Two novel case studies of the crucial role of heterogeneous catalyst supports: core@shell nanostructure and photocatalysis

by

Kevin A. Dahlberg

A dissertation submitted in partial fulfillment
of the requirements for the degree of
Doctor of Philosophy
(Chemical Engineering)
in the University of Michigan
2014

Doctoral Committee:

Professor Johannes W. Schwank, Chair
Adjunct Professor Galen B. Fisher
Professor Nicholas Kotov
Professor Richard M. Laine
Assistant Professor Dominika K. Zgid

Acknowledgements

Many individuals and organizations deserve acknowledgement for their irreplaceable contributions to this thesis. Financial support was provided by the U.S. Army Tank-Automotive Research, Development & Engineering Center (TARDEC) and the University of Michigan MCubed. Kai Sun and Haiping Sun provided transmission electron microscopy (TEM) training and expertise at the Electron Microbeam Analysis Laboratory (EMAL). United Silica and the University of Michigan Auto Lab custom fabricated components for my photocatalytic reactor.

I thank Keegan Cisowski and Jingyi Li, who during their undergraduate research projects aided in the preparation of catalyst materials and shared in my excitement for my project. I owe many thanks to my fellow Schwank Group members from over the years, especially Steve Edmund, Sameer Parvathikar, Joe Mayne, Tom Westrich, Andy Tadd, and Xiaoyin Chen, for their mentorship, encouragement, collaboration, invaluable ideas at crossroads, help in the lab, and senses of humor. Above all I thank my Ph.D. advisor, Johannes Schwank, for his constant support and encouragement of new (and even risky) ideas.

I owe the most thanks to my family: my father, Todd Dahlberg, my mother, Sandy Woodford, and my soon-to-be wife, Carmen Allen. Without their unconditional love and investments in my life, I would be capable of far less.

And last and certainly most importantly, I thank my Creator, who created all the fascinating chemistry I have been privileged to study, and gave me the curious and meticulous mind to appreciate it.

Table of Contents

List of Tables

List of Figures

Abstract

Two catalysis technologies that are promising in the pursuit of more sustainable energy use, particularly reduced use of carbon-based fuels, are fuel reforming and photocatalysis. Unfortunately these technologies each have well-known limitations in their performance, but novel engineering strategies of their catalyst supports could offer effective solutions. Autothermal reforming of hydrocarbons can produce H_2 for fuel cells, yielding greater overall process efficiency than the use of those hydrocarbons in a combustion engine. However, reforming catalysts suffer from metal particle growth, carbon deposition, and sulfur poisoning. The benefits of core@shell nanostructured catalysts over conventional, impregnated catalysts are widely recognized and include increased activity and stability. Less recognized is the potential of the diffusion barrier for reactants and products imposed by the shell material to engender size selectivity characteristics, which may enhance the selectivity of equilibrium-limited reforming reactions. Yolk-shell nanostructured catalysts with encapsulated “egg white” cavities may retain the advantages of core@shell catalysts, and also have more available metal surface area and enhanced size selectivity characteristics due to the accumulation of reaction intermediates in cavities that contain the catalytically active surface.

Both Ni@SiO_2 nanospheres and SiO_2 nanotubes containing Ni nanoparticles were synthesized in a template nonionic surfactant water-in-oil microemulsion, and were characterized by bright field TEM. The highly defined cylindrical cavities in Ni@SiO_2 nanotubes had a uniform diameter of 12-13 nm; however cavity lengths were shown to be strongly dependent on aging time before silica precursor addition, hydrazine concentration, and synthesis temperature.

Depending on synthesis conditions, Ni@SiO_2 nanotubes attained lengths up to 2 microns. A hypothesis is advanced that gas phases form and remain entrained in reverse-micelles, effecting both their elongation and also the exclusion of aggregating silica species to outer micellar regions, thereby causing cavity formation. SiO_2 shell thicknesses could be controlled in the range of 5.1 to 12.4 nm by simple variation of the amount of silica precursor used. Furthermore, H_2 chemisorption measurements demonstrated 14-15% Ni dispersions, and N_2 physisorption analyses showed intraparticle pores on the order of 1 nm, confirming the accessibility of active metal sites via diffusion through the porous silica shells.

Ni@SiO_2 nanotubes, Ni@SiO_2 nanospheres, and impregnated Ni/SiO_2 were comparatively evaluated for propane autothermal reforming performance at 700°C. Results showed that Ni@SiO_2 nanotubes and Ni@SiO_2 nanospheres both had stable activity and H_2 selectivity during 20 hours on stream, whereas impregnated Ni/SiO_2 deactivated continuously over the same time. TGA and TEM analyses of samples following reaction experiments showed that Ni@SiO_2 materials resisted particle growth and carbon deposition, but also experienced SiO_2 shell sintering with unknown consequences for long-term performance. Interestingly, size selectivity characteristics were indicated in the higher H_2, higher CO_2, and lower CO selectivities observed with Ni@SiO_2 catalysts compared to impregnated Ni/SiO_2. These results suggested that H_2, formed in the SiO_2-encapsulated space in contact with Ni nanoparticles, was selectively removed from this space due to its relatively fast diffusion through the SiO_2 shell. These results demonstrate that core@shell nanostructured catalysts hold major promise for reforming applications, and the performance of Ni@SiO_2 may be further improved by utilizing other shell materials less prone to sintering under reforming conditions, such as Al_2O_3 or ZrO_2.

The primary limitation in photocatalysis is low photo efficiency caused by high rates of photo-generated charge carrier recombination, and improvements are needed for photocatalysis to become a practical and economically viable technology. In principle, photocatalysis can offset some of the demand on fossil fuels compared to conventional catalysis by using solar energy to provide the activation energy for catalysts rather than heat. Our group has previously shown for

the first time that photoactivity occurs and even increases at elevated temperatures. There are two beneficial photocatalysis phenomena that potentially occur at elevated temperature with the deposition of Au nanoparticles on the surface of TiO_2. Both phenomena involve the migration of photo-generated electrons to deposited Au nanoparticles according to a well-known mechanism. First, this decreases the rate of electron-hole recombination in TiO_2, which could increase its photocatalytic activity at elevated temperature. Second, this could cause an electrochemical promotion of the Au catalytic activity.

The photoactivities of TiO_2 and Au/TiO_2 catalysts prepared by flame-spray pyrolysis and photodeposition were evaluated by C_2H_4 oxidation experiments in a novel quartz plate reactor and in in-situ DRIFTS experiments. STEM images showed that Au particles had an average size of 11.6 nm. Results showed no photochemical promotion of Au, likely due to a combination of loss of surface hydroxyl species and Au particle growth at elevated temperature. However, a new photocatalytic reaction pathway was discovered on TiO_2 alone which had a maximum rate near 400°C, and which was enhanced by Au nanoparticles in the presence of H_2O. This new pathway may represent an exciting new type of photocatalysis, accessible at high temperature, and inspires future research to understand what other reactions may be catalyzed by its chemistry. Moreover, photocatalytic promotion of catalysis may be achieved by stabilizing a high metal dispersion in close contact with the semiconductor, and a $Au@TiO_2$ nanostructured photocatalyst is in view.

Chapter 1

Introduction

It was reported that the global catalyst market totaled approximately $15.1 billion US dollars in 2012, and is projected to reach $20.1 billion in 2015 [1]. In addition to aiding in the manufacture of an estimated two-thirds of products in the chemical industry [2], catalysts are utilized in transportation fuel refining and in environmental applications. Catalysts are a vital technology for the world's economy and the environment, and there is an ongoing need for innovations and developments in catalysis to meet major current and future challenges in sustainable industrial practice, energy efficiency and production, and environmental protection.

The foremost environmental application for catalysis is emissions control for engines powered by carbon-based fuels. The catalytic converter for gasoline engine vehicles, first commercialized in 1975, is the first and most famous example [3,4]. Since then, and motivated by increasingly strict emissions regulations, engine exhaust after-treatment catalysts have been researched and developed for a wide range of gasoline and diesel engine applications. These catalysts have been highly successful in reducing the emissions of environmentally harmful compounds including hydrocarbons, CO, NO_x, and particulate matter, and increasingly attention is turning to CO_2 emissions. The long-term goal is to find technologies capable of producing energy for all stationary and transportation applications from carbon-neutral processes, like photocatalytic H_2O splitting, photovoltaics, and biomass conversion. However, these technologies currently

remain too expensive and inefficient to replace carbon-based fuels, and finding ways to more efficiently utilize those fuels, such as fuel reforming for fuel cells rather than use in combustion engines, is seen as a promising intermediate solution. It happens that many of these potential fuel efficiency improvements, including fuel reforming, will be dependent on catalysts [3]. Two such applications that will be discussed in detail in this thesis are autothermal reforming and photocatalysis.

The principle motivations within catalysis research are to increase catalyst activity per unit mass or unit cost of catalytically active material, to increase selectivity towards desired reactions, and to increase durability over time. These three specifications are respectively designated as catalytic activity, selectivity, and stability, and together they describe catalyst performance. The cost to industry of replacing catalysts and associated process shut downs was estimated to be on the order of billions of dollars per year in 2001 [5], a significant fraction of the total market, and so the creation of optimized, stable catalysts is a high priority.

Metal nanoparticles are used as the catalytically active material in the majority of applications, for a number of reasons which may be categorized as either geometric or electronic considerations. Of course, minimizing the metal particle size maximizes the dispersion of metal atoms, or the fraction of metal atoms that are on particle surfaces and therefore available for interactions with the reaction phase. The geometric properties of metal nanoparticles arise from their crystal structure and specifically the surface crystal facets that are present on nanoparticle surfaces under reaction conditions. Larger particles tend to have higher-coordinated surface atoms (i.e., terraces) which are relatively less reactive than lower-coordinated atoms (i.e., steps, kinks, or defects) prevalent on smaller particles. A reaction is called structure sensitive when its activation energy is different on terrace and step sites, and consequently its turnover frequency is observed to be dependent on metal particle size [6,7,8]. In some cases, terrace sites and step sites preferentially catalyze different reactions or reaction steps for the same reactants or intermediates [9], and so the reaction selectivity can be dependent on particle size [10].

Lower-coordinated metal surfaces are also known to be the growth sites of deleterious graphitic carbon structures in fuel reforming applications [11]. A recent strategy demonstrated for mitigating carbon deposition on a high-loading Ni-based reforming catalyst was to deposit Sn on the surface of Ni particles. Sn atoms decorating the surface of large Ni particles broke up ensembles of higher-coordinated Ni atoms and resulted in almost complete abatement of carbon deposition during steam reforming of methane, propane, and isooctane [12].

Metal nanoparticles may also exhibit beneficial electronic characteristics for heterogeneous and photocatalytic applications which do not occur in their bulk metal forms. Famously, Haruta observed that Au nanparticles have a high catalytic activity for CO oxidation when they are smaller than 20 nm [13]. More recent work has shown that perimeter Au sites are the active sites for the rate-limiting step, where adsorbed CO from Au edge sites and adsorbed O from the reducible oxide support react. Accordingly, it is not surprising that hemispherical Au nanoparticles have been found to be more active than spherical nanoparticles because they have more perimeter sites. [14]. This may simply indicate that oxidation reactions on Au catalysts are strongly structure sensitive. But there are also arguments that these perimeter Au atoms interact electronically with the support, and may exist in a highly active cationic state stabilized by hydroxyl groups [14].

Nanoparticles of certain metals can exhibit electronic effects which can enhance the performance of semiconductors in photocatalysis and photovolatics applications [15,16,17]. Plasmons are energetic oscillations of electrons on the surface of metal nanoparticles such as Ag or Au that occur with absorption of photons at a characteristic resonant wavelength, and can enhance the photo efficiency of semiconductors in several ways. First, plasmons can intensify the electromagnetic field strength in the vicinity of plasmonic nanoparticles to generate more charge carriers in the semiconductor. Second, they can act as scattering centers for photons, creating a longer photon path through semiconductors, resulting in more charge carrier generation. It has also been claimed that plasmons can inject electrons into the

conduction band of semiconductors [18], but most evidence supports a phenomenon called Fermi level equilibration, where photo-generated electrons in the semiconductor are transferred to metal nanoparticles in electrical contact [19]. This transfer of electrons hinders charge carrier recombination, thus enhancing photo efficiency. Choi *et al*. cleverly demonstrated both the plasmonic and Fermi level equilibration effects individually for their improvements of solar cells by investigating SiO_2- and TiO_2-encapsulated Au nanoparticles [17]. Cells with deposited Au@SiO_2 revealed the improvement from plasmons only, whereas cells with deposited Au@TiO_2 revealed both plasmon and Fermi level equilibration effects.

In most photocatalytic reactions, photo-generated charge carriers react with chemical adsorbates on the semiconductor surface, and so the above effects which hinder charge carrier recombination and increase photo efficiency can also increase photocatalytic activity. In photocatalysis applications, plasmons can also contribute directly to catalytic activity by injecting electrons into adsorbed reactants, lowering the energy barrier for their reaction [15,16].

In catalysis applications, metal nanoparticles are conventionally dispersed over a porous, thermally stable but catalytically inactive support to maintain a high metal dispersion during operation. Indeed, because long-term catalyst stability in almost every application is limited by deactivation related to metal nanoparticle growth leading to irreversible loss of active surface area, supports that maximize and stabilize metal nanoparticle dispersion over time are highly desirable. But research continues to show how the support can be highly determining of catalyst activity, selectivity, and stability in a plethora of other ways. Supports can actively participate in reaction pathways, by providing oxygen storage capacity or specific active sites for activation of one or more reactants, such as dissociative adsorption of H_2O or CO_2 with subsequent transfer of oxygen species to the metal surface [20,21,22]. Supports can alter the electronic properties of the metal or vice versa; for example, the activity and selectivity of Pt/CeO_2 catalysts for the water-gas shift reaction were observed to be highly dependent on the degree of interaction of the Pt and CeO_2 [23,24].

Supports can also affect selectivity by imposing diffusion barriers for reactants and products, if catalytic metal nanoparticles or active sites are only accessible through pores with sizes on the order of molecular length, 0.3 to 2 nm [25]. Size selectivity characteristics in catalysis are best known as shape selectivity in catalytic reactions on zeolites. This selectivity can take many forms, including reactant, product, and transition state selectivities, among other less widely accepted forms [26]. In general, shape selectivity is related to either intraparticle diffusion or limitations to transition states, both of which can be either competitive or exclusive [26]. A famous example is the shape selective alkylation of 4,4'-biphenol with propylene to 4,4'-diisopropylbiphenyl on H-mordenite [27].

Catalysts with a core@shell nanostructure (in which metal nanoparticles are encapsulated in a porous shell, as depicted in Figure 1.1(a) and (d), have attracted interest for a wide variety of reaction systems due to their ability to achieve, to control, and to maximize the above support effects. Because the metal nanoparticles in core@shell catalysts are isolated from each other, they are highly resistant to particle growth [28,29,30,31]. In addition, the porous shell imposes a diffusion barrier that physically separates the metal nanoparticles from the bulk gas phase, which can provide stability against leaching and Ostwald ripening [32,33,34], and can produce size selectivity characteristics, such as the selective oxidation of methane on Pt@SiO_2 in the presence of larger, more reactive hydrocarbons [35]. The core@shell nanostructure also has the characteristic of maximizing the contact between the metal and support materials, and can be optimal in cases where metal-support interactions are beneficial [23,24,36,37]. The size selectivity characteristics of core@shell catalysts are different from those of impregnated zeolites or egg yolk-structured [38] catalysts due to the complete encapsulation of metal nanoparticles, the small size of the shells (on the order of 50 nm) compared to typical zeolite particles (on the order of 500 nm), and the often catalytically inactive shell material (e.g., SiO_2). When the shell material is inactive, the catalytic activity of core@shell nanostructured materials is completely dependent on diffusion of reaction species through the shell, whereas in much

other shape selectivity work, for example with zeolites, a sometimes significant contribution of surface activity occurs.

In the last decade, core@shell catalysts have been investigated several times for their particular advantages for fuel reforming applications, wherein catalyst deactivation due to particle growth greatly hinders performance [39,40,41,42,43,44,45]. Catalytic fuel reforming generates syngas (i.e., H_2 and CO) from a readily available hydrocarbon fuel. The syngas can then be converted into electrical energy by a solid oxide fuel cell (SOFC). One specific application for fuel cells is the auxiliary power unit (APU), which utilizes liquid transportation fuels such as gasoline, diesel, or JP-8 jet fuel onboard a vehicle to efficiently produce electrical power that would otherwise be produced by significant durations of engine idling accompanied by unnecessary exhaust emissions [46]. The efficiency of this fuel-to-electricity conversion in an APU is high, up to 50-60%, whereas that of the alternative conversion by the engine is limited by Carnot thermodynamic losses to 34% at most [47]. Ni-based catalysts are attractive for fuel reforming applications because of their low cost, but are especially prone to particle growth and carbon deposition. Carbon deposition might even be indirectly caused by particle growth, according to evidence that carbon deposition does not occur when Ni particles are below a certain size [11]. Therefore the core@shell nanostructure, well known to mitigate particle growth, may be ideal for fuel reforming.

Several studies have reported the superior activity and stability of Ni@SiO_2 for methane partial oxidation and propane steam reforming over conventional, impregnated Ni/SiO_2 catalysts [41,43,45]. Whereas Ni@SiO_2 has been seen to maintain a steady performance with high hydrocarbon conversion and syngas selectivity for up to 5-10 hr on stream, impregnated Ni-based catalysts were observed to deactivate continuously under the same conditions. Researchers have claimed that particle growth and carbon deposition are less extensive for core@shell catalysts, but these have not been quantified consistently. More concerning is the fact that although TEM images have been shown for the fresh catalyst samples, none have been shown for samples following reaction experiments. Therefore it is not known if and what types

of deactivation could occur for Ni@SiO_2 catalysts under fuel reforming conditions during longer times on stream, especially morphological changes that would degrade the SiO_2 shell porosity and render the catalytically active material inaccessible.

Under normal operation, the selectivity of fuel reforming reactions is determined (and limited) by equilibrium, and so the size selectivity characteristics of Ni@SiO_2 are expected to have a significant effect on the observed selectivity. Specifically, H_2 has a small molecular size and may be quickly removed from the gas phase in contact with the catalytic active surface once formed, causing the steam reforming and water-gas shift reactions to continue to form more products to establish equilibrium. Essentially, Ni@SiO_2 particles may act as membrane nanoreactors, however researchers have not addressed this possibility.

Yolk-shell nanostructured catalysts, in which the “egg white” is a cavity (Figure 1.1(b) and (e)), may retain the advantageous characteristics of the core@shell nanostructure while potentially producing additional desirable effects, such as decreased extent of blocking of the metal surface by the support and further enhanced selectivity due to the accumulation of reaction intermediates in the gas phase in contact with the catalytic active surface. However no studies that directly compare the performances of yolk-shell and core@shell catalyst morphologies have been reported. Several synthetic strategies for yolk-shell have been reported, though most do not allow complete encapsulation of the metal nanoparticles and are limited to certain materials [36,48,49,50,51,52,53,54]. Microemulsion template syntheses are simple and lead to uniform, tunable core@shell nanoparticles, but a procedure for yolk-shell materials has not been reported.

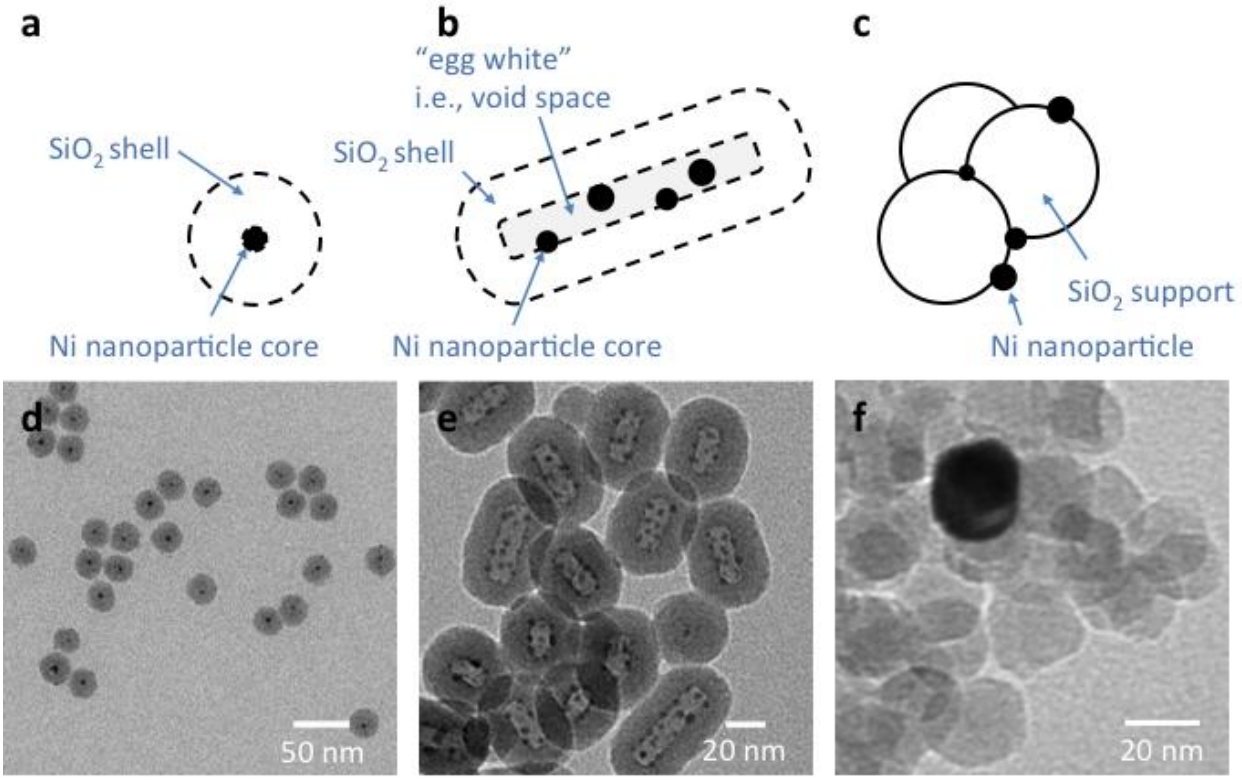

Figure 1.1 Diagrams and TEM images representing core@shell, yolk-shell, and impregnated morphologies of a Ni-based catalyst with SiO_2 support. (a,d) Ni@SiO_2 core@shell nanospheres, (b,e) Ni@SiO_2 yolk-shell nanotubes, and (c,f) impregnated Ni/SiO_2.

The work presented in Chapters 2 and 3 was performed to address the above stated open questions in the literature regarding long-term stability of Ni@SiO_2 catalysts for fuel reforming, the potential synthesis of yolk-shell Ni@SiO_2 using a microemulsion template, and the potential additional advantages offered by the yolk-shell nanostructure over the core@shell nanostructure. Chapter 2, published in *Chemistry of Materials*, presents a novel, tunable microemulsion template synthesis technique for Ni@SiO_2 nanotubes and nanospheres, and the characterization of the catalytic properties of these materials [55]. By identifying and controlling important synthesis variables, and with careful TEM imaging and measurement, a thorough profile of the formation of Ni@SiO_2 nanospheres and nanotubes could be developed, and a greater understanding of the underlying microemulsion phenomena could be gained.

Chapter 3 reports the comparative evaluation of the Ni@SiO_2 nanospheres and nanotubes developed in Chapter 2 and a conventional, impregnated Ni/SiO_2 material for propane autothermal reforming. Because hydrocarbons are rapidly and completely converted to light

olefins, methane, and reforming products (i.e., CO, CO_2, and H_2) at the reforming catalyst entrance [56,57,58,59,60,61,62], propane is an appropriate study hydrocarbon which may represent the performance of liquid hydrocarbons. By analyzing catalyst samples with TGA and TEM following reaction experiments, carbon deposition, metal particle growth, and morphological changes could be observed and quantified. Finally, by carefully monitoring the concentrations of all reactants and products over time, selectivity differences between the catalyst morphologies could be analyzed.

Fuel reforming on Ni-based catalysts also suffers from sulfur poisoning. Our group has extensively investigated the mechanism of sulfur poisoning and potential solutions, and this work was published in *Journal of Catalysis* [63] and *Applied Catalysis A: General* [64]. We found that operating the fuel reforming reaction in reactant composition regimes in which the equilibrium yield of H_2 is high leads to high desulfurization activity and nearly complete abatement of sulfur effects [63]. We also learned through fuel reforming experiments and measurement of Ni particle sizes in catalysts with TEM and XRD techniques that sulfur affects larger Ni particles more than smaller particles [64]. Given this knowledge, it is possible that the nanostructure of Ni@SiO_2 could render it resistant to sulfur poisoning in two ways. First, because larger Ni particles were found to be more susceptible to sulfur poisoning, and because Ni@SiO_2 is resistant to particle growth, this catalyst could maintain a high dispersion of Ni under reforming conditions and thus curtail sulfur poisoning. Second, the size selectivity of the SiO_2 shell may protect Ni particles from exposure to large, sulfur-containing species like dibenzothiophene, which are not converted to smaller molecules by homogeneous reactions like hydrocarbons. These hypotheses for Ni@SiO_2 are promising but are left to future work.

Chapter 4 begins a different study of support effects, exploring novel approaches by which electronic metal-support interactions can enhance catalytic properties and performance in photocatalysis. Lowering the operating temperature of catalysts to decrease the required amount of thermal energy input is a strong motivation in catalysis research. Photocatalysis is one such strategy, in which a semiconductor uses photon energy to offset reaction energy

barriers typically overcome by thermal energy. Unfortunately, photocatalysis is practically limited by poor energy conversion efficiency, and although substantial work has pursued improvements through doping, coupling two or more semiconductors, exploring a wide range of semiconductor materials, controlling phase composition, and controlling particle size, to date these improvements have not made photocatalysts sufficiently efficient for full-scale operations [65]. Excessively large irradiation areas would still be needed to absorb enough solar energy to achieve a reasonable amount of chemical conversion for various applications, for example photocatalytic H_2O splitting to H_2. Significant improvements are still needed, and although further optimization through the currently known strategies listed above is possible, new strategies for engineering photocatalysts are certainly welcome.

In work we published in the *Journal of Physical Chemistry C*, our group showed for the first time how photocatalytic efficiency may be enhanced as temperature increases in non-aqueous conditions [66]. We found maximum photocatalytic ethylene oxidation rates on TiO_2 near 150°C, with photocatalytic rates then decreasing at higher temperatures due to increasing phonon recombination rates. We also proposed a quantitative model predicting the significant effects of TiO_2 phase composition on photocatalytic efficiency. This work left several open questions that warrant further study. Surface hydroxyl radicals produced from photo-generated holes are known to be the primary oxidizing species in photocatalytic oxidation reactions [67], and so H_2O concentration in the reactant stream is expected to have a significant effect on photocatalytic behavior. But the effect of H_2O concentration was not studied at elevated temperature. Furthermore, only the formation of CO_2 was measured, and the formation of partial oxidation products such as H_2CO and CO was completely neglected.

Under ambient conditions, when metal nanoparticles are deposited on photocatalytic semiconductors, photo-generated electrons are known to transfer to metal nanoparticles that have a lower Fermi level than the semiconductor [17,68,69,70]. This effect is known as Fermi level equilibration, because if photo-generated electrons accumulate in metal nanoparticles, the transfer process continues until the Fermi level of the metal is raised to that of the

semiconductor. Studies have shown that this phenomenon decreases charge carrier recombination rates, and therefore increases the photo efficiency of the semiconductor [71,72,73,74,75]. However it is not known if this effect occurs at elevated temperature, which could even further enhance the photocatalytic rates achieved by our group. A second fascinating implication of the potential transfer of photo-generated electrons to metal nanoparticles at elevated temperatures is analogous to charge-donating promotion mechanisms well known for heterogeneous catalysis, including doping with an alkali metal and electrochemical promotion of catalysis (EPOC) [76]. If such a promotion could be accomplished through photocatalysis, this could open a new field of catalysis research in which the material properties of the support semiconductor could be decoupled from those of the catalytic metal nanoparticles, and the limitations of doping with electron donors and EPOC could be circumvented.

To investigate both potential effects of the transfer of photo-generated electrons to deposited metal nanoparticles at elevated temperatures, and to further illuminate photocatalytic behavior at elevated temperatures, TiO_2 and Au/TiO_2 were evaluated in photocatalytic ethylene oxidation experiments between 50°C and 500°C, with and without H_2O in the reactant stream. To perform the photocatalysis experiments at elevated temperatures, a novel, automated reactor system was designed and constructed. Steady-state, in-situ DRIFTS experiments were also performed to investigate the catalytic contributions of Au and TiO_2, the nature of surface hydroxyl species and surface intermediates, and the contributions of thermal and photocatalytic reactions. The results of this work are presented in Chapter 4.

This dissertation explores the above subjects in catalyst support engineering: core@shell nanostructure applied to autothermal reforming of propane and photocatalysts with deposited metal nanoparticles applied to ethylene oxidation. Both these specific catalytic reaction systems may be improved by the insights gained in this work, but moreover this thesis seeks to expand the knowledge of metal-support interactions along two new dimensions and reveal new methods in how they can be exploited to engineer catalysts for a wide variety of reactions.

Chapter 5 will summarize the latest additions to this knowledge, clarify new questions, and offer recommendations on how these questions may be addressed in future work.

References

[1] Bozich, F. BASF Global Catalysis Research. September 6, 2012. *BASF's Catalysts Division: Driving Accelerated Growth.* Presented at BASF Investor Day Automotive, Ludwigshafen, Germany.

[2] Nees, F. BASF Global Catalysis Research. September 25, 2008. *Heterogeneous Catalysis at BASF*. Presented at Journalists and Scientists in Dialogue: Catalysis – Driver for Innovation, Ludwigshafen, Germany.

[3] Shelef, M.; McCabe R.W. Twenty-five years after introduction of automotive catalysts: what next? *Catal. Today* **2000**, *62*, 35-50.

[4] Gandhi, H.S.; Graham, G.W.; McCabe, R.W. Automotive exhaust catalysis. *J. Catal.* **2003**, *216*, 433-442.

[5] Bartholomew, C.H. Mechanisms of catalyst deactivation. *Appl. Catal., A* **2001**, *212*, 17-60.

[6] Atalik, B.; Uner, D. Structure sensitivity of selective CO oxidation over Pt/γ-Al_2O_3. *J. Catal.* **2006** *241*, 268-275.

[7] Bond, G.C. The Origins of particle size effects in heterogeneous catalysis. *Surf. Sci.* **1985**, *156*, 966-981.

[8] Van Meerten, R.Z.C.; Beaumont, A.H.G.M.; Van Nisselrooij, P.F.M.T.; Coenen, J.W.E. Structure sensitivity and crystallite size change of nickel during methanation of CO/H2 on nickel-silica catalysts. *Surf. Sci.* **1983**, *135*, 565-579.

[9] Goodman, D.W. Impurity modification of surface catalyzed reactions: Cyclopropane over sulfide nickel. *J. Vac. Sci. Technol. A* **1984**, *2*, 873-876.

[10] Goodman, D.W. Correlations between Surface Structure and Catalytic Reactivity for Alkane Hydrogenolysis over Nickel. Proc. of the 8th International Conference on Catalysis, p. 3-12, 1984.

[11] Gould, B. D.; Chen, X.; Schwank, J. W. Dodecane reforming over nickel-based monolith catalysts: Deactivation and carbon deposition. *Appl. Catal., A* **2008**, *334*, 277-290.

[12] Nikolla, E.; Schwank, J.W.; Linic S. Promotion of the long-term stability of reforming Ni catalysts by surface alloying. *J. Catal.* **2007**, *250*, 85-93.

[13] Haruta, M.; Yamada, N.; Kobayashi, T.; Iijima, S. Gold catalysts prepared by coprecipitation for low-temperature oxidation of hydrogen and of carbon monoxide. *J. Catal.* **1989**, *115*, 301-309.

[14] Yu, Y.; Huang, J.; Ishida, T.; Haruta, M. Unique catalytic performance of supported gold nanoparticles in oxidation. In Modern Heterogeneous Oxidation Catalysis, p. 77-124, 2009.

[15] Chistopher, P.; Xin, H.; Marimuthu, A.; Linic, S. Singular characteristics and unique chemical bond activation mechanisms of photocatalytic reactions on plasmonic nanostructures. *Nat. Mater.* **2012**, *11*, 1044-1050.

[16] Linic, S.; Christopher, P.; Ingram, D.B. Plasmonic-metal nanostructures for efficient conversion of solar to chemical energy. *Nat. Mater.* **2011**, *10*, 911-921.

[17] Choi, H.; Chen, W. T.; Kamat, P. V. Know thy nano neighbor. Plasmonic versus electron charging effects of metal nanoparticles in dye-sensitized solar cells. *Nano* **2012**, *6*, 4418-4427.

[18] Primo, A.; Corma, A.; Garcia, H. Titania supported gold nanoparticles as photocatalyst. *Phys. Chem. Chem. Phys.* **2011**, *13*, 886-910.

[19] Kamat, P.V. Photophysical, Photochemical and Photocatalytic Aspects of Metal Nanoparticles. *J. Phys. Chem.* B **2002**, *106*, 7729-7744.

[20] Maillet, T.; Madier, Y.; Taha, R.; Barbier, J.; Duprez, D. Spillover of oxygen species in the steam reforming of propane on ceria-containing catalysts. *Stud. Surf. Sci. Catal.* **1997**, *112*, 267-275.

[21] Olafsen, A.; Slagtern, A.; Dahl, I.M.; Olsbye, U.; Schuurman, Y.; Mirodatos, C. Mechanistic features for propane reforming by carbon dioxide over a Ni/Mg(Al)O hydrotalcite-derived catalyst. *J. Catal.* **2005**, *229*, 163-175.

[22] Pengpanich, S.; Meeyoo, V.; Rirksomboon, T.; Schwank, J. Hydrogen production from partial oxidation of iso-octane over Ni/$Ce_{0.75}Zr_{0.25}O_2$ and Ni/β"-Al_2O_3 catalysts. *Appl. Catal., A* **2006**, *302*, 133-139.

[23] Yeung, C.; Meunier, F.; Burch, R.; Thompsett, D.; Tsang, S. Comparison of New Microemulsion Prepared "Pt-in-Ceria" Catalyst with Conventional "Pt-on-Ceria" Catalyst for Water-Gas Shift Reaction. *J. Phys. Chem. Lett.* **2006**, *110*, 8540-8543.

[24] Yeung, C., Tsang, S. Some optimization in preparing core-shell Pt–ceria catalysts for water gas shift reaction. *J. Mol. Catal. A: Chem.* **2010**, *322*, 17-25.

[25] van Bekkum, G. Flanigen, E., Jacobs, P., Jansen, J., editors. Introduction to zeolite science and practice. 2001. Amsterdam.

[26] Degnan, T.F.; The implications of the fundamentals of shape selectivity for the development of catalysts for the petroleum and petrochemical industries. *J. Catal.* **2003**, *216*, 32-46.

[27] Lee, G.-S. The Zeolite Mordenite Story. Proc. of the 32nd Michigan Catalysis Society Spring Symposium, 2010.

[28] Hanaoka, T.; Hayashi, H.; Tago, T.; Kishida, M.; Wakabayashi, K. In situ immobilization of ultrafine particles synthesized in a water/oil microemulsion. *J. Colloid Interface Sci.* **2001**, *235*, 235–240.

[29] Kong, T.; Yu, K.; Tsang, S. Silica coated noble metal nanoparticle hydrosols as supported catalyst precursors. *J. Nanosci. Nanotechnol.* **2006**, *6*, 1167-1172.

[30] Kim, M.; Sohn, K.; Na, H.; Hyeon, T. Synthesis of nanorattles composed of gold nanoparticles encapsulated in mesoporous carbon and polymer shells. *Nano Lett.* **2002**, *2*, 1383-1387.

[31] Joo, S. H.; Park, J. Y.; Tsung, C. K.; Yamada, Y.; Yang, P.; Somorjai, G. A. Thermally stable Pt/mesoporous silica core-shell nanocatalysts for high-temperature reactions. *Nat. Mater.* **2009**, *8*, 126-131.

[32] Takenaka, S.; Hirata, A.; Tanabe, E.; Matsune, H.; Kishida, M. Preparation of supported Pt-Co alloy nanoparticle catalysts for oxygen reduction reaction by coverage with silica. *J. Catal.* **2010**, *274*, 228-238.

[33] Takenaka, S.; Matsumori, H.; Matsune, E.; Tanabe, M.; Kishida, J. High durability of carbon nanotube-supported Pt electrocatalysts covered with silica layers for the cathode in a PEMFC *J. Electrochem. Soc. **2008**, 155*, B929-B936.

[34] Zhou, C.; Peng, F.; Wang, H.; Yu, H.; Peng, C.; Yang, J. Development of stable PtRu catalyst coated with manganese dioxide for electrocatalytic oxidation of methanol. *Electrochem. Commun.* **2010**, *12*, 1210-1213.

[35] Hori, K.; Matsune, H.; Takenaka, S.; Kishida, M. Preparation of silica-coated Pt metal nanoparticles using microemulsion and their catalytic performance. *Sci. Technol. Adv. Mater.* **2006**, *7*, 678-684.

[36] Chen, W.; Pan, X.; Bao, X. Tuning of redox properties of iron and iron oxides via encapsulation within carbon nanotubes. *J. Am. Chem. Soc.* **2007**, *129*, 7421-7426.

[37] Yu, K.; Wu, Z.; Zhao, Q.; Li, B.; Xie, Y. High-temperature-stable Au@SnO_2 core/shell supported catalyst for CO oxidation. *J. Phys. Chem. C* **2008**, *112*, 2244-2247.

[38] Lekhal, A.; Glasser, B.; Khinast, J. Drying of supported catalysts. In Catalyst Preparation: Science and Engineering I. Regalbuto, J., ed. 2006. 375-403.

[39] Montini, T.; Condo, A. M.; Hickey, N.; Lovey, F. C.; De Rogatis, L.; Fornasiero, P.; Graziani, M. Embedded Rh(1 wt.%)@Al_2O_3: Effects of high temperature and prolonged aging under methane partial oxidation conditions. *Appl. Catal., B* **2007**, *73*, 84-97.

[40] Xu, S.; Zhao, R.; Wang, X. Highly coking resistant and stable Ni/Al_2O_3 catalysts prepared by W/O microemulsion for partial oxidation of methane. *Fuel Process. Technol.* **2004**, *86*, 123-133.

[41] Takenaka, S.; Umebayashi, H.; Tanabe, E.; Matsune, H.; Kishida, M. Specific performance of silica-coated Ni catalysts for the partial oxidation of methane to synthesis gas. *J. Catal.* **2007**, *245*, 392-400.

[42] Xu, J.; Yeung, C. M. Y.; Ni, J.; Meunier, F.; Acerbi, N.; Fowles, M.; Tsang, S. C. Methane steam reforming for hydrogen production using low water-ratios without carbon formation over ceria coated Ni catalysts. *Appl. Catal., A* **2008**, *345*, 119-127.

[43] Takenaka, S.; Orita, Y.; Umebayashi, H.; Matsune, H.; Kishida, M. High resistance to carbon deposition of silica-coated Ni catalysts in propane steam reforming. *Appl. Catal., A* **2008**, *351*, 189-194.

[44] Montini, T.; De Rogatis, L.; Gombac, V.; Fornasiero, P.; Graziani, M. Rh(1%)@$Ce_xZr_{1-x}O_2$–Al_2O_3 nanocomposites: Active and stable catalysts for ethanol steam reforming. *Appl. Catal., B* **2007**, *71*, 125-134.

[45] Li, L.; He, S.; Song, Y.; Zhao, J.; Ji, W.; Au, C.-T. Fine-tunable Ni@porous silica core–shell nanocatalysts: Synthesis, characterization, and catalytic properties in partial oxidation of methane to syngas. *J. Catal.* **2012**, *288*, 54-64.

[46] Jain, S.; Chen, H.; Schwank, J. Techno-economic analysis of fuel cell auxiliary power units as alternative to idling. *J. Power Sources* **2006**, *160*, 474-484.

[47] Song, C. Fuel processing for low-temperature and high-temperature fuel cells: Challenges, and opportunities for sustainable development in the 21st century. *Catal. Today* **2002**, *77*, 17-49.

[48] Lee, J.; Park, J. C.; Song, H. A nanoreactor framework of a Au@SiO_2 yolk/shell structure for catalytic reduction of p-nitrophenol. *Adv. Mater.* **2008**, *20*, 1523-1528.

[49] Arnal, P. M.; Comotti, M.; Schüth, F. High-temperature-stable catalysts by hollow sphere encapsulation. *Angew. Chem. Int. Ed.* **2006**, *45*, 8224-8227.

[50] Somorjai, G. A.; Rioux, R. M. High technology catalysts towards 100% selectivity: Fabrication, characterization and reaction studies. *Catal. Today* **2005**, *100*, 201-215.

[51] Ikeda, S.; Ishino, S.; Harada, T.; Okamoto, N.; Sakata, T.; Mori, H.; Kuwabata, S.; Torimoto, T.; Matsumura, M. Ligand-free platinum nanoparticles encapsulated in a hollow porous carbon shell as a highly active heterogeneous hydrogenation catalyst. *Angew. Chem. Int. Ed.* **2006**, *45*, 7063-7066.

[52] Yin, Y.; Rioux, R. M.; Erdonmez, C. K.; Hughes, S.; Somorjai, G. A.; Alivisatos, A. P. Formation of hollow nanocrystals through nanoscale Kirkendall effect. *Science* **2004**, *304*, 711-714.

[53] Huang, X.; Guo, C.; Zuo, J.; Zheng, N.; Stucky, G. D. An assembly route to inorganic catalytic nanoreactors containing sub-10-nm gold nanoparticles with anti-aggregation properties. *Small* **2009**, *5*, 361-365.

[54] Pan, X.; Fan, Z.; Chen, W.; Ding, Y.; Luo, H.; Bao, X. Enhanced ethanol production inside carbon-nanotube reactors containing catalytic particles. *Nat. Mater.* **2007**, *6*, 507-511.

[55] Dahlberg, K.; Schwank, J. Synthesis of Ni@SiO_2 nanotube particles in a water-in-oil microemulsion template. *Chem. Mater.* **2012**, *24*, 2635-2644.

[56] Dreyer, B., Lee, I., Krummenacher, J., Schmidt, L. Autothermal steam reforming of higher hydrocarbons: *n*-Decane, n-hexadecane, and JP-8. *Appl. Catal., A* **2006**, *307*, 184-194.

[57] Yoon, S.; Kang, I.; Bae, J. Suppression of ethylene-induced carbon deposition in diesel autothermal reforming. *Int. J. Hydrogen Energy* **2009**, *3*, 1844-1851.

[58] Yoon, S.; Kang, I.; Bae, J. Effects of ethylene formation in diesel autothermal reforming. *Int. J. Hydrogen Energy* **2008**, *33*, 4780-4788.

[59] Horn, R.; Williams, K.; Degenstein, N.; Bitsch-Larsen, A.; Nogare, D.; Tupy, S.; Schmidt, L. Methane catalytic partial oxidation on autothermal Rh and Pt catalysts: Oxidation and reforming zones, transport effects, and approach to thermodynamic equilibrium. *J. Catal.* **2007**, *249*, 380-393.

[60] Hotz, N.; Osterwalder, N.; Stark, W.; Bieri, N.; Poulikakos, D. Disk-shaped packed bed micro-reactor for butane-to-syngas processing. *Chem. Eng. Sci.* **2008**, *63*, 5193-5201.

[61] Joensen, F.; Rostrup-Nielsen, J.R. Conversion of hydrocarbons and alcohols for fuel cells. *J. Power Sources* **2002**, *105*, 195-201.

[62] Randolph, K.; Dean, A. Hydrocarbon fuel effects in solid-oxide fuel cell operation: An experimental and modeling study of *n*-hexane pyrolysis. *Phys. Chem. Chem. Phys.* **2007**, *9*, 4245-4258.

[63] Mayne, J. M.; Tadd, A. R.; Dahlberg, K. A.; Schwank, J. S. Influence of thiophene on the isooctane reforming activity of Ni-based catalysts. *J. Catal*. **2010**, *271*, 140-152.

[64] Mayne, J. M.; Dahlberg, K. A.; Westrich, T. A.; Tadd, A. R.; Schwank, J. S. Effect of metal particle size on sulfur tolerance of Ni catalysts during autothermal reforming of isooctane. *Appl. Catal., A* **2011**, *400*, 203-214.

[65] Mohamed, H.H.; Bahnemann, D.W. The Role of Electron Transfer in Photocatalysis: Facts and Fictions. *Appl. Catal., B* **2012**, *128*, 91-104.

[66] Westrich, T.A.; Dahlberg, K.A.; Kaviany, M.; Schwank, J.W. High-temperature phtocatalytic ethylene oxidation over TiO_2. *J. Phys. Chem. C* **2011**, *115*, 16537-16543.

[67] Fox, M.A.; Dulay, M.T. Heterogeneous photocatalysis. *Chem. Rev.* **1993**, *93*, 341-357.

[68] Subramanian, V.; Wolf, E.E.; Kamat, P.V. Catalysis with TiO_2/gold nanocomposities. Effect of metal particle size on the Fermi level equilibration. *J. Am. Chem. Soc.* **2004**, *126*, 4943-4950.

[69] Hirakawa, T.; Kamat, P.V. Charge separation and catalytic activity of Ag@TiO_2 core-shell composite clusters under UV-irradiation. *J. Am. Chem. Soc.* **2005**, *127*, 3928-3934.

[70] Jakob, M.; Levanon, H.; Kamat, P.V. Charge distribution between UV-irradiated TiO_2 and gold nanoparticles: Determination of shift in the Fermi level. *Nano Lett.* **2003**, *3*, 353-358.

[71] Jovik, V.; Al-Azri, Z.H.N.; Chen, W.-T.; Sun-Waterhouse, D.; Idriss, H.; Waterhouse, G.I.N. Photocatalytic H_2 production from ethanol-water mixtures over Pt/TiO_2 and Au/TiO_2 photocatalysts: A comparative study. *Top. Catal.* **2013**, *56*, 1139-1151.

[72] Shen, P.; Zhao, S.; Su, D.; Li, Y.; Orlov, A. Outstanding performance of sub-nm Au clusters for photocatalytic hydrogen production. *Appl. Catal., B* **2012**, *126*, 153-160.

[73] Lin, H.-Y.; Chang, Y.-S. Photocatalytic water splitting for hydrogen production on $Au/KTiNbO_5$. *Int. J. Hydrogen Energy* **2010**, *35*, 8463-8471.

[74] Mohamed, H.H.; Dillert, R.; Bahnemann, D.W. Kinetic and Mechanistic Investigations of the Light Induced Formation of Gold Nanoparticles on the Surface of TiO_2. *Chem. Eur. J.* **2012**, *18*, 4314-4321.

[75] Nosaka, Y.; Norimatsu, K.; Miyama, H. The function of metals in metal-compounded semiconductor photocatalysis. *Chem. Phys. Lett.* **1984**, *106*, 128-131.

[76] Ibrahim, N.; Poulidi, D.; Metcalfe, I.S. The role of sodium surface species on electrochemical promotion of catalysis in a Pt/YSZ system: The case of ethylene oxidation. *J. Catal.* **2013**, *303*, 100-109.

Chapter 2

Synthesis of Ni@SiO_2 nanotube particles in a water-in-oil microemulsion template

Introduction

A fundamental motivation in heterogeneous catalysis is to develop catalytic materials that have a stable active metal surface area and high selectivity for desired reactions. Recently, coated catalysts (often designated core@shell), materials with catalytically active metal surfaces covered by porous oxides, have drawn attention for their unique advantages in electrocatalytic [1,2,3,4,5,6,7], water-gas shift [8,9,10,11], steam reforming [12,13,14], partial oxidation [15,16,17], hydrogenation [18,19,20,21,22,23], and photocatalytic water-splitting reactions [24]. These materials are known for the enhanced stability of confined metal nanoparticles and the maximized contact of metal and oxide support [19,20,25].

Compared to conventional supported metal catalysts, coated metal particles exhibit less tendency for metal particle growth and hence irreversible active surface area loss. Metal particles covered with oxide layers are less susceptible to surface migration leading to sintering,

and to single-atom migration such as in Ostwald ripening or leaching [1]. The oxide encapsulation can also prevent the formation of carbon structures on metal surfaces [15,16], which causes reversible deactivation through active site blocking and can also cause irreversible, highly deleterious separation of metal particles and support [26]. This stabilizing encapsulation of metal nanoparticles is particularly advantageous in the case of alloys, whose synthesis often involves a compromise between higher temperatures required for alloy formation and consequent particle growth and metal separation [3,8]. Encapsulation of alloys also adds stability against growth and metal separation during catalytic operation.

Several remarkable methods have emerged by which the reaction selectivity of catalysts can be modified by the coating structure from corresponding conventional supported structures. Porous oxide shells in coated materials typically have pore sizes on the order of 1-2 nm, and can therefore introduce shape selectivity characteristics [20,27,28,29]. The intimate contact of metal and oxide material in coated materials can increase their electronic interaction, which has been shown to change the redox character of metals [15,18]. For certain materials a "synergistic confinement effect" has been hypothesized, wherein a charge transfer occurs between the coating material and metal particles. This has been used to explain observations of enhanced activity and selectivity of CO hydrogenation to ethanol on Rh@carbon nanotubes (CNTs) [30], increased metal reducibility in Fe@CNTs [31], and enhanced CO oxidation activity of Au@SnO_2 [32]. Enhanced electronic interaction has also been shown to promote otherwise inactive oxide surfaces, leading to improvements in activity and selectivity compared to the corresponding metal surfaces in conventional supported catalysts [8,9,10,11,14].

Compared to the more tightly-encapsulated core@shell materials discussed above, a yolk-shell catalyst structure, in which a cavity containing metal nanoparticles is encapsulated with a porous coating material, has additional advantages. With the desirable metal particle confinement and oxide-metal interaction properties retained, a more open cavity environment allows greater accessibility of metal surfaces and potentially avoids transition state shape selectivity effects. These cavity structures could also facilitate the accumulation of reactants,

intermediates, and products in the local environment of metal particles, which may aid selectivity [30]; and even open the possibility of directed transport of intermediates between active sites in the case of multi-step reaction mechanisms.

Several synthetic strategies have emerged for encapsulation of metal particles in cavities to prepare coated catalysts. Nanotubes with open ends may be prepared, such as carbon nanotubes [30,31], or mesoporous silica materials [33,34], with subsequent or concurrent uptake of metal precursor solutions through an impregnation procedure; however selective deposition of metal particles in cavities is difficult, and the desirable confinement of metal particles is not wholly achieved in the continuous and open-ended support channels. Closed-shell (i.e., yolk-shell) structures, often termed “nanorattles” or “nanocapsules,” have been demonstrated from several synthetic routes. Template nanoparticles have been used, e.g., Au [35,36] and $CaCO_3$ [37] spheres or rods, which can be encapsulated and then partially removed by dissolution, leaving cavities. However, this limits the choice of catalytic metal, and sacrificial etching is not ideal. A similar route which preserves metal nanoparticles involves selective dissolution of inner shell material, leaving outer shell material and a hollow core [23,29,38,39]. Hollow particles with encapsulated core metal nanoparticles can be formed via the Kirkendall effect, wherein vacancies can diffuse radially inward during oxidation of initially fully reduced metal nanoparticles. These vacancies then nucleate and grow, leaving reduced metal particles in an internal cavity encapsulated by a polycrystalline oxide shell. The metal and coating oxide can be selected by forming appropriate initial core@shell particles, such as yolk-shell Pt@CoO from core@shell Pt-Co [20,40] and Au@SnO_2 from Au-Sn [*32*]; however the method may be difficult to generalize to many desirable catalytic materials.

This study reports a novel route for the preparation of hollow Ni@SiO_2 nanoparticles via a water-in-oil microemulsion template method, with possible application to a wide range of metals and coating oxides. Cavities in this case are formed by a localized polymerization or aggregation of the coating material precursor at the micelle interface, thus the shape of reverse-micelles becomes the template directing the final morphology. This effect has been

used in the formation of hollow silica nanospheres [41] and Fe@SiO_2 nanotubes [42], and a similar effect was recently demonstrated in the formation of M@SiO_2 (M = Au, Pt, Pd) nanospheres [43], though the phenomena underlying the formation and template capability of reverse-micelles in this study are significantly different than in these previous studies. Hollow Ni@SiO_2 nanoparticles have been shown by Veser and coworkers, however to date their procedure has not been described [25,44].

This study further reports an elongation phenomenon whereby Ni@SiO_2 nanotubes can be prepared. Experiments were performed to investigate synthesis variables which had a significant effect on nanotube formation and elongation (e.g., aging time prior to addition of the SiO_2 precursor, N_2H_4 concentration, and synthesis temperature), and to elucidate mechanistic insight thereof. Experimental Ni@SiO_2 materials were analyzed by TEM, H_2 chemisorption, N_2 physisorption, and ICP, for morphological observation and preliminary catalytic characterization.

Background of nanoparticle synthesis in a water-in-oil microemulsion template

The use of water-in-oil microemulsions for preparing metal nanoparticles was first reported by Boutonnet in 1982 [45]. Since then this procedure has been used to create uniform metal particles less than 10 nm in size for many transition metals and metal oxides, including Ni [46], Rh [47], Co [48], and Ce_xWO_4 [49]. The procedure involves forming a microemulsion, characterized as transparent, thermodynamically stable, and nanoscale in micellar droplet size, from a ternary system of oil, surfactant (e.g., cyclohexane and polyoxyethylene alkyl ether, respectively), and water.

Microemulsions are dynamic in that the contents of micelles are exchanged at a high rate, a process called intermicellar exchange. This process involves the collision of two micelles, the

formation of a fused dimer in which the internal phases of two micelles are joined through a neck in the surfactant interface, the transfer of species contained in the inner phases smaller than the neck constriction, and finally separation to re-form two micelles [50]. In general, particularly with nonionic surfactants, stronger interactions between surfactant and the associated oil and aqueous phases hinder intermicellar exchange. This includes longer hydrophilic and hydrophobic surfactant parts [51], longer or absent alcohol co-surfactant [50,52], and increased aqueous phase salinity [52]. Further, the intermicellar exchange rate increases with increasing droplet size, which increases with increasing water-to-surfactant ratio [50,52].

Many variables are known to affect the microemulsion structure, including the composition of water, oil, and surfactant; the salt concentration in the aqueous phase; the surfactant and oil types; and the temperature. Much work has been done to study the often heavily interrelated effects of these variables, leading to complex descriptions and phase diagrams of microemulsion systems. For example, Shinoda *et al.* reported phase diagrams for the nonionic system of water, the surfactant polyoxyethylene (10) cetyl ether ($C_{16}H_{33}(OCH_2CH_2)_{10}OH$, or $C_{16}E_{10}$), and the oil cyclohexane [53]. Their data shows the range of compositions and temperatures under which a stable water-in-oil microemulsion phase forms. Common considerations in forming a water-in-oil microemulsion template for nanoparticle synthesis are the maximum water content that can be fully solubilized in micelles [54]; the phase inversion temperature, below which an oil-in-water microemulsion is stable and above which a water-in-oil microemulsion is stable [55]; and the minimum surfactant concentration needed to form micelles [56]. These properties can be modified to suit specific syntheses by controlling the types of surfactant and oil and, in the case of nonionic surfactants, the lengths of the hydrophilic and hydrophobic groups [57].

Once a stable water-in-oil microemulsion is formed, a metal precursor salt is added, which solubilizes in the aqueous droplets, and is reduced to form metal particles by addition of a reductant (e.g., N_2H_4, $NaBH_4$, or H_2 gas) and a base (e.g., NH_3 or NaOH) [58]. The size control of

the metal nanoparticles is a primary goal, and much work has been done to understand the effects of water and surfactant concentrations, surfactant and oil types, metal precursor and reductant concentrations, and temperature on the final metal particle size [46,49,50,51,59,60,61]. The prevailing opinion regards standard nucleation and growth processes in bulk media, where the final particle size depends on the number of quickly formed nuclei and the extent of subsequent particle growth as they are determined by the above variables [46,60], though surfactant dynamics [50] or surfactant interaction with the metal particle surface to restrict excessive particle growth have also been reported [50,62,63]. The final particle size is commonly observed to be either limited by or proportional to the water-to-surfactant molar ratio [62].

Metal nanoparticles formed in a water-in-oil microemulsion template can be deposited on a pre-formed support. In such a preparation, the support is added to the microemulsion, and a micelle destabilizing agent such as tetrahydrofuran is added slowly to deposit the particles on the support surface [64]. Functionalizing the support with a silylation agent like octadecyltrimethoxysilane or hexamethyldisilazane to create a hydrophobic surface has been shown to prevent particle growth and retain the particle size distribution initially present in the microemulsion. Compared to conventional impregnated catalysts (and also core@shell catalysts), metal particles formed in a microemulsion and deposited on a preformed support have decreased interaction with the support and increased reducibility. This has been observed with Fe/SiO_2 [65], Co/SiO_2 [66], and Pt/TiO_2 [67]. This decreased metal-support interaction has been attributed to the loose contact between the support and preformed metal particles, in contrast with when the metal particles are formed from their precursors in the presence of the support [67]. In addition, the support silylation step has been suggested to reduce the metal-support interaction, where the hydrophobic support will interact with the organic phase and outer boundary of the reverse micelles rather than directly with the metal particles [66]. Metal nanoparticles having less interaction with the support may result in greater particle growth at elevated temperatures, but the stability of particles formed in microemulsion and deposited on supports at elevated temperature has not been reported.

The advantage of microemulsion techniques for controlling metal particle size with a narrow size distribution has been used to study particle size effects in catalytic reactions, with the additional benefit that size effects are not confounded with metal-support interactions [67]. Ojeda *et al.* prepared Rh particles in microemulsions of 5, 10, 20, and 30 nm, and deposited them on Al_2O_3. They found that smaller metal particles remained oxidized during the Fischer Tropsch reaction, leading to a higher selectivity to oxygenates than with larger particles [47]. For the same reaction, Trepanier *et al.* compared three Co catalysts, deposited on carbon nanotubes, with distinct particle size distributions in the range 3-10 nm, and found that reaction activities and product selectivities were dependent on metal particle size [48].

The first two reports of core@shell nanostructures were $Rh@SiO_2$ in 1995 [21] and $Pd@ZrO_2$ in 1997 [22], both studied as CO hydrogenation catalysts. Since then, various shell materials have been used to encapsulate a diverse range of metal, metal oxide, and metal alloy nanoparticles and other compounds that have drawn interest in catalytic and biomedical research [68,69]. Encapsulation of metal nanoparticles in SiO_2 shells is attractive in biomedical applications because SiO_2 is biologically compatible and hydrophilic, allowing greater utilization of the unique magnetic and imaging properties of metal nanoparticles. Core@shell nanostructured materials have been investigated for many catalysis applications, with shell materials including Al_2O_3 [17], CeO_2 [10], and (most commonly) SiO_2.

The synthesis of these core@shell materials in a water-in-oil microemulsion is similar to that of metal nanoparticles, with the difference that complete reduction of the metal precursor is not required before addition of the shell precursor (e.g., tetraethyl orthosilicate (TEOS) in the case of SiO_2). The reductant (e.g., N_2H_4) is commonly added to the water-in-oil microemulsion containing the solubilized metal precursor, as before, however its purpose is to complex and localize metal precursor ions that will be encapsulated [64]. Encapsulating metal nanoparticles in a shell material like SiO_2 contrasts with depositing metal nanoparticles formed in microemulsion on a support in that in the latter case the particle size distribution formed in the

microemulsion is retained while in the former case several microemulsion particles can be encapsulated into a single core@shell particle [70], slightly increasing the final metal particle size and broadening the size distribution.

Microemulsion dynamics may influence the shell pore size in core@shell materials. In the case of SiO_2 shells, fast TEOS hydrolysis and condensation in droplets results in numerous, compartmentalized nuclei, and the growth of SiO_2 shells is the aggregation of smaller condensed TEOS moieties as they are transported between droplets [28]. This assembly process leaves spaces open in the SiO_2 shell, creating the pore network. It is reasonable to hypothesize that the pore structure and hence pore size distribution are dependent on intermicellar exchange.

Experimental

The synthesis procedures used in this work were adapted from the procedure reported by Kishida and coworkers for Ni@SiO_2 nanospheres [13]. Chemical reagents used for Ni@SiO_2 syntheses were obtained from Sigma Aldrich. $Ni(NO_3)_2 \cdot 6H_2O$ was dissolved in DI water to create a 0.38 M solution, used as the Ni precursor. $N_2H_4 \cdot H_2O$ was used as a reductant/complexing agent. Ammonium hydroxide solution (ca. 29 wt%) was diluted as needed to achieve desired NH_3/H_2O mole ratios during synthesis. Cyclohexane (C_6H_{12}) was used to form the oil phase, and polyoxyethylene (10) cetyl ether ($C_{16}E_{10}$) was used as the nonionic surfactant. Tetraethyl orthosilicate (TEOS, $Si(OCH_2CH_3)_4$) was used as the silica precursor.

Ni@SiO_2 syntheses were performed in an open 250 mL Pyrex flask. A Teflon-coated stir bar and stir plate were used for mixing at a constant power setting for all experiments. The temperature of the synthesis mixture was controlled using resistive heating from the stir plate surface and a thermocouple inserted directly into the mixture, with a corroborating thermometer.

For each synthesis, 100 mL of a 0.5 M solution of $C_{16}E_{10}$ in cyclohexane was set stirring and heated to 50°C. When the solution had attained the set point temperature and a transparent microemulsion was observed, $Ni(NO_3)_2$ solution, $N_2H_4 \cdot H_2O$, and NH_3 solution were added (in that order) to achieve 62 mg Ni, N_2H_4/Ni (molar basis) = 45, NH_3/H_2O (molar basis) = 0.039, and W (water-to-surfactant mole ratio) = 23. After a period of aging which was experimentally varied, TEOS was added. The microemulsion was then further aged for 2 hr to allow hydrolysis and condensation of TEOS. At the end of each synthesis, ca. 30 mL of isopropanol was added to the mixture to destabilize the microemulsion structure. Ni@SiO_2 particles were separated by centrifuging at 3000 rcf, and the resulting pellet was washed twice with ca. 30 mL isopropanol, followed each time by additional centrifugation. The washed material was dried overnight at ca. 100°C, then calcined at 500°C for 2 hr in flowing air, and finally reduced at 700°C for 2 hr in flowing H_2.

To investigate the formation of silica nanotubes, synthesis experiments were performed with varying aging time prior to TEOS addition, varying N_2H_4 concentration, and varying temperature. The variable values for these experiments are listed in Table 2.1. Additionally, an experiment with the Ni precursor substituted with additional water to maintain W = 23, and an experiment with the order of addition of N_2H_4 and NH_3 reversed, were performed. The amount of TEOS was also varied to investigate control of silica shell thickness (Table 2.2).

Table 2.1 $Ni@SiO_2$ synthesis experiments varying aging time prior to TEOS addition, N_2H_4 concentration, and temperature.

Experiment	Aging time (hr)	N_2H_4/Ni (molar)	Temperature (°C)
Base case	3	45	50
Varying aging time	5 min	45	50
	1.5		
	6		
	24		
Varying N_2H_4 concentration	3	3	50
		12	
		24	
Varying temperature	3	45	46
			54

TEM bright field imaging, performed to observe $Ni@SiO_2$ particle morphology and dimensions, was accomplished using a JEOL 3011 HRTEM with 300kV accelerating voltage from a LaB_6 thermoelectric emission gun. To avoid fouling due to residual organic species, most TEM specimens were prepared from samples following the 500°C calcination step. Ca. 1 mg of powder was suspended in 1 mL of ethanol and ultrasonicated for 1 hr. A drop of each suspension was placed on a 3 mm carbon film Cu grid to form the TEM specimen. TEM images were analyzed to generate histogram distributions of particle dimensions, including $Ni@SiO_2$ nanotube shell thickness, cavity diameter, and cavity length. At least 100 particles were used for each distribution. All distributions were normalized; the number of measurements at each bin value was divided by the bin width and the total number of measurements to obtain the reported measurement frequency. Additionally, the prevalence of the nanotube morphology compared to the solid nanosphere morphology was quantified as the observed number of nanotube particles divided by the total number of particles observed. The equations used for calculating the above values are given below. Cavity length, L_{cavity}; cavity cross-sectional area and perimeter, A_{cavity} and P_{cavity}, respectively; and cross-sectional area enclosed by the outer particle surface and particle perimeter, $A_{particle}$ and $P_{particle}$, respectively; were measured directly from TEM images. $N_{nanotubes}$ is the number of observed nanotubes for a sample, and $N_{spheres}$ is the number of observed solid nanosphere particles.

Silica shell thickness (cross-sectional average) =

$$\frac{2\left(A_{\text{particle}} - A_{\text{cavity}}\right)}{P_{\text{particle}} + P_{\text{cavity}}}$$

Cavity diameter, d_{cavity}, calculated from (assuming cylindrical cavities with hemispherical ends):

$$\frac{\pi}{4} d_{\text{cavity}}{}^2 + d_{\text{cavity}}\left(L_{\text{cavity}} - d_{\text{cavity}}\right) = A_{\text{cavity}}$$

Nanotube morphology fraction =

$$\frac{N_{\text{nanotubes}}}{N_{\text{nanotubes}} + N_{\text{spheres}}}$$

Apparent metal dispersions of samples were measured using H_2 chemisorption with a Micromeritics ASAP 2020 instrument. Measurements were taken of reduced samples (i.e., samples having been treated at 500°C in air and at 700°C in H_2) at 35°C following additional in-situ reduction at 650°C in flowing H_2 for 2 hr. H_2 uptake was measured twice with intermittent evacuation. The first measurement represented physisorbed plus chemisorbed gas, and the second represented physisorbed gas only. The difference in uptake, averaged at several partial pressures of adsorbate gas, was taken as representative of metal surface area. To calculate metal particle size and dispersion, an adsorption stoichiometry of 0.5 H_2/Ni surface atom, a cross sectional area of 0.0649 nm^2 per Ni surface atom, and a spherical Ni particle geometry were assumed.

Physical surface areas of samples were calculated using the Brunauer-Emmett-Teller (BET) model, using N_2 physical adsorption (physisorption) measurements also taken with a Micromeritics ASAP 2020 instrument. Measurements of N_2 uptake for BET calculations were taken of reduced samples in the range of relative pressures of 0.11 to 0.30. The highest-frequency (on the basis of pore volume) intraparticle pore size in the distribution of pore sizes smaller than 5 nm was calculated using the Horvath-Kawazoe model with the Saito-Foley

modification for cylindrical pore geometry, using N_2 uptake measurements in the range of relative pressures less than 0.10. Prior to N_2 physisorption analysis, samples were held under vacuum (less than 10 μmHg) at 350°C overnight to remove water and gases from the material.

The elemental composition of Ni@SiO_2 samples was quantitatively analyzed using a Varian 710-ES Inductively Coupled Plasma Optical Emission Spectrometer (ICP-OES), equipped for axial viewing with a 1.12 megapixel CCD detector, sensitive to wavelengths in the range 177-785 nm. For these analyses reduced powder samples were dissolved in equal volumes concentrated nitric and hydrofluoric acids, with later hydrochloric acid addition to dissolve remaining Ni particles. ICP results were used to calculate Ni loading (i.e, Ni mass fraction in sample) and fractional SiO_2 yield for each sample according to the following equations:

$$\text{Ni loading} = \frac{x_{\text{Ni}}}{x_{\text{Ni}} + x_{\text{Si}} \dfrac{M_{\text{SiO}_2}}{M_{\text{Si}}}}$$

$$\text{Fractional SiO}_2\text{ yield} = \frac{m_{\text{Ni}} \dfrac{x_{\text{Si}}}{x_{\text{Ni}}}}{m_{\text{TEOS}} \dfrac{M_{\text{Si}}}{M_{\text{TEOS}}}}$$

where x_i is the weight fraction of species i measured by ICP, M_i is the molar weight of species i, and m_i is the total mass of species i used for a sample during synthesis. The fractional SiO_2 yield calculation assumes complete encapsulation of Ni.

Results

Effect of aging time

$Ni@SiO_2$ samples were synthesized with varying aging time preceding TEOS addition to observe effects on the incidence of SiO_2 nanotube morphology and elongation. For these experiments, the microemulsion containing $Ni(NO_3)_2$, N_2H_4, and NH_3 was aged for 5 min, 1.5 hr, 3 hr, 6 hr, and 24 hr before TEOS addition. TEM images of the resulting calcined $Ni@SiO_2$ samples are shown in Figure 2.1. The number of particles containing a distinct cavity increased relative to solid nanosphere particles up to 3 hr aging, where almost only nanotubes were observed, and then decreased for 6 hr aging to a nanotube morphology fraction of 0.67.

For nanotube particles, cavity diameter and length were measured for at least 100 particles in each sample (except for 24 hr aging), and their distributions are shown in Figure 2.1(g) and (h). Cavity diameter distributions were similar with varying aging times, with an average diameter of 12-13 nm. Any correlation of cavity diameter with length or aging time was within the error of the diameter measurement (ca. 0.5 nm) and random experimental variations (e.g., 1-2°C temperature fluctuations). The cavity length distribution, however, shifted to larger values with increasing aging time, with the highest-frequency values increasing as 24.8, 33.9, 35.5, and 45.3 nm for 5 min, 1.5 hr, 3 hr, and 6 hr aging, respectively. For 24 hr aging, maximum cavity lengths were as high as 2 μm.

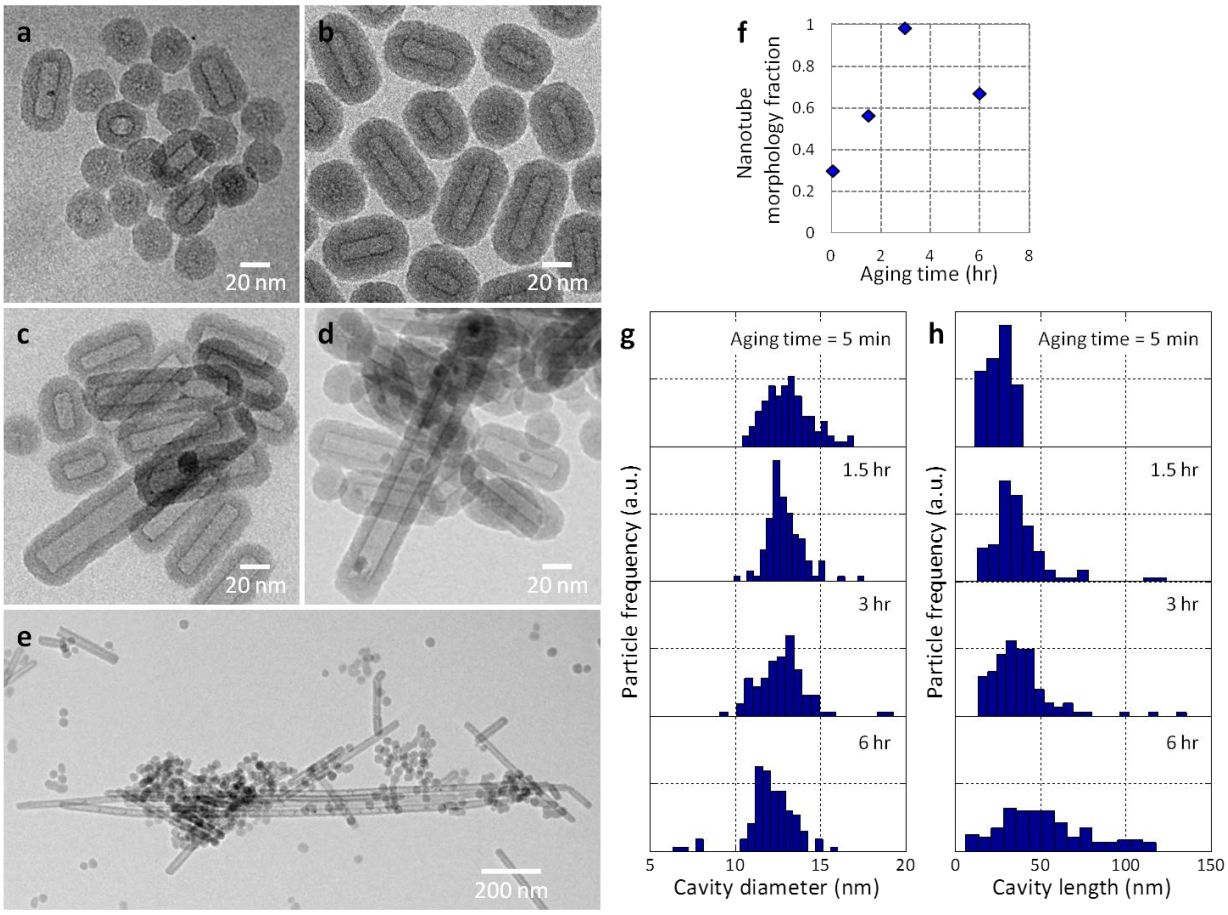

Figure 2.1 TEM images of calcined Ni@SiO_2 samples synthesized with varying aging time prior to TEOS addition: (a) 5 min, (b) 1.5 hr, (c) 3 hr, (d) 6 hr, and (e) 24 hr. (f) Nanotube morphology fraction, (g) nanotube cavity diameter distribution, and (h) nanotube cavity length distribution with varying aging time. N_2H_4/Ni = 45; 50°C synthesis temperature.

Effect of N_2H_4 concentration

The effects of varying N_2H_4 concentration on the incidence of SiO_2 nanotube morphology and elongation were observed in experiments with N_2H_4/Ni (molar) values of 3, 12, 24, and 45. N_2H_4/Ni = 3 is stoichiometric for complete complexation of Ni^{2+} ions, given the bidentate character of hydrazine and assuming octahedral coordination to Ni^{2+} centers. Hydrazine complexation has been widely used for localizing metal ions within micelles before encapsulation with SiO_2 or other materials. Complete reduction of Ni^{2+} to Ni nanoparticles through $2Ni^{2+} + N_2H_4 + 4OH^- \longrightarrow 2Ni + N_2 + 4H_2O$ requires N_2H_4/Ni = 0.5, but has not been

regarded as a requirement; encapsulation is sufficient to maintain a high metal dispersion until subsequent dry reduction treatments. Indeed, the encapsulating material precursor is typically added shortly after N_2H_4, without allowing time for the reduction reaction [70], which would require on the order of 2 hr to reach completion at temperatures near 50°C [71]. N_2H_4 concentrations greater than the equivalent of N_2H_4/Ni = 3 have not been reported.

TEM images of calcined Ni@SiO_2 samples synthesized with varying N_2H_4 concentrations are shown in Figure 2.2. For N_2H_4/Ni values of 3 and 12, particles with distinct cavities were not observed, but only solid nanospheres were formed, consistent with reports in the literature for similar systems [13]. The distinct nanotube morphology appeared at N_2H_4/Ni = 24, though nanotubes were relatively less numerous than nanospheres, and at the base case N_2H_4/Ni = 45 almost only nanotubes were observed.

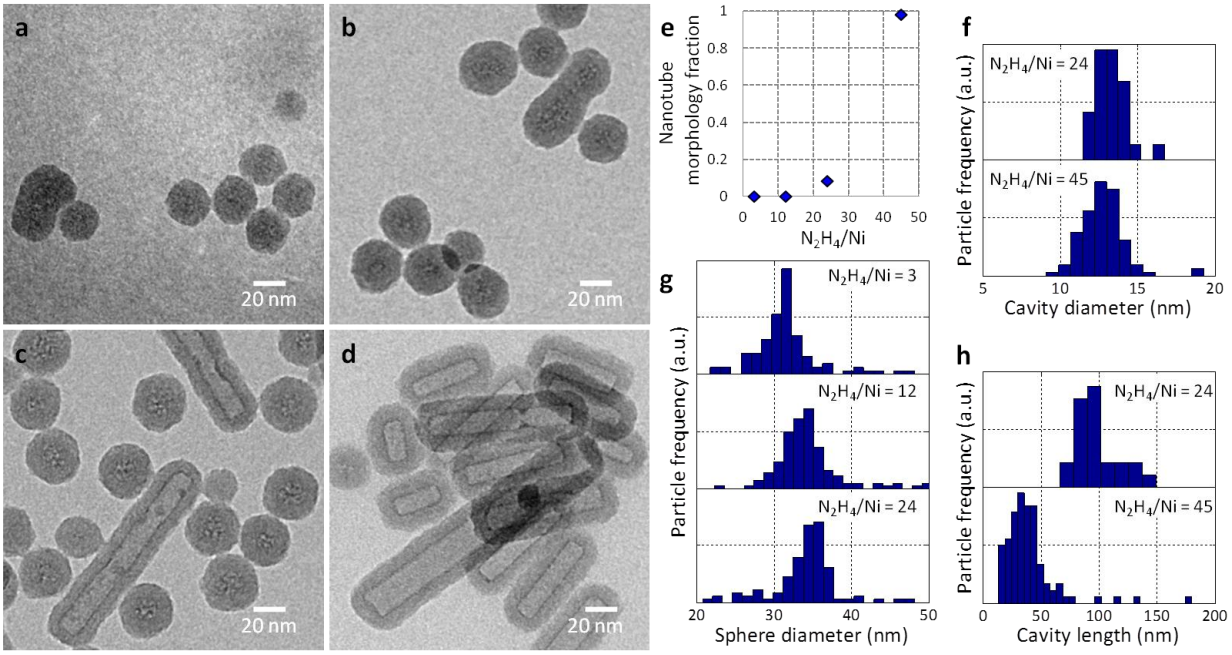

Figure 2.2 TEM images of calcined Ni@SiO_2 samples synthesized with varying N_2H_4 concentration: (a) N_2H_4/Ni = 3, (b) N_2H_4/Ni = 12, (c) N_2H_4/Ni = 24, (d) N_2H_4/Ni = 45. (e) Nanotube morphology fraction, (f) nanotube cavity diameter distribution, (g) nanosphere diameter distribution, and (h) nanotube cavity length distribution with varying N_2H_4 concentration. 3 hr aging before TEOS addition; 50°C synthesis temperature.

Cavity diameter and length distributions representing 24 and 100 nanotube particles for N_2H_4/Ni = 24 and 45 samples, respectively, are shown in Figure 2.2(f) (N_2H_4/Ni = 3 and 12

samples without nanotube particles not applicable). Interestingly, only very long cavity lengths were observed in a narrow distribution with a highest frequency of 97.6 nm for N_2H_4/Ni = 24, compared to 35.5 nm for N_2H_4/Ni = 45. Cavity diameter distributions were similar for N_2H_4 = 24 and 45 samples, with average diameters of 12.7 and 13.3 nm, respectively, differing on the order of measurement uncertainty and experimental error.

The dimensions of solid spherical particles for N_2H_4/Ni = 3, 12, and 24 samples (the N_2H_4/Ni = 45 sample with few solid spherical particles not included) were compared using diameter distributions representing at least 100 particles each, shown in Figure 2.2(g). Diameter distributions shifted to higher values with increasing N_2H_4 concentration, and average diameters were 31.6, 34.5, and 35.2 nm for N_2H_4/Ni = 3, 12, and 24, respectively. The increase in sphere diameters is consistent with the observation of small cavity-like features within spherical particles observed in TEM images for N_2H_4/Ni = 12 and 24 samples, suggesting that at increased N_2H_4 concentration, the spherical particles became less solid.

Effect of temperature

Temperature is a difficult variable to manipulate in microemulsion systems due to the inter-related dependencies of microemulsion phase, surfactant hydrophilicity/hydrophobicity, intermicellar exchange rate, and potentially of N_2H_4/NH_3 decomposition and Ni^{2+} reduction rates. However, experiments with varying temperature were used to investigate effects on SiO_2 nanotube formation and elongation, as such effects could still be revealing of underlying phenomena. Relatively small variations in temperature were investigated (i.e., 46, 50, and 54°C), so as to remain in the nominal water-in-oil reverse-micellar phase at 50°C.

TEM images for calcined Ni@SiO_2 samples synthesized at different temperatures are shown in Figure 2.3. Compared to the sample synthesized at 50°C, the 46 and 54°C samples both had a

smaller fraction of particles with nanotube morphology. The 46°C sample additionally had many non-spherical particles in the population of solid particles.

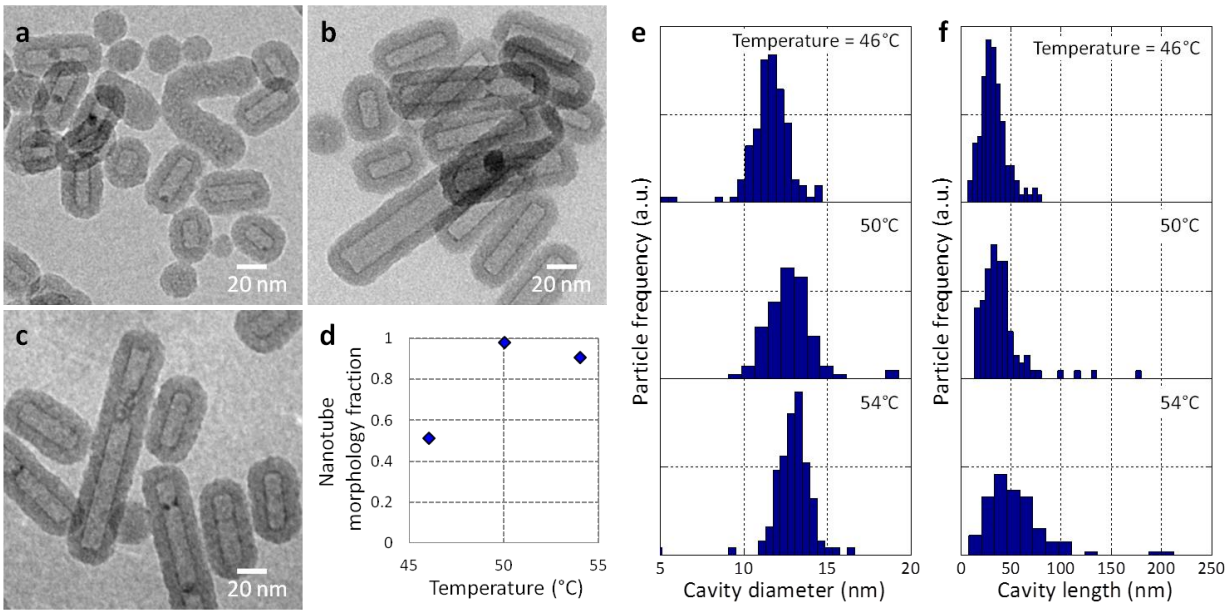

Figure 2.3 TEM images of calcined Ni@SiO_2 samples synthesized with varying synthesis temperature: (a) 46°C, (b) 50°C, and (c) 54°C. (d) Nanotube morphology fraction, (e) nanotube cavity diameter distribution, and (f) nanotube cavity length distribution with varying synthesis temperature. 3 hr aging before TEOS addition; N_2H_4/Ni = 45.

Cavity diameter and length distributions representing at least 100 nanotube particles in each sample are shown in Figure 2.3(e) and (f). With increasing temperature, the distributions of cavity length shifted to larger values with maximum frequencies of 30.1, 35.5, and 46.5 nm for samples synthesized at 46, 50, and 54°C, respectively. Interestingly, cavity diameter distributions were seen to shift to larger values with increasing temperature, with average values of 11.6, 12.7, and 13.1 nm for 46, 50, and 54°C, respectively. This contrasts with results for varying aging time prior to TEOS addition and N_2H_4 concentration experiments, where cavity diameter distributions were seen to remain constant, despite significant differences in length distributions.

Effect of TEOS amount

To investigate the possibility of controlling the SiO_2 shell thickness of Ni@SiO_2 particles, an important potential optimization variable, base case synthesis experiments were performed with varying amounts of TEOS. Accounting for the amounts of TEOS used and the resulting fractional SiO_2 yields calculated from ICP results, samples with Ni loadings of 2.5, 3.4, 5.1, and 13% were achieved (shown in Table 2.2). In each sample the number fraction of nanotube particles was high (>95%). As expected, TEM images (Figure 2.4) of samples showed visually decreased shell thicknesses as Ni loading increased. Shell thickness distributions representing at least 100 particles in each sample showed quantitatively that shell thickness decreased with increasing Ni loading, with average shell thicknesses of 12.4, 8.8, 7.8, and 5.1 nm for 2.5, 3.4, 5.1, and 13% Ni loading, respectively. Nanotube cavity diameter and length distributions were similar between samples, with variations in average diameters and highest frequency lengths being on the order of measurement uncertainty and experimental error.

Table 2.2 Measured properties of reduced Ni@SiO_2 samples with varying shell thickness.

TEOS amount (g)	Fractional silica yield[a]	Ni mass loading[a]	Silica shell thickness[b] (nm)	Ni dispersion[c]	Ni particle size[c] (nm)	BET surface area[d] (m^2/g)	Pore size[e] (nm)
10	83%	2.5%	12.4	14.2%	7.1	67	1.05
10	62%	3.4%	9.8	14.2%	7.1	78	0.90
5	81%	5.1%	8.8	15.4%	6.6	98	0.92
2	71%	13%	5.1	9.5%	10.7	-	-

[a]Calculated from ICP measurements
[b]Measured from TEM images
[c]Measured by H_2 chemisorption
[d]Measured by N_2 physisorption
[e]Highest-frequency intraparticle pore size, measured by N_2 physisorption

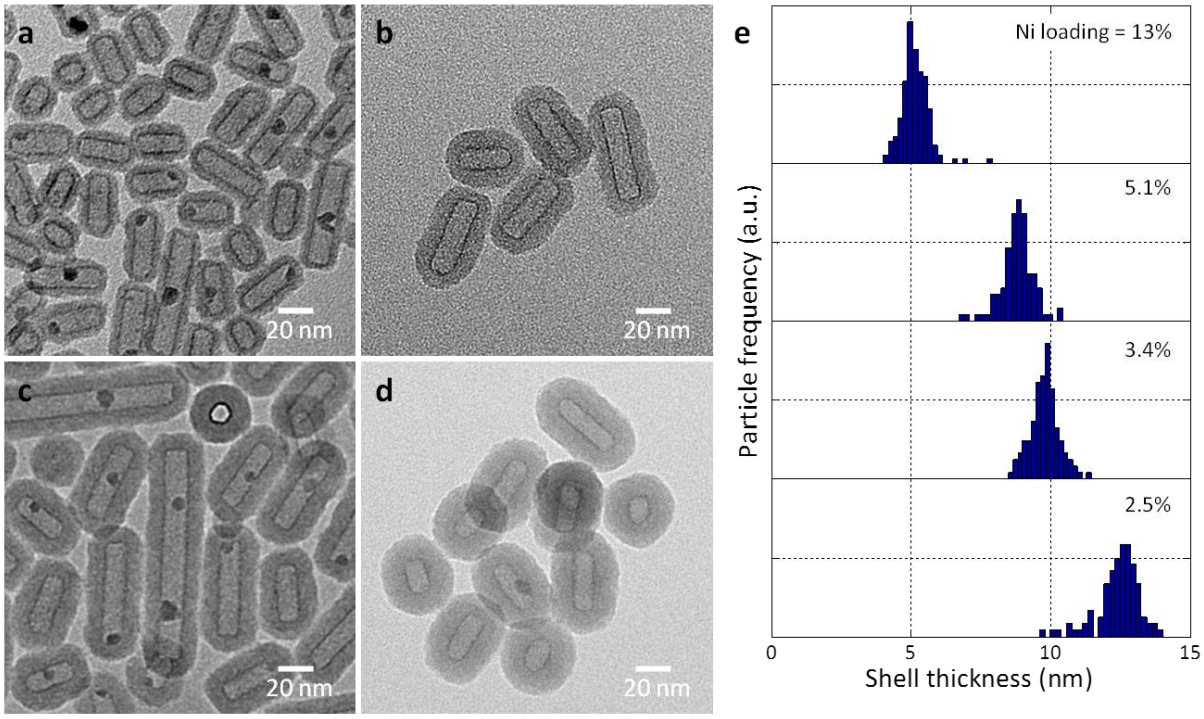

Figure 2.4 TEM images of calcined Ni@SiO_2 samples synthesized with varying Ni loading: (a) 13%, (b) 5.1%, (c) 3.4%, and (d) 2.5%. (e) Nanotube shell thickness distribution with varying Ni loading. 3 hr aging before TEOS addition; N_2H_4/Ni = 45; 50°C synthesis temperature.

Synthesis without Ni precursor

The synthesis procedure for Ni@SiO_2 was performed without the addition of $Ni(NO_3)_2$ solution, but with additional water to maintain W = 23. The synthesis temperature used was 50°C, the N_2H_4 concentration was the same as with Ni present, and the microemulsion was aged 3 hr after NH_3 addition, before TEOS addition. As shown by the TEM image in Figure 2.5(a), the resulting SiO_2 nanoparticles were smaller, ca. 10 nm, and less symmetric without Ni. No cavity formation or elongation features were observed, revealing the significant role of Ni on the final SiO_2 morphology.

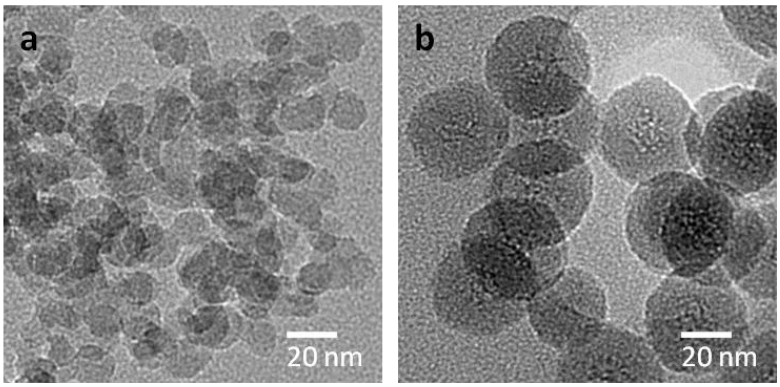

Figure 2.5 (a) TEM image of calcined SiO_2 sample from base case synthesis except with $Ni(NO_3)_2$ replaced with equivalent amount of H_2O. (b) TEM image of calcined $Ni@SiO_2$ sample from base case synthesis except with addition of N_2H_4 following addition of NH_3. 3 hr aging before TEOS addition; N_2H_4/Ni = 45 (or equivalent N_2H_4 concentration); 50°C synthesis temperature.

Synthesis with NH_3 addition before N_2H_4

A synthesis procedure for $Ni@SiO_2$ was performed with the addition of N_2H_4 following that of NH_3. The hypothesis was that the later addition of N_2H_4 would result in less extensive complexation with Ni^{2+}, which would instead be bound with harder NH_3 ligands. This would suppress Ni nanoparticle formation by hindering the reduction of Ni^{2+}. Thus observation of the morphology of the resulting SiO_2 particles was expected to reveal the dependence of cavity formation and elongation on the formation of Ni nanoparticles.

As shown by the TEM image in Figure 2.5(b), the resulting SiO_2 nanoparticles were spherical and slightly larger than nanospheres observed in other samples, with an average diameter of ca. 40 nm, and distinct cavities were not observed. SiO_2 particles did appear to contain small cavity-like features, similar to the cases of $Ni@SiO_2$ synthesized with intermediate N_2H_4 concentrations, but it is clear that the effect that is responsible for producing cavities is significantly reduced compared to the cases where N_2H_4 was added before NH_3.

Metal particle accessibility – H_2 chemisorption

The Ni@SiO_2 sample series with varying silica shell thickness, calcined in air at 500°C and reduced in H_2 at 700°C, were evaluated with H_2 chemisorption to determine the accessibility of Ni metal surface area to an external gas phase, an initial catalytic characterization. According to results, shown in Table 2.2, silica porosity was sufficient with all shell thicknesses in the range of 5.1 to 12.4 nm for H_2 diffusion to and chemical adsorption on Ni particle surfaces. No correlation of accessible Ni surface area with shell thickness was apparent.

Physical surface area and pore structure – N_2 physisorption

The Ni@SiO_2 sample series with varying shell thickness, calcined in air at 500°C and reduced in H_2 at 700°C, were also analyzed with N_2 physisorption to measure physical surface area and pore size to further characterize the accessibility of encapsulated Ni particles to external gas phase species. The sample with a shell thickness of 5.1 nm could not be analyzed due to the limited amount of powder obtained with its relatively low silica composition. BET surface areas and highest-frequency intraparticle pore sizes for the other samples are given in Table 2.2. BET surface areas increased with decreasing shell thickness, which is reasonable considering that the distribution of particle shapes remains constant with varying shell thickness, and particle mass varies more significantly than particle surface area with varying shell thickness. Results also confirmed the presence of pore sizes on the order of 1 nm, consistent with previous studies [27,28,29].

Discussion

The results of Ni@SiO_2 synthesis experiments with varying aging time before TEOS addition, N_2H_4 concentration, temperature, and TEOS amount, which formed SiO_2 nanotubes of highly uniform cavity diameter and solid SiO_2 nanospheres, give insight into the mechanism of cavity

formation and elongation. Evidence suggests that the final Ni@SiO_2 particle morphology arises from the micelle structure at the time of addition of the silica precursor; micelles are elongated prior to TEOS addition. For instance, varying aging times before TEOS addition, up to 24 hr, resulted in signficantly different nanotube lengths, up to on the order of microns, whereas the TEOS hydrolysis and condensation step required only 2 hr in each case (with > 50% SiO_2 yield confirmed by ICP for all samples). Moreover, it is expected that the cavity space of eventual nanotubes is encapsulated at an early stage of the TEOS hydrolysis and condensation step. Therefore it can be ruled out that the particle cavities and their elongation are the result of anisotropic growth of silica particles during the hydrolysis and condensation step, as has been observed elsewhere [72]. Rather, they are the result of developed micelle shapes.

Cavities are the result of TEOS-to-SiO_2 conversion occurring in the outer regions of micelles. This might occur due to fast hydrolysis and condensation taking place at the surfactant interface, a potential result of increased ionic activity near the interface, as has been seen in other studies in which hollow SiO_2 particles were formed from a water-in-oil microemulsion template [41,42]. However, incidence of cavities is dependent on time, coincidently with Ni^{2+} reduction by N_2H_4, and the latter decreases the concentrations of Ni^{2+} and OH^- over time. Additionally, N_2H_4 concentration, having a strong effect on cavity formation, is not expected to have a significant effect on TEOS conversion kinetics. The formation of SiO_2 nanospheres instead of nanotubes when N_2H_4 was added after NH_3 suggested that cavity formation was also dependent on N_2H_4-Ni complexation or reaction. Cavity formation was furthermore dependent on the presence of Ni species, as shown by the experiment without the Ni precursor. In the latter case micelles appear to have been smaller, possibly a result of a smaller aggregation number in the absence of Ni.

It seems rather that hydrolyzed TEOS species are excluded from inner micellar regions, due to the presence of a separate phase immiscible with the aqueous phase. It is hypothesized here that cavities are a result of formation of gases produced by reduction of Ni^{2+} by N_2H_4, and possibly by further decomposition of N_2H_4 and/or NH_3 catalyzed by reduced Ni particles. The

timescale of both Ni^{2+} reduction and N_2H_4 decomposition to N_2 and H_2 gases in the presence of Ni nanoparticles has been shown to be on the order of 2 hr at 50°C [71], consistent with the timescale of cavity formation and elongation observed in this study. The significance of Ni particle formation is consistent with the results of the experiments with Ni removed and with N_2H_4 added after NH_3, both having not formed nanotube structures.

Elongation of SiO_2 structures occurs only for nanotubes with well-defined cavities, and is dependent on time, indicating the elongation is not a purely thermodynamic effect, and is likewise with cavity formation a result of gas formation inside micelles. Elongated rodlike or cylindrical micelles are well-known for oil-in-water (o/w) microemulsions. They form as a result of increased surfactant aggregation number with suppression of electrostatic repulsion between hydrophilic head groups and/or favorable interaction of hydrophobic tail groups with a solubilized organic phase [73,74,75]. In general, increased solubilized volume, increased entropy of conformation of hydrophobic groups of surfactants, favorable enthalpy of mixing of hydrophobic surfactant groups and solubilized molecules, and decreased water-oil interface energy will tend to increase aggregation number and cause formation of elongated micelles, while electrostatic repulsion between charged hydrophilic surfactant groups will tend to cause spherical micelle shapes. The elongation of reverse-micelles in water-in-oil microemulsions is a less prevalent effect, and typically lower aggregation numbers are favored. Instances of elongation have been observed for nonionic surfactant systems when the hydrophobic groups of surfactants become less miscible with the continuous oil phase, such as with lower temperature, shorter alkyl chain length of the surfactant, and larger size of oil molecules [76,77]. These elongation effects are enhanced by solubilization of water in reverse-micelles [78]. Elongation is further effected when favorable mixing of hydrophilic surfactant groups and the aqueous phase occurs, such as for ionic surfactant systems with solubilization of aqueous ionic compounds [42].

The phenomenon reported here, however, cannot be explained solely by the above thermodynamic considerations. It is reasonable that an increased aggregation number could

result from a growing volume in micelle droplets of an entrained gas phase, however the formation of elongated rather than large spherical micelles does not have an obvious explanation. Possibly one-dimensional growth (as opposed to spherical) would maintain a larger surface area per surfactant molecule and accordingly a lower conformational free energy of alkyl chains. Micelle diameter, then, would be a thermodynamic property, which is consistent with the result of relatively uniform SiO_2 nanotube diameters throughout all experiments, except the series with varying temperature. The observation that the degree of elongation increases with increasing temperature, despite the increased hydrophobicity of the surfactant, which would tend to favor spherical micelles, shows the strength of the driving force towards elongation arising from a gas phase formed in micelles. Indeed, if the formation of gas phases in micelles is the dominant driving force to cavity formation and elongation, then, assuming no departures from a primarily spherical reverse-micellar phase, rates of reactions leading to gas products increase with increasing temperature, and therefore the degree of elongation should increase with increasing temperature (though not necessarily the number fraction of nanotube particles). The elongation of reverse-micelles via the formation of a gas phase in micelles, and furthermore the encapsulation of these micelle templates with an aggregated solid, in this case SiO_2, are both considered novel results.

The results of this study suggest the micelle elongation profile depicted in the scheme in Figure 2.6. Accepting the hypothesis that micelles elongate due to formation and entrainment of a gas phase, nanotube elongation is theoretically limited by the amount of potential gas evolution, and therefore excessive aging times may result in a shortening of nanotubes as gas escapes. However, the potential length of nanotubes seems to be at least on the order of 2 microns. Interestingly, it appears that over time the length distribution of micelles shifts to increasing values, even after the fraction of elongated micelles begins to decrease with time after reaching a maximum for 3 hr aging. This indicates that over extended periods of gas production and intermicellar exchange, gas phases entrained in micelles tend to coalesce, causing extensive elongation of a decreasing number of micelles, while spherical micelles are formed which do not contain Ni^{2+} or decomposition reactants (i.e., gas precursors). This is consistent with the

results for the N_2H_4/Ni = 24 sample, which after 3 hr aging appeared to have only long micelles with a highest-frequency cavity length of 97.6 nm and spherical micelles with only trace evidence of cavities. These results reveal a certain "stability" of elongated micelles, in that shorter elongated micelles do not develop as time progresses, but only spherical micelles. Thus scission of elongated micelles was not evident, but only separation of a sufficient number of surfactant molecules to form spherical aggregates. This profile of gas-induced micelle elongation is consistent with the current understanding of microemulsion dynamics, which regards the collision of two micelles to form a fused dimer with transient continuous inner phase, ensuing transport of solubilized species (in this case gases), and finally fission to re-form separate micelles [50,52,79,80].

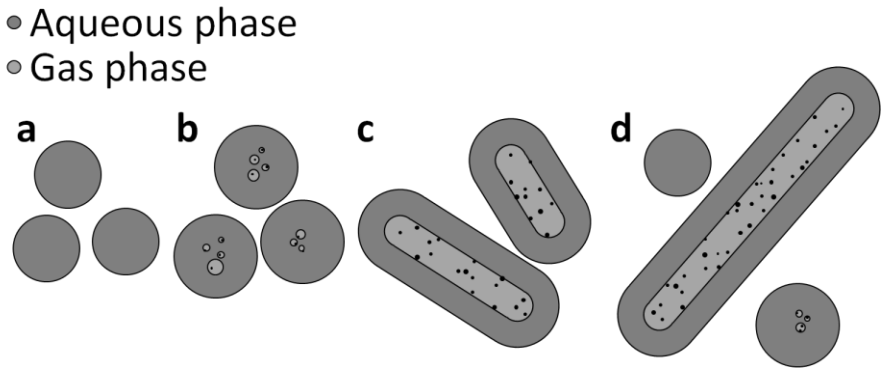

Figure 2.6 Schematic illustration of gas-induced elongation profile of reverse-micelles over time. (a) Initial spherical reverse-micelles containing Ni^{2+} and N_2H_4, (b) larger spherical micelles containing small amounts of entrained gas, (c) elongated micelles with distinct gas phases and reduced Ni nanoparticles, and (d) further elongated micelles with re-formed spherical micelles.

It is clear from TEM images that Ni was completely encapsulated by silica during syntheses of Ni@SiO_2. After the drying step at ca. 100°C, Ni particles, formed via the reduction of Ni^{2+} by N_2H_4, were highly dispersed on the inner shell surfaces (i.e., cavity walls) of nanotubes, as seen in Figure 2.7(a). After calcination in air at 500°C, NiO species remained highly dispersed on the inner shell surfaces, and only larger NiO agglomerates were visible by TEM, as seen in Figure 2.7(b). After reduction in H_2 at 700°C, denser, larger Ni particles formed (though still well-dispersed), as seen in Figure 2.7(c).

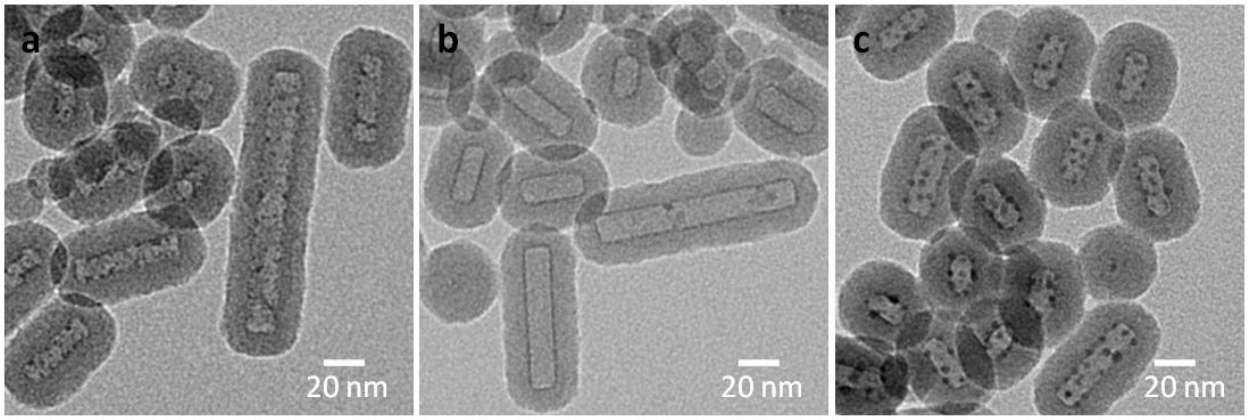

Figure 2.7 TEM images of Ni@SiO_2 nanotubes (a) after synthesis and drying at ca. 100°C, (b) after calcination at 500°C in air, and (c) after reduction at 700°C in H_2. 3 hr aging before TEOS addition; N_2H_4/Ni = 45; 50°C synthesis temperature.

Therefore, for Ni@SiO_2 nanotube materials to be considered for catalytic applications, the silica shell must be sufficiently porous to permit transport of species in the external phase to and from the encapsulated active metal sites, and also thin enough to avert excessive mass-transport limitations. A wide range of core@shell nanoparticles that meet these constraints are emerging in the literature, a notable example being Pd@SiO_2 for catalytic oxidation of various large alcohols such as benzyl alcohol [43]. Here it is shown that the silica shell thickness may be controlled in the range of 5.1 to 12.4 nm by varying the amount of silica precursor used, presenting a simple method for optimizing transport rates. Accessibility of the surfaces of encapsulated particles was confirmed by H_2 chemisorption measurements, even for shell thicknesses as large as 12.4 nm. Chemisorption results predicted metal particles sizes larger than those apparent from TEM images of reduced samples (e.g., Figure 2.7(c)), suggesting that a fraction of Ni particle surfaces were inaccessible to H_2, possibly due to contact with SiO_2. Interestingly, the thinnest-shell sample was observed to have the lowest Ni dispersion, which could be a result of increased growth of NiO in this sample during calcination compared to others, suggested by the TEM image in Figure 2.4(a). Intraparticle pore sizes on the order of 1 nm were measured by N_2 physisorption in the samples with shell thicknesses of 8.8, 9.8, and 12.4 nm (Table 2.2), which was consistent with the conclusion that metal particle surfaces are accessible to molecular species in the external phase via pore diffusion.

These results validate the inclusion of the novel Ni@SiO_2 nanotube materials reported in this study in the developing class of M_1@M_2O_x yolk-shell materials in catalyst research. The comparative evaluation of Ni@SiO_2 nanotubes, Ni@SiO_2 nanospheres, and impregnated Ni/SiO_2 for autothermal reforming of propane will be the subject of the following chapter.

Conclusion

A novel technique is reported for the synthesis of Ni-containing SiO_2 nanotubes of uniform diameter and tunable length, up to 2 microns, in a water-in-oil microemulsion template. The strong dependence of nanotube formation on N_2H_4 concentration and aging time prior to introduction of the silica precursor, along with other experimental evidence, led to the hypothesis that a gas phase formed and remained entrained in reverse-micelles, causing both micelle elongation and the exclusion of agglomerating Si species to outer micellar regions. This synthesis technique has potential for fabrication of other nanotube materials, which may have different encapsulated metals, shell materials, and gas phase precursors. According to preliminary experimental results, the synthesis method may, with some modifications, be generalized to form similar Fe@SiO_2 and Co@SiO_2 yolk-shell structures (Figure 2.8).

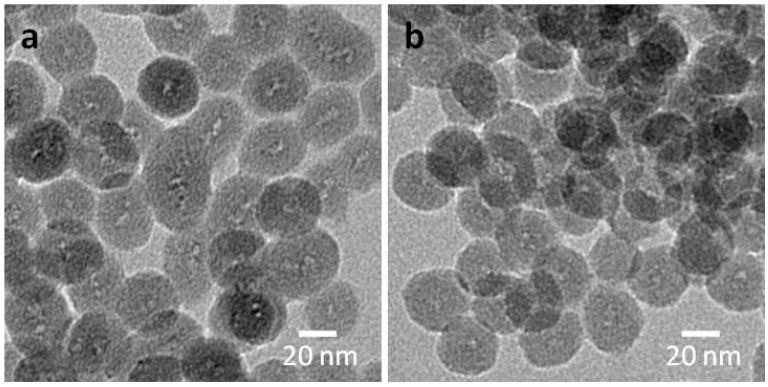

Figure 2.8 TEM images of (a) Fe@SiO_2 and (b) Co@SiO_2 samples after synthesis and drying at ca. 100°C.

The synthesized Ni@SiO_2 nanotubes have porous shells and accessible active Ni surface area, as shown by H_2 chemisorption measurements. N_2 physisorption results are consistent with this conclusion, indicating intraparticle pore sizes on the order of 1 nm. Moreover, simple variation of the amount of silica precursor used during synthesis allows tuning of the shell thickness of Ni@SiO_2 particles in the range of 5.1 to 12.4 nm. Therefore this material may be evaluated for catalytic applications in which the stability, metal-support contact, and size selectivity characteristics of yolk-shell materials are expected to be advantageous.

References

[1] Takenaka, S.; Matsumori, H.; Matsune, H.; Tanabe, E.; Kishida, M. High Durability of Carbon Nanotube-Supported Pt Electrocatalysts Covered with Silica Layers for the Cathode in a PEMFC. *J. Electrochem. Soc.* **2008**, *155*, B929–B936.

[2] Takenaka, S.; Matsumori, H.; Arike, T.; Matsune, H.; Kishida, M. Preparation of carbon nanotube-supported Pt metal particles covered with silica layers and their application to electrocatalysts for PEMFC. *Top. Catal.* **2009**, *52*, 731-738.

[3] Takenaka, S.; Hirata, A.; Tanabe, E.; Matsune, H.; Kishida, M. Preparation of supported Pt-Co alloy nanoparticle catalysts for oxygen reduction reaction by coverage with silica. *J. Catal.* **2010**, *274*, 228-238.

[4] Shimazaki, Y.; Hayasaka, S.; Koyama, T.; Nagao, D.; Kobayashi, Y.; Konno, M. A durable PtRu/C catalyst with a thin protective layer for direct methanol fuel cells. *J. Colloid Interface Sci.* **2010**, *351*, 580-583.

[5] Shimazaki, Y.; Kobayashi, Y.; Sugimasa, M.; Yamada, S.; Itabashi, T.; Miwa, T.; Konno, M. Preparation and characterization of long-lived anode catalyst for direct methanol fuel cells. *J. Colloid Interface Sci.* **2006**, *300*, 253-258.

[6] Matsumori, H.; Takenaka , S.; Matsune, H.; Kishida, M. Preparation of carbon nanotube-supported Pt catalysts covered with silica layers; application to cathode catalysts for PEFC. *Appl. Catal., A* **2010**, *373*, 176-185.

[7] Zhou, C.; Peng, F.; Wang, H.; Yu, H.; Peng, C.; Yang, J. Development of stable PtRu catalyst coated with manganese dioxide for electrocatalytic oxidation of methanol. *Electrochem. Commun.* **2010**, *12*, 1210-1213.

[8] Yeung, C. M. Y.; Tsang, S. C. Some optimization in preparing core-shell Pt-ceria catalysts for water gas shift reaction. *J. Mol. Catal. A: Chem.* **2010**, *322*, 17-25.

[9] Yeung, C. M. Y.; Tsang, S. C. Noble metal core-ceria shell catalysts for water-gas shift reaction. *J. Phys. Chem. C* **2009**, *113*, 6074-6087.

[10] Yeung, C. M. Y.; Meunier, F.; Burch, R.; Thompsett, D.; Tsang, S. C. Comparison of new microemulsion prepared "Pt-in-Ceria" catalyst with conventional "Pt-on-Ceria" catalyst for water-gas shift reaction *J. Phys. Chem. B* **2006**, *110*, 8540-8543.

[11] Yeung, C. M. Y.; Yu, K. M. K.; Fu, Q. J.; Thompsett, D.; Petch, M. I.; Tsang, S. C. Engineering Pt in ceria for a maximum metal−support interaction in catalysis. *J. Am. Chem. Soc.* **2005**, *127*, 18010-18011.

[12] Montini, T.; De Rogatis, L.; Gombac, V.; Fornasiero, P.; Graziani, M. Rh(1%)@$Ce_xZr_{1-x}O_2$–Al_2O_3 nanocomposites: Active and stable catalysts for ethanol steam reforming. *Appl. Catal., B* **2007**, *71*, 125-134.

[13] Takenaka, S.; Orita, Y.; Umebayashi, H.; Matsune, H.; Kishida, M. High resistance to carbon deposition of silica-coated Ni catalysts in propane steam reforming. *Appl. Catal., A* **2008**, *351*, 189-194.

[14] Xu, J.; Yeung, C. M. Y.; Ni, J.; Meunier, F.; Acerbi, N.; Fowles, M.; Tsang, S. C. Methane steam reforming for hydrogen production using low water-ratios without carbon formation over ceria coated Ni catalysts. *Appl. Catal., A* **2008**, *345*, 119-127.

[15] Takenaka, S.; Umebayashi, H.; Tanabe, E.; Matsune, H.; Kishida, M. Specific performance of silica-coated Ni catalysts for the partial oxidation of methane to synthesis gas. *J. Catal.* **2007**, *245*, 392-400.

[16] Xu, S.; Zhao, R.; Wang, X. Highly coking resistant and stable Ni/Al_2O_3 catalysts prepared by W/O microemulsion for partial oxidation of methane. *Fuel Process. Technol.* **2004**, *86*, 123-133.

[17] Montini, T.; Condo, A. M.; Hickey, N.; Lovey, F. C.; De Rogatis, L.; Fornasiero, P.; Graziani, M. Embedded Rh(1 wt.%)@Al_2O_3: Effects of high temperature and prolonged aging under methane partial oxidation conditions. *Appl. Catal., B* **2007**, *73*, 84-97.

[18] Hayashi, H.; Chen, L. Z.; Tago, T.; Kishida, M.; Wakabayashi, K. Catalytic properties of Fe/SiO_2 catalysts prepared using microemulsion for CO hydrogenation. *Appl. Catal., A* **2002**, *231*, 81-89.

[19] Joo, S. H.; Park, J. Y.; Tsung, C. K.; Yamada, Y.; Yang, P.; Somorjai, G. A. Thermally stable Pt/mesoporous silica core–shell nanocatalysts for high-temperature reactions. *Nat. Mater.* **2009**, *8*, 126-131.

[20] Somorjai, G. A.; Rioux, R. M. High technology catalysts towards 100% selectivity: Fabrication, characterization and reaction studies. *Catal. Today* **2005**, *100*, 201-215.

[21] Kim, W. Y.; Hanaoka, T.; Kishida, M.; Wakabayashi, K. Hydrogenation of carbon monoxide over zirconia-supported palladium catalysts prepared using water-in-oil microemulsion. *Appl. Catal., A* **1997**, *155*, 283-289.

[22] Kishida, M.; Umakoshi, K.; Kim, W. Y.; Hanaoka, T.; Nagata, H.; Wakabayashi, K. A Novel Preparation Method of Supported Metal Catalysts Using Microemulsion. *Kagaku Kogaku Ronbunshu* **1995**, *21*, 990-996.

[23] Ikeda, S.; Ishino, S.; Harada, T.; Okamoto, N.; Sakata, T.; Mori, H.; Kuwabata, S.; Torimoto, T.; Matsumura, M. Ligand-free platinum nanoparticles encapsulated in a hollow porous carbon shell as a highly active heterogeneous hydrogenation catalyst. *Angew. Chem. Int. Ed.* **2006**, *45*, 7063-7066.

[24] Maeda, K.; Sakamoto, N.; Ikeda, T.; Ohtsuka, H.; Xiong, A.; Lu, D.; Kanehara, M.; Teraishi, T.; Domen, K. Preparation of core-shell-structured nanoparticles (with a noble-metal or metal oxide core and a chromia shell) and their application in water splitting by means of visible light. *Chem. Eur. J.* **2010**, *16*, 7750-7759.

[25] Cao, A.; Lu, R.; Veser, G. Stabilizing metal nanoparticles for heterogeneous catalysis. *Phys. Chem. Chem. Phys.* **2010**, *12*, 13499-13510.

[26] Gould, B. D.; Chen, X.; Schwank, J. W. Dodecane reforming over nickel-based monolith catalysts: Deactivation and carbon deposition. *Appl. Catal., A* **2008**, *334*, 277-290.

[27] Takenaka, S.; Hori, K.; Matsune, H.; Kishida, M. Control of selectivity based on the diffusion rates of the reactants in the oxidation of mixed hydrocarbons with molecular oxygen over silica-coated Pt catalysts. *Chem. Lett.* **2005**, *34*, 1594-1595.

[28] Hori, K.; Matsune, H.; Takenaka, S.; Kishida, M. Preparation of silica-coated Pt metal nanoparticles using microemulsion and their catalytic performance. *Sci. Technol. Adv. Mater.* **2006**, *7*, 678-684.

[29] Kim, M.; Sohn, K.; Na, H. B.; Hyeon, T. Synthesis of nanorattles composed of gold nanoparticles encapsulated in mesoporous carbon and polymer shells. *Nano Lett.* **2002**, *2*, 1383-1387.

[30] Pan, X.; Fan, Z.; Chen, W.; Ding, Y.; Luo, H.; Bao, X. Enhanced ethanol production inside carbon-nanotube reactors containing catalytic particles. *Nat. Mater.* **2007**, *6*, 507-511.

[31] Chen, W.; Pan, X.; Bao, X. Tuning of redox properties of iron and iron oxides via encapsulation within carbon nanotubes. *J. Am. Chem. Soc.* **2007**, *129*, 7421-7426.

[32] Yu, K.; Wu, Z.; Zhao, Q.; Li, B.; Xie, Y. High-temperature-stable Au@SnO_2 core/shell supported catalyst for CO oxidation. *J. Phys. Chem. C* **2008**, *112*, 2244-2247.

[33] Narkhede, V. S.; De Toni, A.; Narkhede, V. V.; Guraya, M.; Niemantsverdriet, J. W.; van den Berg, M. W. E.; Grünert, W.; Gies, H. Au/TiO_2 catalysts encapsulated in the mesopores of siliceous MCM-48 – Reproducible synthesis, structural characterization and activity for CO oxidation. *Microporous Mesoporous Mater.* **2009**, *118*, 52-60.

[34] Yin, H.; Ma, Z.; Zhu, H.; Chi, M.; Dai, S. Evidence for and mitigation of the encapsulation of gold nanoparticles within silica supports upon high-temperature treatment of Au/SiO_2 catalysts: Implication to catalyst deactivation. *Appl. Catal., A* **2010**, *386*, 147-156.

[35] Liz-Marzán, L. M.; Correa-Duarte, M. A.; Pastoriza-Santos, I.; Mulvaney, P.; Ung, T.; Giersig, M.; Kotov, N. A.; Core-Shell Nanoparticles and Assemblies Thereof. In *Handbook of Surfaces and Interfaces of Materials*; Nalwa, H., Ed.; Academic Press, 2001; Vol. 3; pp 190-238.

[36] Lee, J.; Park, J. C.; Song, H. A nanoreactor framework of a Au@SiO_2 yolk/shell structure for catalytic reduction of p-nitrophenol. *Adv. Mater.* **2008**, *20*, 1523-1528.

[37] Xiao, Q.; Tao, X.; Zou, H.; Chen, J. Comparative study of solid silica nanoparticles and hollow silica nanoparticles for the immobilization of lysozyme. *Chem. Eng. J.* **2008**, *137*, 38–44.

[38] Arnal, P. M.; Comotti, M.; Schüth, F. High-temperature-stable catalysts by hollow sphere encapsulation. *Angew. Chem. Int. Ed.* **2006**, *45*, 8224-8227.

[39] Huang, X.; Guo, C.; Zuo, J.; Zheng, N.; Stucky, G. D. An assembly route to inorganic catalytic nanoreactors containing sub-10-nm gold nanoparticles with anti-aggregation properties. *Small* **2009**, *5*, 361-365.

[40] Yin, Y.; Rioux, R. M.; Erdonmez, C. K.; Hughes, S.; Somorjai, G. A.; Alivisatos, A. P. Formation of hollow nanocrystals through nanoscale Kirkendall effect. *Science* **2004**, *304*, 711-714.

[41] Jafellicci, M.; Davolos, M. R.; Jose dos Santos, F.; Jose de Andrade, S. Hollow silica particles from microemulsion. *J. Non-Cryst. Solids* **1999**, *247*, 98-102.

[42] Jang, J.; Yoon, H. Novel fabrication of size-tunable silica nanotubes using a reverse-microemulsion-mediated sol-gel method. *Adv. Mater.* **2004**, *16*, 799-802.

[43] Liu, J.; Yang, H. Q.; Kleitz, F.; Chen, Z. G.; Yang, T.; Strounina, E.; Lu, G. Q.; Qiao, S. Z. Yolk-shell hybrid materials with a periodic mesoporous organosilica shell: Ideal nanoreactors for selective alcohol oxidation. Adv. Funct. Mater. **2012**, *22*, 591-599.

[44] Whaley, L.; Veser, G. Highly reactive and robust Ni@SiO_2 core-shell catalysts for catalytic partial oxidation of methane. Paper 4848 Extended Abstract, 22nd North American Catalysis Society Meeting, Detroit, MI , June 5-10, 2011. http://nam.confex.com/nam/2011/webprogram/Paper4848.html

[45] Boutonnet, M.; Kizling, J.; Stenius, P.; Maire, G. The preparation of monodisperse colloidal metal particles from microemulsions. *Colloids Surf.* **1982**, *5*, 209-225.

[46] Chen, D.H.; Wu, S.H. Synthesis of Nickel Nanoparticles in Water-in-Oil Microemulsions. *Chem. Mater.* **2000**, *12*, 1354-1360.

[47] Ojeda, M.; Rojas, S.; Boutonnet, M.; Pérez-Alonso, F.J.; Garcia-Garcia, F.; Fierro, J.L.G. Synthesis of Rh nano-particles by the microemulsion technology - Particle size effect on the CO+H_2 reaction. *Appl. Catal., A* **2004**, *274*, 33-41.

[48] Trepanier, M.; Dalai, A.K.; Abatzoglou, N. Synthesis of CNT-supported cobalt nanoparticle catalysts using a microemulsion technique: Role of nanoparticle size on

reducibility, activity, and selectivity in Fischer-Tropsch reactions. *Appl. Catal., A* **2010**, *374*, 79-86.

[49] Pramanik, S.; Bhattacharya, S.C. Size tunable synthesis and characterization of cerium tungstate nanoparticles via H_2O/AOT/heptane microemulsion. *Mater. Chem. Phys.* **2010**, *121*, 125-130.

[50] Lopez-Quintela, M. A. Synthesis of nanomaterials in microemulsions: Formation mechanisms and growth control. *Curr. Opin. Colloid Interface Sci.* **2003**, *8*, 137-144.

[51] Chang, C.-L.; Fogler, H.S. Controlled formation of silica particles from tetraethyl orthosilicate in nonionic water-in-oil microemulsions. *Langmuir* **1997**, *13*, 3295-3307.

[52] Moulik, S. P.; Paul, B. K. Structure, Dynamics and Transport Properties of Microemulsions. *Adv. Colloid Interface Sci.* **1998**, *78*, 99-195.

[53] Shinoda, K.; Saito, H. The effect of temperature on the phase equilibria and the types of dispersions of the ternary system composed of water, cyclohexane, and nonionic surfactant. *J. Colloid Interface Sci.* **1968**, *26*, 70-74.

[54] Lo, A.; Florence, A.T.; Treguier, J.-P.; Seiller, M.; Puisieux, F. The influence of surfactant HLB and the nature of the oil phase diagrams of nonionic surfactant-oil-water systems. *J. Colloid Interface Sci.* **1977**, *59*, 319-327.

[55] Herrmann, C.-U.; Klar, G.; Kahlweit, M. On the phase inversion in H_2O-oil-nonionic surfactant systems and related phenomena. *J. Colloid Interface Sci.* **1981**, *82*, 6-13.

[56] Lindman, B. Phase Behaviour, Interfacial Tension and Microstructure of Microemulsions. In Microemulsions: Background, New Concepts, Applications, Perspectives, ed. Stubenrauch, C. Wiley 2009.

[57] Burauer, S.; Sachert, T.; Sottmann, T.; Strey, R. On microemulsion phase behavior and the monomeric solubility of surfactant. *Phys. Chem. Chem. Phys.* **1999**, *1*, 4299-4306.

[58] Boutonnet, M,; Lögdberg, S.; Svensson, E.E. Recent developments in the application of nanoparticles prepared from w/o microemulsions in heterogeneous catalysis. *Curr. Opin. Colloid Interface Sci.* **2008**, *13*, 270-286.

[59] Hanaoka, T.; Hatsuta, T.; Tago, T.; Kishida, M.; Wakabayashi, K. Control of the rhodium particle size of the silica-supported catalysts by using microemulsion. *Appl. Catal., A* **2000**, *190*, 291-296.

[60] Capek, I. Preparation of metal nanoparticles in water-in-oil (w/o) microemulsions. *Adv. Colloid Interface Sci.* **2004**, *110*, 49-74.

[61] Destree, C.; Nagy, J.B. Mechanism of formation of inorganic and organic nanoparticles from microemulsions. *Adv. Colloid Interface Sci.* **2006**, *123-126*, 353-367.

[62] Hanaoka, T.; Hayashi, H.; Tago, T.; Kishida, M.; Wakabayashi, K. In situ immobilization of ultrafine particles synthesized in a water/oil microemulsion. *J. Colloid Interface Sci.* **2001**, *235*, 235-240.

[63] Kishida, M.; Hanaoka, T.; Kim, W.Y.; Nagata, H.; Tago, T.; Wakabayashi, K. Size control of rhodium particle of silica-supported catalysts using water-in-oil microemulsion. *Appl. Surf. Sci.* **1997**, *121-122*, 347-350.

[64] Martínez, A.; Prieto, G. The key role of support-surface tuning during the preparation of catalysts from reverse micellar-synthesized metal nanoparticles. *Catal. Commun.* **2007**, *8*, 1479-1486.

[65] Herranz, T.; Rojas, S.; Perez-Alonso, F.J.; Ojeda, M.; Terreros, P.; Fierro, J.L.G. Carbon oxide hydrogenation over silica-supported iron-based catalysts. *Appl. Catal., A* **2006**, *308*, 19-30.

[66] Martínez, A.; Prieto, G. A surfactant-assisted hydrothermal deposition method for preparing highly dispersed W/γ-Al_2O_3 hydrodenitrogenation catalyst. *J. Catal.* **2007**, *245*, 470-476.

[67] Dauscher, A.; Touroude, R.; Maire, G.; Kizling, J.; Boutonnet-Kizling, M. Influence of the preparation mode on metal-support interactions in Pt/TiO_2 catalysts. *J. Catal.* **1993**, *143*, 155-165.

[68] Heitsch, A.T.; Smith, D.K.; Patel, R.E.; Ress, D.; Korgel, B.A. Multifunctional particles: magnetic nanocrystals and gold nanorods coated with fluorescent dye-doped silica shells. *J. Solid State Chem.* **2008**, *181*, 1590-1599.

[69] Yi, D.; Lee, S.; Papaefthymiou, G.; Ying, J. Nanoparticle architectures template by SiO_2/Fe_2O_3 nanocomposites. *Chem. Mater.* **2006**, *18*, 614-619.

[70] Kishida, M.; Tago, T.; Hatsuta, T.; Wakabayashi, K. Preparation of silica-coated rhodium nanoparticles using water-in-oil microemulsion. *Chem. Lett.* **2000**, *29*, 1108-1109.

[71] Li, Z.; Han, C.; Shen, J. Reduction of Ni^{2+} by hydrazine in solution for the preparation of nickel nano-particles. *J. Mater. Sci.* **2006**, *41*, 3473-3480.

[72] Yao, L.; Xu, G.; Dou, W.; Bai, Y. The control of size and morphology of nanosized silica in Triton X-100 based reverse micelle. *Colloids Surf., A* **2008**, *316*, 8-14.

[73] Tornblom, M.; Henriksson, U. Effect of solubilization of aliphatic hydrocarbons on size and shape of rodlike C_{16}TABr micelles studied by ^{2}H NMR relaxation. *J. Phys. Chem. B* **1997**, *101*, 6028-6035.

[74] D'Arrigo, J. S. Concentrated gas-in-liquid emulsions in artificial media. II. Characterization by photon correlation spectroscopy. *Studies in Interface Science* **2011**, *25*, 135-168.

[75] Zhang, J.; Ge, Z.; Jiang, X.; Hassan, P. A.; Liu, S. Stopped-flow kinetic studies of sphere-to-rod transitions of sodium alkyl sulfate micelles induced by hydrotropic salt. *J. Colloid Interface Sci.* **2007**, *316*, 796-802.

[76] Shrestha, L. K.; Shrestha, R. G.; Varade, D.; Aramaki, K. Tunable parameters for the structural control of reverse-micelles in glycerol monoisostearate/oil systems: A SAXS study. *Langmuir* **2009**, *25*, 4435-4442.

[77] Strestha, L. K.; Sato, T.; Acharya, D. P.; Iwanaga, T.; Aramaki, K.; Kunieda, H. Phase behavior of monoglycerol fatty acid esters in nonpolar oils: Reverse rodlike micelles at elevated temperatures. *J. Phys. Chem. B* **2006**, *110*, 12266-12273.

[78] Teng, F.; Tian, Z.; Xu, J.; Xiong, G.; Lin, L. Synthesis of nano-sized $BaAl_{12}O_{19}$ via nonionic reverse microemulsion method: I. Effect of the microemulsion structure on the paticle morphology. *Stud. Surf. Sci. Catal.* **2004**, *147*, 493-498.

[79] Capek, I. Preparation of metal nanoparticles in water-in-oil (w/o) microemulsions. *Adv. Colloid Interface Sci.* **2004**, *110*, 49-74.

[80] Stubenrauch, C.; Wielpütz, T.; Sottmann, T.; Roychowdhury, C.; DiSalvo, F. J. Microemulsions as Templates for the Synthesis of Metallic Nanoparticles. *Colloids Surf., A* **2008**, *317*, 328-338.

Chapter 3

Catalytic performance of Ni@SiO_2 nanospheres and nanotube materials for autothermal reforming of propane

Introduction

Fuel cells are a critical part of today's developing portfolio of energy technologies. These devices convert chemical energy directly to electrical energy without intermediary heat generation or mechanical work steps. For this reason their efficiencies are not limited by Carnot thermodynamics, which currently contribute to a loss of approximately 66% of the energy consumed in transportation and electricity generation [1]. Solid oxide fuel cells (SOFCs) are especially attractive for their high efficiencies (50-60%) and strong performance in the presence of CO and hydrocarbons, typically harmful to other types of fuel cells.

One promising application of SOFCs is in onboard auxiliary power units (APUs). Such devices could greatly increase fuel efficiency and reduce emissions in vehicles that spend significant amounts of time idling [2]. These devices utilize commercially available fuels, such as gasoline, diesel, or JP-8, with higher efficiency. Therein lies a key advantage, as the use of portable liquid fuels overcomes the problems of establishing a hydrogen economy. A critical component of the APU is the catalytic fuel reformer, in which autothermal reforming (ATR), a combination of

exothermic partial oxidation (POX) and endothermic steam reforming (SR), converts a hydrocarbon feedstock into syngas (i.e., H_2 and CO). The syngas is in turn fed to the SOFC for conversion to electrical power. Though they are effective fuel reforming catalysts, Pt-group metals are costly and lose preference to inexpensive catalyst materials such as Ni. However, Ni-based catalysts suffer from several forms of deactivation that limit their long-term performance, including particle growth and carbon deposition. Particle growth may even indirectly cause carbon deposition, as shown by studies in which carbon deposition is less extensive for smaller Ni particles [3].

Since core@shell catalytic nanostructures lead to improved metal nanoparticle stability and size-selectivity characteristics [4,5], they may be ideal for fuel reforming applications. Ni@SiO_2 catalysts should be resistant to particle growth and the associated process of carbon deposition. Moreover, because the selectivity of fuel reforming is limited during operation by equilibrium, the diffusion barrier imposed by the SiO_2 shell in Ni@SiO_2 particles could cause them to act as membrane nanoreactors, enhancing overall selectivity. Molecular H_2, formed by steam reforming and water-gas shift on the encapsulated Ni metal surface, is expected to diffuse much faster through the porous SiO_2 shell than other products and therefore be selectively removed from the gas phase in contact with the catalytically active surface. This would cause the steam reforming and water-gas shift reactions to continue to form more products (i.e., more H_2) to achieve equilibrium.

Several sources have reported syntheses for core@shell catalyst materials that contain cavities in which metal nanoparticles are dispersed, known as yolk-shell materials, where the “egg white” is a cavity [6,7,8,9,10,11,12,13]. In Chapter 2, the novel synthesis of Ni@SiO_2 nanotubes from a microemulsion template was demonstrated [14]. These materials have porous SiO_2 shells (pores on the order of 1 nm), tunable shell thickness (5.1 to 12.4 nm), and controllable yolk-shell nanotube vs. core@shell nanosphere morphology. In the case of yolk-shell catalysts, the desirable core@shell structure characteristics may be retained while additional desirable effects are potentially produced, such as decreased extent of blocking of the metal surface by

the support and further enhanced selectivity due to further accumulation of larger-size reaction intermediates in the gas phase in contact with the metal surface. To date, no direct comparison of the catalytic performance of core@shell and yolk-shell has been reported.

Ni@SiO_2 nanospheres have previously been reported to be more active and stable than conventional, impregnated Ni-based catalysts for methane partial oxidation [15,16] and propane steam reforming [17]. In methane partial oxidation at 700°C, Takenaka *et al*. found that coated Ni@SiO_2 catalysts maintained about 70% methane conversion over 3 hr on stream, while a conventional supported Ni catalyst had much lower initial conversion which decreased to less than 5% after 30 minutes [15]. At 800°C, they found that a Ni@SiO_2 catalyst maintained CH_4 conversion and CO selectivity at levels higher than 90% for 10 hr on stream, without any sign of deactivation. The group used XANES and TPR analyses to conclude that Ni interacted strongly with SiO_2 in Ni@SiO_2, which prevented particle growth and oxidation, though carbon deposition and changes in particle size were not measured. The same group found in propane steam reforming experiments that a Ni@SiO_2 catalyst had a higher propane conversion and H_2 selectivity over 5 hr on stream than impregnated Ni/MgO and Ni/Al_2O_3 catalysts [17]. Similar XANES analyses showed a stronger interaction between metal and support in Ni@SiO_2 than in Ni/MgO and Ni/Al_2O_3, which the authors again concluded to be the basis of the higher stability and activity of Ni@SiO_2. Carbon deposition measurements showed that carbon deposition on Ni@SiO_2 was less than on impregnated samples.

Li *et al*. found similar results for their methane partial oxidation experiments at 750°C on a Ni@SiO_2 catalyst, where CH_4 conversion and H_2 selectivity were maintained over 90% for 9 hr on stream [16]. An impregnated Ni/SiO_2 catalyst under the same conditions initially had a lower conversion and selectivity, and deactivating continuously during the experiment. TPO experiments following selected reactions showed that some carbon deposition occurred on Ni@SiO_2, although carbon deposition was not measured on an impregnated Ni/SiO_2 sample for comparison.

There is strong consensus within the above literature that Ni@SiO_2 nanospheres are more active and stable than impregnated Ni catalysts due to their resistance to particle growth and carbon deposition, though the extents of these conventional deactivation effects have not been quantified consistently. Moreover, core@shell catalysts must retain shell porosity and dispersion over time, or the catalytically active material may become inaccessible to reactants; however post-reaction TEM analyses of Ni@SiO_2 have not been reported, and the morphological stability of these materials in ATR environments is completely unknown. Finally, the size selectivity characteristics of Ni@SiO_2 has not been recognized, even though there should be a significant effect on the equilibrium-limited ATR reaction selectivity.

In this chapter, to address the above shortcomings in the Ni@SiO_2 reforming literature, and to compare the catalytic performances of yolk-shell and solid sphere core@shell morphologies, the novel Ni@SiO_2 nanotubes were evaluated along with Ni@SiO_2 nanospheres and conventional impregnated Ni/SiO_2 materials for ATR of propane over 20 hr on stream. Many studies have shown that liquid hydrocarbons fed to a reforming catalyst are rapidly and completely converted by homogeneous oxidation and cracking reactions at the catalyst entrance to light olefins (primarily ethylene and propylene), methane, and reforming products (i.e., CO, CO_2, and H_2) [18,19,20,21,22,23,24]. Light olefins, especially ethylene, are also known to be the principle precursors of carbon deposition [23]. Therefore catalysts that are effective and durable for light olefin reforming will also be effective and durable for liquid hydrocarbon reforming. Hence propane, which is expected to be converted to ethylene, methane, and reforming products, is an appropriate study hydrocarbon for reforming experiments representing other fuels.

During reaction experiments, the concentrations of each product species were monitored carefully to investigate selectivity differences between the catalyst morphologies. Following propane ATR tests, samples were analyzed by TGA and TEM to observe and quantify carbon deposition, metal particle growth, and morphological changes.

Background of fuel reforming and carbon deposition

The traditional reforming reactions of steam reforming (SR) and partial oxidations (POX) are well-established. SR was first demonstrated by Standard Oil in 1930, and POX was first developed in 1945 by Texaco and Shell [25]. The POX and SR reaction equations are accompanied by the water-gas shift reaction, and all three reactions are shown below:

Steam reforming: $$C_xH_y + xH_2O \leftrightarrow xCO + \left(x + \frac{y}{2}\right)H_2$$

Partial oxidation: $$C_xH_y + \frac{x}{2}O_2 \rightarrow xCO + \frac{y}{2}H_2$$

Water-gas shift: $$CO + H_2O \leftrightarrow CO_2 + H_2$$

SR is reversible with a reaction enthalpy for *n*-paraffins with *x* carbon atoms $\Delta H^\circ \approx 157.3x$ kJ/mol. POX is irreversible with $\Delta H^\circ \approx -86.4x$ kJ/mol. Autothermal reforming (ATR) couples these two reactions in the same catalyst bed so that exothermic POX drives endothermic SR.

Reforming of light hydrocarbons, especially methane, is well researched, whereas reforming of liquid hydrocarbons has been investigated only more recently. Examples of these hydrocarbons are tetralin, isooctane, decane, dodecane, tetradecane, and hexadecane [18,26,27,28,29]. Some work has also been done with fuels that approximate real JP-8 [19,20,30].

Some work, though largely speculative, has been done to illuminate reaction pathways for heavier hydrocarbons. Gould *et al*. studied dodecane ATR on Ni/CZO experimentally and reported that dodecane is converted by a combination of oxidative cracking on CZO, catalytic cracking, and homogenous pyrolysis to H_2, CO_x, and C_1-C_4 hydrocarbons. These lighter hydrocarbons are then the primary reactants for SR [27]. Dorazio *et al*. used computational modeling to study tetradecane ATR and reported that 50% of the tetradecane was converted by POX to H_2 and CO_2, and the other 50% was cracked to light hydrocarbons (C_2H_4 and CH_4), H_2,

and CO_2. No SR but significant water-gas shift activities were observed [26]. The mechanism for methane reforming, however, is comparatively well understood. Wei *et al*. studied methane SR on Ni/MgO and found that C-H bond activation was the rate-limiting step [31]. Nikolla *et al*. found similar results for methane reforming on Ni/YSZ and Sn-Ni/YSZ catalysts [32].

ATR studies have distinguished two distinct reaction zones in series in the catalyst bed: a high-temperature oxidation zone and an oxygen-depleted reforming zone with decreasing temperature. Horn *et al*. studied methane POX on Rh and Pt catalysts and found a short oxidation region where O_2 was consumed and temperature increased, followed by a longer reforming zone which used H_2O formed in the oxidation zone [21]. Hotz *et al*. studied butane reforming in a $Rh/Ce_{0.5}Zr_{0.5}O_2$ radial microreactor and observed the reaction in 3 segments along the reaction coordinate. In the first segment, all O_2 and most butane were converted and most H_2 and CO were produced. In segments 2 and 3, the temperature decreased while H_2O and CO_2 reforming produced more H_2 and CO [22].

Particularly important in the ATR reaction pathway are light olefins, ethylene and propylene. The homogeneous production of such olefins in the catalyst entrance zone is one major conversion pathway for heavy hydrocarbons [23]. The importance of this gas-phase chemistry was demonstrated by Randolph *et al*., who saw that hexane was completely converted at 800˚C and a space time of 100 ms to 70 mol% methane, ethylene, and propylene [24]. In catalytic studies of heavy hydrocarbon ATR, several groups have found that the most prevalent reaction products besides H_2, CO_x, and methane were ethylene and propylene, reiterating their homogenously formation at the reactor entrance [18,19,20].

The reactivities of these lighter olefins is unclear, however these species have been reported to be precursors for carbon deposition, among which ethylene is the foremost [3,19,20,23,33]. Some work has been done to investigate the reactivities of light hydrocarbons with a number of catalysts. In most cases the primary products of ethane, ethylene, propane, and propylene SR were H_2 and CO with varying levels of methane, as predicted by equilibrium [34,35,36,37].

However, SR of propane on Pd was selective to mostly propylene or ethylene [35]. Ethylene was also formed in homogeneous experiments with mixtures of ethane and propane [34]. It may be that olefins are intermediates in reforming of paraffins. Also, methane formed in these experiments, especially at levels exceeding equilibrium, is believed to be formed by hydrogenolysis on Rh and Ni [37].

Some work has specifically looked at carbon formation of light hydrocarbons. Graf *et al*. found that Rh/YSZ deactivated faster for ethylene SR than for ethane [37]. Yoon *et al*. singled out ethylene as a carbon precursor and looked at ethylene ATR, SR, and POX on Pt/GDC. POX and ATR both led to less carbon deposition than SR, but if ethylene is formed in the reactor entrance where O_2 is quickly consumed, then it is effectively exposed to SR conditions in the catalyst bed [19].

The tendency of Ni-based catalysts to form carbon that causes deactivation is well known [3,38,39,40,41,42,43,44]. Three types of carbon deposition are observed in reforming reactions: pyrolytic, coating, and filamentous [39,40]. Filamentous carbon is the most deleterious and grows as graphene fibers or nanotubes between Ni particles and the support, eventually separating the two completely. Excessive carbon fiber or nanotube growth can lead to mechanical stress causing severe catalyst attrition [3].

Filamentous carbon formation starts with the decomposition of carbon-containing species on the catalyst surface. Carbon formed on the surface diffuses into the Ni bulk to low-coordinated or defect sites on the support-side of the Ni particle, where graphene phases can nucleate and propagate [40,44]. The location of carbon deposition in the catalyst bed can depend on the presence of oxygen and water, and the support properties, but in general deposition increases in downstream sections where temperature is decreased and oxidant is depleted [41].

Carbon deposition can be reduced by increasing the O/C and H_2O/C ratios, and the temperature in the catalyst bed with supplementary heat [3,36]. However, the carbon tolerance of the

catalyst itself can be improved. Since the defect sites that nucleate carbon phases are more prevalent on larger particle, smaller Ni particles form carbon much more slowly [3,39,40], and particles smaller than 7 nm appear not to form carbon at all [3]. It has been shown that these defect sites can be deactivated by alloying with Sn, S, Au, and K, which greatly reduces carbon-related deactivation [40,42,43,44]. However a core@shell nanostructure may stabilize small Ni particles under reforming conditions, and may completely remove the possibility of carbon deposition.

Experimental

Conventional, impregnated 5 wt% Ni/SiO_2 was synthesized using a typical incipient wetness impregnation technique. 10 g 40-60 mesh SiO_2 gel was placed in a 100 mL beaker. An appropriate amount of 3.5 M aqueous $Ni(NO_3)_2$ solution was added with additional deionized water to reach incipient wetness. The powder was stirred with a spatula to assure the liquid phase was uniform. The impregnated SiO_2 was then dried overnight at 120°C, calcined at 500°C for 2 hr, and finally reduced in flowing H_2 at 700°C for 2 hr.

The $Ni@SiO_2$ nanospheres and nanotubes were prepared by methods reported in the previous chapter. Both $Ni@SiO_2$ morphologies were synthesized in a water-in-oil microemulsion composed of cylcohexane and polyoxyethylene (10) cetyl ether, at a final water-to-surfactant mole ratio of 23 and a temperature of 50°C. $Ni(NO_3)_2$ was solubilized in the microemulsion, followed by additions of N_2H_4, NH_3, and finally tetraethyl orthosilicate (TEOS). The different nanosphere and nanotube morphologies were achieved by varying the aging time prior to TEOS addition and the N_2H_4/Ni ratio. $N_2H_4/Ni = 12$ and 5 min aging before TEOS addition was used for $Ni@SiO_2$ nanospheres, whereas $N_2H_4/Ni = 45$ and 3.0 hr aging before TEOS addition was used for $Ni@SiO_2$ nanotubes. After allowing 2 hr for conversion of TEOS to SiO_2, the nanoparticles were separated via centrifugation, washed with isopropanol, dried at 100°C overnight, calcined

at 500°C for 2 hr in air, and reduced at 700°C for 2 hr in flowing H_2. Elemental analysis with ICP showed that both Ni@SiO_2 samples had an approximately 2.8 wt% Ni loading.

Samples of impregnated Ni/SiO_2, Ni@SiO_2 nanospheres, and Ni@SiO_2 nanotubes were ground fine in a mortar and pestle and combined 1:4 by weight with 60-80 mesh SiO_2 gel in a 10 mL sample vial with 5 mL of deionized water. The vial was then ultrasonicated for 1 hr and dried overnight at 100°C. For each propane autothermal reforming experiment, 0.9 g of diluted catalyst was loaded into a 0.5 in quartz reactor tube. The catalyst powder was held between two quartz wool plugs, and a thermocouple was inserted upstream of the bed to monitor temperature inside the reactor. Before each experiment, an in-situ reduction step was performed with flowing H_2 at 700°C for 1 hr, followed by a purge step with flowing Ar at 700°C for 1 hr. To initiate the reaction, H_2O was turned on, C_3H_8 was turned on, and then Ar was replaced by air to obtain a reactant stream with O/C = 0.5, H_2O/C = 1.0, and 200 sccm flow rate. The product stream was monitored by a gas chromatograph which sampled every 30 min. Using N_2 as an inert internal standard, the concentrations of H_2, O_2, CO, CO_2, C_3H_8, C_2H_4, and CH_4 were calculated. The reaction was continued for 20 hr and then quenched by replacing air with Ar, then C_3H_8 was turned off, then H_2O was turned off, and finally the reactor was cooled to room temperature.

Following reaction experiments, each catalyst sample was analyzed by TEM and TGA to investigate the extents of carbon deposition, particle growth, and morphological changes. TEM analysis was performed with a JEOL 3011 HRTEM instrument with 300kV accelerating voltage from a LaB_6 thermoelectric emission gun. Specimens were prepared according to the procedure described in the previous chapter. TGA analysis was performed on 40 mg speciments with a TA ThermoGravimetric Analysis instrument. Each specimen was treated at 120°C for 1 hr in a flow of 100 sccm 12% O_2 with N_2 balance, and then under this gas flow the temperature was increased at 10°C/min to 800°C.

Results and Discussion

To evaluate and compare the catalytic performance of Ni@SiO_2 nanotubes, Ni@SiO_2 nanospheres, and conventional, impregnated Ni/SiO_2, these samples were tested in propane autothermal reforming (ATR) experiments. An experiment with a sample of unloaded SiO_2 was used to observe the effects of homogeneous, non-catalytic reactions. For this blank experiment, no C_3H_8 or O_2 were observed leaving the reactor, but only CH_4, C_2H_4, CO, CO_2, and H_2. Moreover, all three catalyst samples had similar concentrations of CH_4 leaving the reactor during experiments compared to the blank experiment. Therefore, the catalytic experiments were effectively tests of the performance of catalysts for C_2H_4 steam reforming and the water-gas shift reaction. This is consistent with the wide agreement in the literature that hydrocarbons are rapidly and completely converted to olefins, methane, and reforming products at the catalyst entrance zone in ATR reactors [18,19,20,21,22,23,24]. The results of propane ATR experiments for the three catalyst samples are shown in Figure 3.1, and TEM images of Ni@SiO_2 nanospheres and nanotubes before ATR experiments are shown in Figure 3.2(a) and (d), respectively.

Impregnated Ni/SiO_2 deactivated over time, evidenced by the decreasing concentration of H_2 and increasing concentration of ethylene leaving the reactor during the experiment. The Ni@SiO_2 nanotube and nanosphere samples, on the other hand, had similar behaviors, with no deactivation observed over 20 hr on stream. At the end of each experiment, both Ni@SiO_2 catalysts had no observed C_2H_4 leaving the reactor, but higher concentrations of H_2 and CO_2 and lower concentrations of CO compared to impregnated Ni/SiO_2, showing their superior activity and stability for ethylene steam reforming and the water-gas shift reaction.

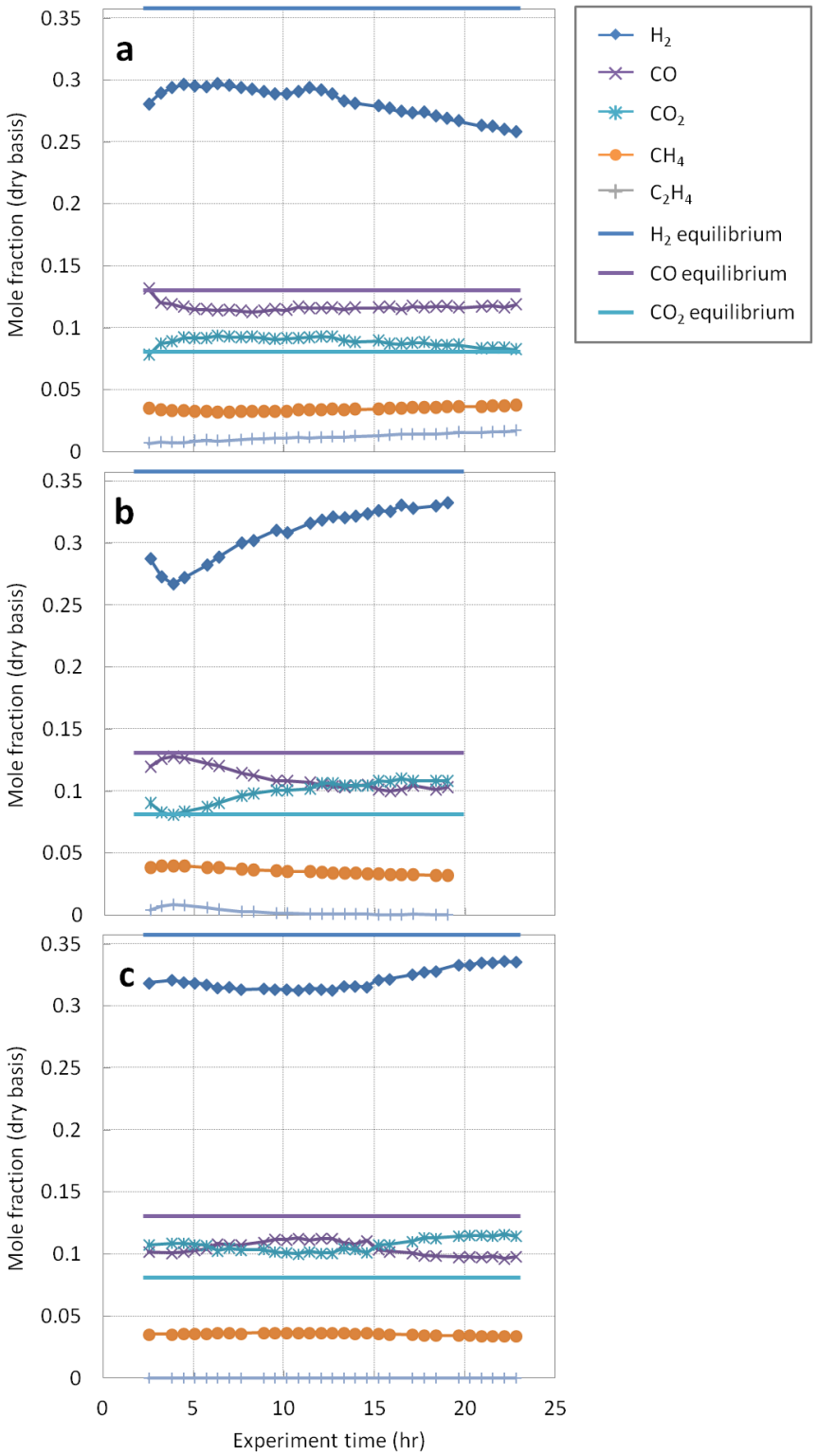

Figure 3.1 Composition (dry basis) of gas stream leaving the reactor during propane ATR experiments for (a) impregnated 5% Ni/SiO_2, (b) 2.8% $Ni@SiO_2$ nanospheres, and (c) 2.8% $Ni@SiO_2$ nanotubes.

The high water-gas shift activity of Ni@SiO_2 catalysts may be related to the SiO_2 shell which acts as a diffusion barrier for products leaving the gas phase in contact with the catalytic active sites. Perhaps H_2 was selectively removed from this phase by rapid diffusion through the SiO_2 shell due to its small molecular size, thereby shifting the water-gas shift equilibrium towards products. Compared to previous results reported for propane steam reforming on Ni@SiO_2 nanospheres by Takenaka *et al*. [17], Ni@SiO_2 catalysts in this study achieved a slightly smaller H_2 yield (0.53 in this work compared to 0.60 in Takenaka *et al*.), which can be expected with the addition of O_2 in an ATR system. But Ni@SiO_2 catalysts in this study had better stability, maintaining steady propane conversion and H_2 yield over 20 hr on stream compared to Takenaka *et al*., who observed decreasing propane conversion over 5 hr on stream, their maximum experiment duration.

To investigate the causes of deactivation of impregnated Ni/SiO_2, and the reasons for the better performance of Ni@SiO_2 samples, catalyst samples were analyzed by TEM following reaction experiments to observe particle growth, carbon deposition, and morphological changes. TEM images of the impregnated Ni/SiO_2 sample showed that filamentous carbon in the form of nanotubes was deposited everywhere Ni particles were observed (Figure 3.2(g) and (h)). Consistent with previous studies, large Ni particles were observed at the ends of carbon nanotubes, separated from the SiO_2 support [3]. These images clearly show a large extent of particle growth and carbon deposition.

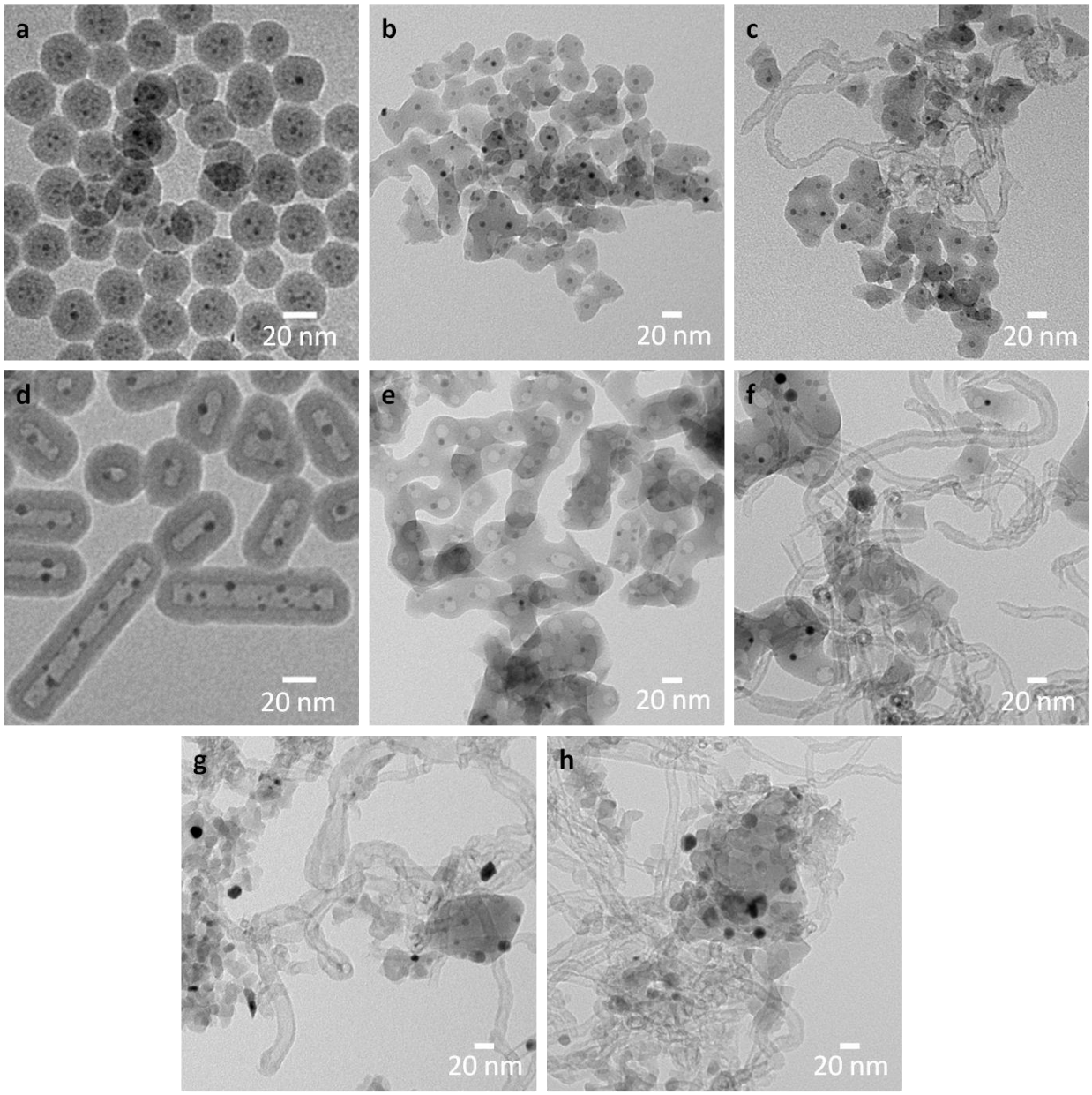

Figure 3.2 Bright field TEM images of catalyst samples before and after propane ATR experiments. Ni@SiO_2 nanospheres (a) before ATR, (b) after ATR in a region without carbon deposition, and (c) after ATR in a region with carbon deposition. Ni@SiO_2 nanotubes (d) before ATR, (e) after ATR in a region without carbon deposition, and (f) after ATR in a region with carbon deposition. (g,h) Impregnated Ni/SiO_2 after ATR.

Images of Ni@SiO_2 nanosphere and nanotube samples following reaction experiments showed some regions with filamentous carbon deposition in the form of nanotubes (Figure 3.2(c) and (f), respectively), but also many other regions with no visible carbon deposition (Figure 3.2(b) and (e), respectively). HRTEM images of carbon nanotubes showed the characteristic carbon layer spacing of approximately 0.35 nm. Both samples also showed some particle growth, but

not as extensively as with impregnated Ni/SiO_2 due to their encapsulation inside SiO_2 shells. The largest change that occurred with Ni@SiO_2 catalyst samples during reaction experiments was sintering or necking of the SiO_2 shells. With the Ni@SiO_2 nanotube, this sintering caused a large decrease in the internal cavity volume of particles, so that over time the morphologies of nanotubes and nanospheres approached a similar morphology. This SiO_2 shell sintering is concerning as it could cause increased shell thickness or a collapse of nanopores, either of which could remove accessible active surface area of encapsulated Ni nanoparticles. However, neither effect occurred extensively enough to be observed as deactivation during reaction experiments. The most significant deactivation effects were particle growth and carbon deposition, which were both mitigated by both Ni@SiO_2 nanospheres and nanotubes.

To quantify the extent of carbon deposition, catalyst samples were analyzed by TGA following reaction experiments. All three samples showed a negative weight change near 600°C (Figure 3.3(a)), characteristic of removal of filamentous carbon [45]. However the amount of carbon deposited during reaction experiments varied between the samples as follows: impregnated Ni/SiO_2 deposited the most carbon (1.9 g C/g Ni), followed by Ni@SiO_2 nanotubes (1.2 g C/g Ni), and then Ni@SiO_2 nanospheres which deposited relatively little carbon (0.25 g C/g Ni). The extent of carbon deposition from reforming reactions is known to increase with increasing Ni particle size [3], and so the higher extent of carbon deposition on Ni@SiO_2 nanotubes compared to Ni@SiO_2 nanospheres suggests that Ni particle growth occurred more in the former, perhaps due to the open cavity space. Following propane steam reforming for 5 hr, Takenaka *et al*. found approximately 0.75 g C/g Ni deposited on a Ni@SiO_2 nanospheres sample and approximately 2.5 g C/g Ni deposited on impregnated Ni/MgO and Ni/Al_2O_3 samples [17]. These carbon deposition amounts for steam reforming are comparable to the results for ATR of this work, given the typically higher extent of carbon deposition which occurs with steam reforming compared to ATR, primarily due to the typically lower operating temperature and lower oxygen availability with the former [3].

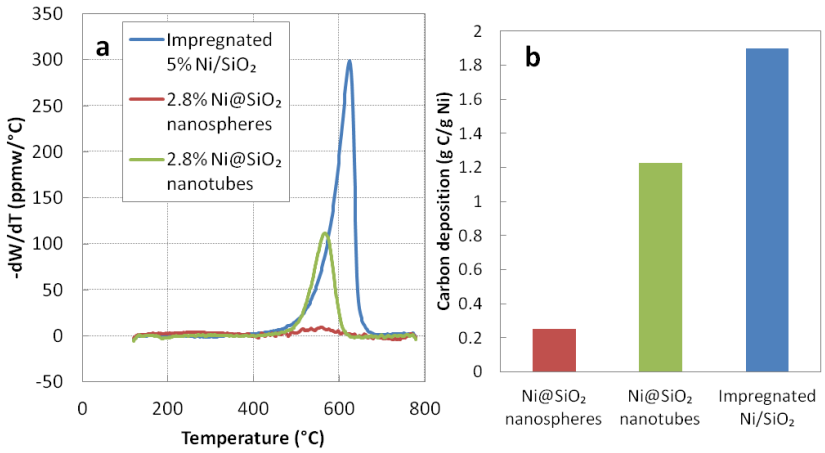

Figure 3.3 TGA TPO analyses of carbon deposition on catalyst samples during propane ATR experiments. (a) Differential weight-change curves and (b) total carbon deposited.

Conclusion

$Ni@SiO_2$ nanotubes are viable and advantageous catalysts, as demonstrated in propane autothermal reforming (ATR) experiments. They had a high selectivity to H_2 and high stability compared to a conventional, impregnated Ni/SiO_2 catalyst, owing to their resistance to Ni particle growth and carbon deposition. However, $Ni@SiO_2$ catalysts experienced SiO_2 shell sintering which caused $Ni@SiO_2$ nanotubes and nanospheres to approach the same morphology over time under ATR conditions. While this did not result in any observed deactivation, the long-term effect on performance is a concern, and $Ni@SiO_2$ materials may be better suited for lower temperature catalytic applications. Additionally, more stable shell materials like Al_2O_3 or ZrO_2 could be utilized to improve the high-temperature performance of Ni core@shell catalysts.

The higher observed H_2 selectivities of $Ni@SiO_2$ catalysts were related to higher activities for ethylene steam reforming and the water-gas shift reaction, and the properties of $Ni@SiO_2$ leading to these higher activities should be further investigated. This suggests that H_2 was selectively removed from the gas phase in contact with the Ni surface by rapid diffusion through the SiO_2 shell, owing to its small molecular size, thereby causing the water-gas shift

reaction to continue to produce H_2 to achieve equilibrium. Future work should investigate if this desirable size selectivity effect can be enhanced by maintaining the cavity spaces in Ni@SiO_2 nanotubes under reaction conditions (with the potential for accumulating reaction intermediates), perhaps by replacing SiO_2 with Al_2O_3 or ZrO_2; and by increasing the shell thickness according to the methods demonstrated in Chapter 2.

Core@shell materials like Ni@SiO_2 nanospheres and nanotubes should be exclusively investigated for reactions where control of the composition of the gas phase in contact with the catalyst surface is desirable. In particular, the core@shell nanostructure should be investigated for designated water-gas shift catalysts. Because the water-gas shift reaction is exothermic, its equilibrium increasingly favors reactants with increasing temperature. Most water-gas shift catalysis research reasonably accepts that reaction selectivity is limited by equilibrium, and seeks to increase the activity of water-gas shift catalysts at lower temperatures where equilibrium is more in favor of products. However, if indeed the core@shell nanostructure is effective at removing H_2 from the catalytically active core, resulting in a membrane nanoreactor, this represents a fundamentally different yet simple approach to water-gas shift catalyst engineering. Furthermore, water-gas shift catalysts require much lower operating temperatures than reforming catalysts, which would alleviate the concern of shell sintering.

References

[1] Song, C. Fuel processing for low-temperature and high-temperature fuel cells: Challenges, and opportunities for sustainable development in the 21st century. *Catal. Today* **2002**, *77*, 17-49.

[2] Jain, S.; Chen, H.; Schwank, J. Techno-economic analysis of fuel cell auxiliary power units as alternative to idling. *J. Power Sources* **2006**, *160*, 474-484.

[3] Gould, B.; Chen, X.; Schwank, J. *n*-Dodecane reforming over nickel-based monolith catalysts: deactivation and carbon deposition. *Appl. Catal., A* **2008**, *334*, 277-290.

[4] Liu, J.; Yang, H.Q.; Kleitz, F.; Chen, Z.G.; Yang, T.; Strounina, E.; Lu, G.Q.; Qiao, S.Z. Yolk–Shell Hybrid Materials with a Periodic Mesoporous Organosilica Shell: Ideal Nanoreactors for Selective Alcohol Oxidation. *Adv. Funct. Mater.* **2012**, *22*, 591-599.

[5] Cao, A.; Lu, R.; Veser, G. Stabilizing Metal Nanoparticles for Heterogeneous Catalysis. Phys. Chem. Chem. Phys. **2010**, *12*, 13499-13510.

[6] Lee, J.; Park, J. C.; Song, H. A nanoreactor framework of a Au@SiO_2 yolk/shell structure for catalytic reduction of *p*-nitrophenol. *Adv. Mater.* **2008**, *20*, 1523-1528.

[7] Arnal, P. M.; Comotti, M.; Schüth, F. High-temperature-stable catalysts by hollow sphere encapsulation. *Angew. Chem. Int. Ed.* **2006**, *45*, 8224-8227.

[8] Somorjai, G. A.; Rioux, R. M. High technology catalysts towards 100% selectivity: Fabrication, characterization and reaction studies. *Catal. Today* **2005**, *100*, 201-215.

[9] Ikeda, S.; Ishino, S.; Harada, T.; Okamoto, N.; Sakata, T.; Mori, H.; Kuwabata, S.; Torimoto, T.; Matsumura, M. Ligand-free platinum nanoparticles encapsulated in a hollow porous carbon shell as a highly active heterogeneous hydrogenation catalyst. *Angew. Chem. Int. Ed.* **2006**, *45*, 7063-7066.

[10] Yin, Y.; Rioux, R. M.; Erdonmez, C. K.; Hughes, S.; Somorjai, G. A.; Alivisatos, A. P. Formation of hollow nanocrystals through nanoscale Kirkendall effect. *Science* **2004**, *304*, 711-714.

[11] Huang, X.; Guo, C.; Zuo, J.; Zheng, N.; Stucky, G. D. An assembly route to inorganic catalytic nanoreactors containing sub-10-nm gold nanoparticles with anti-aggregation properties. *Small* **2009**, *5*, 361-365.

[12] Chen, W.; Pan, X.; Bao, X. Tuning of redox properties of iron and iron oxides via encapsulation within carbon nanotubes. *J. Am. Chem. Soc.* **2007**, *129*, 7421-7426.

[13] Pan, X.; Fan, Z.; Chen, W.; Ding, Y.; Luo, H.; Bao, X. Enhanced ethanol production inside carbon-nanotube reactors containing catalytic particles. *Nat. Mater.* **2007**, *6*, 507-511.

[14] Dahlberg, K.; Schwank, J. Synthesis of Ni@SiO_2 nanotube particles in a water-in-oil microemulsion template. *Chem. Mater.* **2012**, *24*, 2635-2644.

[15] Takenaka, S.; Umebayashi, H.; Tanabe, E.; Matsune, H.; Kishida, M. Specific performance of silica-coated Ni catalysts for the partial oxidation of methane to synthesis gas. *J. Catal.* **2007**, *245*, 392-400.

[16] Li, L.; He, S.; Song, Y.; Zhao, J.; Ji, W.; Au, C.-T. Fine-tunable Ni@porous silica core–shell nanocatalysts: Synthesis, characterization, and catalytic properties in partial oxidation of methane to syngas. *J. Catal.* **2012**, *288*, 54-64.

[17] Takenaka, S.; Orita, Y.; Umebayashi, H.; Matsune, H.; Kishida, M. High resistance to carbon deposition of silica-coated Ni catalysts in propane steam reforming. *Appl. Catal., A* **2008**, *351*, 189-194.

[18] Dreyer, B., Lee, I., Krummenacher, J., Schmidt, L. Autothermal steam reforming of higher hydrocarbons: *n*-Decane, n-hexadecane, and JP-8. *Appl. Catal., A* **2006**, *307*, 184-194.

[19] Yoon, S.; Kang, I.; Bae, J. Suppression of ethylene-induced carbon deposition in diesel autothermal reforming. *Int. J. Hydrogen Energy* **2009**, *3*, 1844-1851.

[20] Yoon, S.; Kang, I.; Bae, J. Effects of ethylene formation in diesel autothermal reforming. *Int. J. Hydrogen Energy* **2008**, *33*, 4780-4788.

[21] Horn, R.; Williams, K.; Degenstein, N.; Bitsch-Larsen, A.; Nogare, D.; Tupy, S.; Schmidt, L. Methane catalytic partial oxidation on autothermal Rh and Pt catalysts: Oxidation and reforming zones, transport effects, and approach to thermodynamic equilibrium. *J. Catal.* **2007**, *249*, 380-393.

[22] Hotz, N.; Osterwalder, N.; Stark, W.; Bieri, N.; Poulikakos, D. Disk-shaped packed bed micro-reactor for butane-to-syngas processing. *Chem. Eng. Sci.* **2008**, *63*, 5193-5201.

[23] Joensen, F.; Rostrup-Nielsen, J.R. Conversion of hydrocarbons and alcohols for fuel cells. *J. Power Sources* **2002**, *105*, 195-201.

[24] Randolph, K.; Dean, A. Hydrocarbon fuel effects in solid-oxide fuel cell operation: An experimental and modeling study of *n*-hexane pyrolysis. *Phys. Chem. Chem. Phys.* **2007**, *9*, 4245-4258.

[25] Rostrup-Nielsen, J.R. Syngas in perspective. *Catal. Today* **2002**, *71*, 243-247.

[26] Dorazio, L.; Castaldi, M. Autothermal reforming of tetradecane ($C_{14}H_{30}$): A mechanistic approach. *Catal. Today* **2008**, *136*, 273-280.

[27] Gould, B.; Chen, X.; Schwank, J. Dodecane reforming over nickel-based monolith catalysts. *J. Catal.* **2007**, *250*, 209-221.

[28] Tadd, A.; Gould, B.; Schwank, J. Packed bed versus microreactor performance in autothermal reforming of isooctane. *Catal. Today* **2005**, *110*, 68-75.

[29] Gould, B.; Tadd, A.; Schwank, J. Nickel-catalyzed autothermal reforming of jet fuel surrogates: *n*-dodecane, tetralin, and their mixture. *J. Power Sources* **2007**, *164*, 344-350.

[30] Erri, P.; Dinka, P.; Varma, A. Novel perovskite-based catalysts for autothermal JP-8 fuel reforming. *Chem. Eng. Sci.* **2006**, *61*, 5328-5333.

[31] Wei, J., Iglesia, E. Isotopic and kinetic assessment of the mechanism of reactions of CH_4 with CO_2 or H_2O to form synthesis gas and carbon on nickel catalysts. *J. Catal.* **2004**, *224*, 370-383.

[32] Nikolla, E.; Schwank, J.; Linic, S. Comparative study of the kinetics of methane steam reforming on supported Ni and Sn-Ni alloy catalysts: The impact of the formation of Ni alloy on chemistry. *J. Catal.* **2009**, *263*, 220-227.

[33] Tanaka, Y.; Kato, T. Reforming of methane, ethylene, and desulfurized kerosene over Ni-YSZ catalyst. *Appl. Catal., A* **2008**, *348*, 229-235.

[34] Laosiripojana, N.; Sangtongkitcharoen, W.; Assabumrungrat, S. Catalytic steam reforming of ethane and propane over CeO_2-doped Ni/Al_2O_3 at SOFC temperature:

Improvement of resistance toward carbon formation by redox property of doping CeO_2. *Fuel* **2006**, *85*, 323-332.

[35] Resini, C.; Concepcion, M.; Delgado, H.; Arrighi, L.; Alemany, L.; Marazza, R.; Busca, G. Propene versus propane steam reforming for hydrogen production over Pd-based and Ni-based catalysts. *Catal. Commun.* **2005**, *6*, 441-445.

[36] Modafferi, V.; Panzera, G.; Baglio, V.; Frusteri, F.; Antonucci, P. Propane reforming on Ni-Ru/GDC catalyst: H_2 production for IT-SOFCs under SR and ATR conditions. *Appl. Catal., A* **2008**, *334*, 1-9.

[37] Graf, P.; Mojet, B.; Ommen, J.; Leferts, L. Comparative study of steam reforming of methane, ethane and ethylene on Pt, Rh and Pd supported on yttrium-stabilized zirconia. *Appl. Catal., A* **2007**, *332*, 310-317.

[38] Pengpanich, S.; Meeyoo, V.; Rirksomboon, T.; Schwank, J. Hydrogen production from partial oxidation of iso-octane over Ni/$Ce_{0.75}Zr_{0.25}O_2$ and Ni/β"-Al_2O_3 catalysts. *Appl. Catal., A* **2006**, *302*, 133-139.

[39] Chen, X.; Tadd, A.; Schwank, J. Carbon deposited on Ni/Ce-Zr-O isooctane autothermal reforming catalysts. *J. Catal.* **2007**, *251*, 374-387.

[40] Bengaarda, H.S.; Norskova, J.K.; Sehestedb, J.; Clausen, B.S.; Nielsenb, L.P.; Molenbroekb, A.M.; Rostrup-Nielsen, J.R. Steam reforming and graphite formation on Ni catalysts. *J. Catal.* **2002**, *209*, 365-384.

[41] Chen, X.; Gould, B.; Schwank, J. *n*-Dodecane reforming over monolith-based Ni catalysts: SEM study of axial carbon distribution profile. *Appl. Catal., A* **2009**, *356*, 137-147.

[42] Nikolla, E.; Schwank, J.; Linic, S. Promotion of the long-term stability of reforming Ni catalysts by surface alloying. *J. Catal.* **2007**, *250*, 85-93.

[43] Nikolla, E.; Schwank, J.; Linic, S. Hydrocarbon steam reforming on Ni alloys at solid oxide fuel cell operating conditions. *Catal. Today* **2008**, *136*, 243-248.

[44] Pengpanich, S.; Meeyoo, V.; Rirksomboon, T.; Schwank, J. *iso*-Octane partial oxidation over Ni-Sn/$Ce_{0.75}Zr_{0.25}O_2$ catalysts. *Catal. Today* **2008**, *136*, 214-221.

[45] Westrich, T.A.; Chen, X.; Schwank, J.W. Isooctane decomposition and carbon deposition over ceria-zirconia supported nickel catalysts. *Appl. Catal., A* **2010**, *386*, 83-93.

Chapter 4

Photocatalytic promotion of ethylene oxidation on gold nanoparticles supported on titania

Introduction

Concerns over the long-term availability and environmental consequences of non-renewable energy sources such as oil, coal, and natural gas have motivated the research and development of technologies that utilize the energy abundantly available in sunlight. Photocatalysis uses solar energy to drive chemical reactions, either to store energy in chemical bonds, such as in water splitting to H_2. Other photocatalyst technologies with environmental motivations are the degradation or removal of pollutants from water or air, such as heavy metal cations in aqueous waste streams or volatile organic compounds (VOC) in air. In photocatalytic reactions, light is absorbed by a semiconductor if it has energy exceeding the semiconductor band gap to produce energetic electrons and holes. These energetic charge carriers can then react directly or indirectly with reactants. TiO_2 is an attractive photocatalytic material because it is non-toxic, earth-abundant, photochemically stable, and inexpensive [1,2]. TiO_2 can absorb light with wavelengths less than approximately 400 nm, approximately the UV portion of the solar spectrum, about 5% of the total energy flux.

The limitations of semiconductor photocatalysis are well-known, and their low efficiency is primarily the result of charge carrier recombination and saturated photoactivity at higher intensities. The performance of photocatalysts may be improved by controlling particle size, phase composition, coupling two or more semiconductors, and doping [3]. Deposition of metal nanoparticles onto semiconductors, associated with the phenomenon of Fermi level equilibration [4,5,6,7], has become another method for improving the performance of photocatalysts. When metal nanoparticles are in contact with a semiconductor, photo-generated electrons in the semiconductor can transfer to metal nanoparticles, raising their Fermi level. In the absence of an electron scavenger, electrons can accumulate in metal nanoparticles until their Fermi level increases to that of the semiconductor, at which point their Fermi levels are "equilibrated." This effect is well-known to decrease the rates of charge carrier recombination in photocatalysts, resulting in enhanced rates of the photocatalytic hydrogen evolution reaction [1,8,9,10,11,12], photocatalytic oxidation of organic molecules [13], and photocatalytic steam reforming of methanol [14].

Recently, Westrich *et al*. showed that photo efficiency increased for photocatalytic oxidation of ethylene, a representative VOC, on TiO_2 with increasing temperature, reaching a maximum activity between 150°C and 200°C, the first time semiconductor photocatalysis was studied at temperatures higher than 110°C [15]. At temperatures higher than 200°C, Westrich and coworkers found that the increasing rate of phonon-based recombination predominated and photoactivity decreased. Not only was photocatalytic oxidation of a VOC demonstrated at elevated temperature, extending this application to conditions relevant to heterogeneous catalysis, but another means for improving photo efficiency was shown.

Recently plasmonic nanostructures have been shown to facilitate photocatalytic reactions at high temperatures [16,17]. Plasmons are energetic oscillations of electrons on the surface of metal nanoparticles such as Ag or Au that occur with absorption of photons at a characteristic resonant wavelength. But this fundamentally different photocatalytic mechanism depends strongly on a specific metal and highly controlled metal particle shape. While plasmon

photocatalysts holds promise for certain targeted reactions, they may not be able to replace more generally applicable semiconductor photocatalysts.

If the transfer of photo-generated electrons to metal nanoparticles occurs at elevated temperatures, there are two implications that build directly upon the work of Westrich *et al*. that should be explored. First, at increased temperatures where TiO_2 photoactivity is maximized, the deposition of metal nanoparticles may cause a further increase. Second, the transfer of electrons to metal nanoparticles would be expected to have a large effect on the activity of the metal at temperatures where it is thermally active. The latter case may represent a new frontier of photocatalysis, photo-enhanced heterogeneous catalysis, wherein energy from sunlight could either offset the energy for breaking the bonds of reactants usually supplied by heat derived from non-renewable sources, or alter the energetics of catalysts in novel ways and open up new possibilities for tuning their properties. This could have numerous indirect implications for sustainability, such as greater industrial efficiency and less cost-restrictive implementation of new environmental technologies.

Two well-known phenomena that involve a similar transfer of charge to metal nanoparticles in heterogeneous catalysts at high temperature are surface doping of electron donors such as alkali metals [18,19], and electrochemical promotion, also known as non-faradaic electrochemical modification of catalyst activity (NEMCA) or electrochemical promotion of catalysis (EPOC) [20,21]. However, electron donor species have only localized effects on the catalyst surface, and EPOC is typically associated with engineering difficulties.

To investigate the potential for an electron transfer promotion effect with photon irradiation, and the potential increase in photo efficiency at high temperatures due to deposited metal nanoparticles, the effect of UV irradiation on ethylene oxidation on TiO_2 and 1 wt% Au/TiO_2 at steady state at temperatures between 50 and 500°C was studied using a novel photocatalytic reactor. The concentration of H_2O is expected to have a significant effect on photocatalytic ethylene oxidation at elevated temperature, though this effect has not been studied; therefore

experiments with 0 and 2.6 kPa H_2O were performed. Steady-state, in-situ DRIFTS experiments were used to observe the surface species present on TiO_2 and Au/TiO_2 during the photocatalytic reaction, to investigate the catalytic contributions of Au and TiO_2, the nature of surface hydroxyl species and surface intermediates, and the contributions of thermal and photocatalytic reactions.

Background of metal-support photocatalysis

When a semiconductor is irradiated with light with photon energy greater than the band gap energy, electrons in the valence band are promoted to the conduction band. Photo generated electrons and holes can undergo recombination which limits their lifetime and therefore their probability of facilitating chemical reactions. Recombination can be monitored with photoluminescence (PL) spectroscopy [22]. Electrons and holes not undergoing recombination may become trapped and accumulate on the semiconductor surface, raising the semiconductor Fermi level to near the bottom edge of the conduction band. Photo-generated electrons in TiO_2 are trapped at surface Ti(IV) sites, which results in a broad absorption of light in the red region and a blue visual appearance [5,6,7]. Holes can be trapped by surface hydroxyl groups, producing highly oxidizing hydroxyl radicals. Hydroxyl radical formation can be observed by PL spectroscopy in the presence of terephthalic acid [13,22]. Terephthalic acid is oxidized by hydroxyl radicals to 2-hydroxyterephthalic acid, which fluoresces at 425 nm.

Metals typically have a lower Fermi level than that of pre-irradiated TiO_2, so if a metal nanoparticle is in intimate contact with TiO_2, photo-generated electrons may transfer to the metal conduction band [5,6]. This places a negative charge on metal particles, inducing a space charge layer in the semiconductor at the metal-semiconductor interface (i.e., a Schottky barrier). Photo-generated electrons transfer to the metal until the metal Fermi level is raised to a level equal to that of the semiconductor, resulting in “Fermi level equilibration” [6].

The transfer of electrons to metal nanoparticles can be monitored by observing the surface plasmon absorption peak with UV-vis spectroscopy. As electrons accumulate, electron density increases, and the surface plasmon absorption peak blue-shifts according to a well-defined equation [4,6,22]. The electrons accumulated in metal nanoparticles may also be observed by titration with an electron acceptor, such as the dye thionine [6]. The transfer of photo generated electrons to metal nanoparticles reduces the rate of recombination, which can be observed by decreased PL emission for a semiconductor with deposited metal nanoparticles compared to the semiconductor alone. For example, a monotonic decrease in PL emission from ZnO was observed with increasing Ag loading [22]. The combined evidence given by these techniques has provided strong evidence that the transfer of photo generated electrons to metal nanoparticles is the predominant charge transfer pathway occurring in these semiconductor systems. The stability of electrons accumulated in metal nanoparticles in the absence of an electron scavenger rules out other hypothesized pathways, such as recombination of electrons transferred to metal nanoparticles with holes in the semiconductor, or promotion of electrons in metal nanoparticles through photo absorption to the semiconductor conduction band.

The enhancement of photocatalytic reaction rate for semiconductors with deposited metal nanoparticles has been shown to trend with the metal's work function, with enhancement increasing as Ag < Au < Pt [9,13,14]. The metal type has also been reported to affect the nature of the transfer of photo-generated electrons to metal nanoparticles, which may be either ohmic or charging in nature [3,4]. Au is understood to have a charging nature, because electrons accumulate in Au nanoparticles, and the Fermi level decreases to more negative potentials and is not in equilibrium with redox couples in the surrounding medium. Pt however is understood to be ohmic, because electrons are not stored in Pt nanoparticles but are quickly transferred to redox couples in the surrounding medium [7,23].

Photoactivity has been shown to exhibit a maximum enhancement with varying metal loading [8,9,22]. This may be partially due to blocking of surface sites at higher loading. For example,

for Au/$KTiNbO_5$ samples with similar Au particle size synthesized by the same photodeposition method, the higher loading led to lower H_2 evolution rate. Other effects might be the increasing rate of non-radiative recombination at higher loading [22].

Experimental

TiO_2 having a phase composition of 85 wt% anatase and 15 wt% rutile was prepared by flame-spray pyrolysis by the Richard Laine Laboratory. 1 wt% Au/TiO_2 samplers were prepared by photodeposition. 1 g of TiO_2 was dispersed in a Pyrex flask containing a solution of 200 mL deionized water, 20 mL ethanol, and an appropriate amount of chloroauric acid. After the suspension was stirred for 30 min in ambient light, it was irradiated at an approximate distance of 2 in by a UV lamp for 30 min. The UV lamp was a UVP B-100AP high intensity lamp, which supplies 0.0217 W/cm^2 of 365 nm light at a distance of 2 in. After irradiation, the suspension became purple, indicating the formation of Au nanoparticles. The solids were separated by centrifugation at 9000 relative centripetal force for 20 min, then washed three times with 50 mL deionized water, then washed three times with 4 M NH_3 solution, with intermittent centrifugation separations. The washed solids were dried overnight at approximately 100°C. The dry powder was then crushed and ground to a fine grain size using a mortar and pestle.

The specific surface area for TiO_2 was measured using a Micromeritics ASAP 2020 physisorption analyzer. The analysis was performed at 77 K with N_2 adsorbate gas from relative pressures of 0.05 to 0.35. An X-ray diffraction (XRD) pattern for TiO_2 was obtained with a Rigaku rotating anode diffractometer at 40 kV and 100 mA. A scan was run from 10-70° 2θ with a scan rate of 2° 2θ/min with 0.02° intervals. Scherrer particle size and phase composition were measured through Rietveld refinement using MDI Jade 10.0 software.

To observe the particles deposited by photodeposition and obtain a particle size distribution, a specimen of Au/TiO_2 was examined by STEM. 10 mg of Au/TiO_2 powder was dispersed in 2 mL

ethanol and ultrasonicated for 1 hr to break up agglomerates. Catalyst particles were then deposited on carbon films supported on copper grids by adding the suspension drop-wise and allowing the ethanol to evaporate. A JOEL 2010F analytical electron microscope was used for STEM imaging. The instrument was equipped with a zirconated tungsten [100] thermal field tip filament and was operated at 200 kV at a pressure of 1.5×10^{-7} Torr. A probe size of 0.5 nm and camera length of 12 cm was used. High-angle annular dark field (HAADF) STEM images were collected with a Gatan retractable CCD camera. To measure metal particle sizes, the area of each clearly resolved Au particle in the STEM images was measured and converted to the diameter of a circle having the same area with ImageJ software.

Photocatalytic reaction experiments were carried out in a novel reactor system (depicted in Figure 4.1) consisting of a custom designed quartz tube with inline plate zone, a custom milled firebrick to allow simultaneous thermal insulation and UV access to the reactor bed, temperature-controlled heat plate, and Thermofisher Scientific FTIR instrument for analysis of a gas stream. The custom quartz reactor apparatus was fabricated by United Silica, and had 0.25 in tubes (O.D.) at each end, a 1 mm x 1 in x 1 in plate zone, and tapered 1 in transition zones. The custom firebrick was milled by the University of Michigan Auto Lab. A four-way valve acted as a switch for which of two gas streams was directed to the FTIR, the stream leaving the reactor or a stream of reference gas. The reactor system was monitored, controlled, and automated by a program written in Labview. The program recorded the temperature at the back-face of the catalyst bed, the temperature at the heat plate surface, and the pressure difference across the reactor tube while controlling the heat plate power to reach a surface temperature set point, the gas flows through four MKS mass flow controllers, the position of the four-way valve, and the UV lamp power.

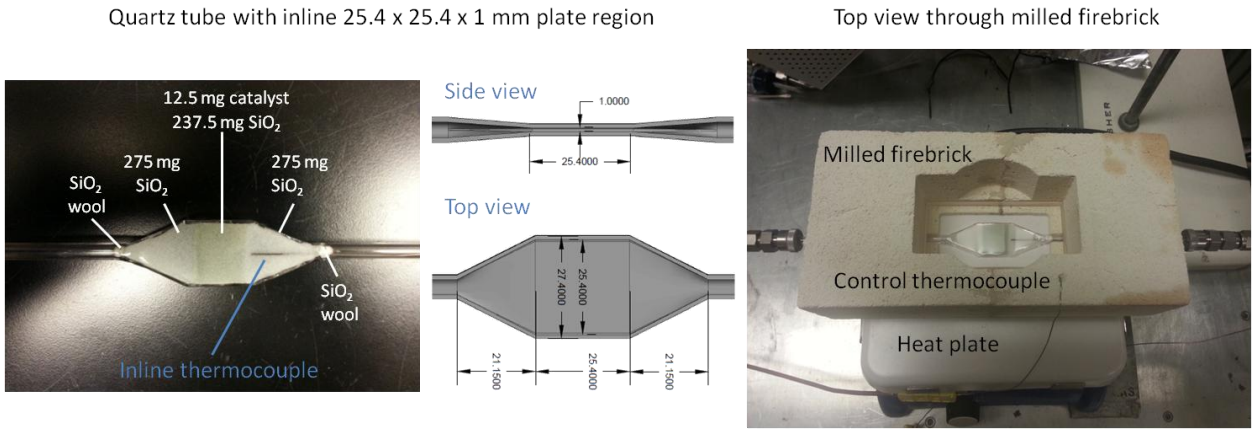

Figure 4.1 Photographs and diagrams of photocatalytic reactor used for ethylene oxidation experiments.

For each photocatalytic reaction experiment, Au/TiO_2 powder was deposited 5 wt% on 35-60 mesh SiO_2 to facilitate even distribution of gas flow and UV irradiation in the reactor bed. The SiO_2 diluent was previously calcined at 800°C for 4 hr to remove its internal pore structure and water absorption capacity. The powder was combined with an appropriate amount of SiO_2 and 20 mL H_2O in a 50 mL beaker. The beaker was covered with parafilm and ultrasonicated for 1 hr. Then the parafilm was removed and the beaker set overnight on a 100°C heat plate surface to obtain a dry powder with even distribution of Au/TiO_2 on SiO_2. To load the quartz reactor with a catalyst sample, the reactor was first thoroughly rinsed with deionized water and ethanol, and then dried with a stream of air. A plug of quartz wool was inserted at the downstream end, then a tubing apparatus with thermocouple was connected through a 0.25 in vacuum fitting such that the thermocouple tip would be positioned at the back face of the catalyst bed. Then 275 mg of 35-60 mesh SiO_2 (previously calcined at 800°C for 4 hr) was added, followed by 250 mg of catalyst sample, followed by another 275 mg SiO_2, and finally an upstream plug of quartz wool. With each addition of powder, the reactor tube was shaken until the powder's upstream face was even and perpendicular to the reactor axis.

The concentrations of products in the gas stream flowing through the FTIR were measured using Omnic software. The signal of each species was an integration of a characteristic IR absorption peak: 2400-2230 cm^{-1} for carbon dioxide, 2230-2000 cm^{-1} for carbon monoxide, and 2858-2719 cm^{-1} for formaldehyde. While each of these signals are not linear with gas

concentration in the full range of 0-1%, especially in the case of CO_2, a linear calibration was accurate in the range of 0-0.2% for CO and CO_2, which was not exceeded in experiments. A linear calibration was assumed for H_2CO in the range of 0-0.2% H_2CO, which also was not exceeded in experiments. Calibrations for CO and CO_2 were performed by flowing each at a concentration of 0.2% through the FTIR. H_2CO was calibrated by observing the signal over time as a known amount of H_2CO was evaporated by flowing N_2.

Photocatalytic ethylene oxidation experiments used a reactant gas with a flow rate of 100 mL/min (at 298 K and 1 atm) containing 3 kPa ethylene, 10 kPa oxygen, and balance nitrogen. For experiments containing H_2O, the reactant stream was bubbled through a water saturator, which resulted in concentrations of water near equilibrium of 2.6 kPa. The reaction was monitored at steady state at 65 min temperature intervals of 50°C between 50°C and 550°C. The pressure drop across the reactor varied proportionally with temperature in the range 0.5-3.0 psi. During each interval, the temperature was raised at 10°C/min for 5 min to the interval set point. After another 30 min, the UV lamp was switched on. After 15 min of irradiation, the UV lamp was switched off. Then after a final 15 min without UV to check for changes in thermal activity, the next interval began. For the first 10 min of each interval, pure nitrogen gas was selected to flow through the FTIR. A linear interpolation of the apparent concentrations of gas species during these nitrogen intervals was subtracted from the steady state data to remove the background, which was especially important for CO_2.

The steady state reaction rates for thermal (no UV irradiation) and photothermal (with UV irradiation) catalytic ethylene oxidation were calculated from the background-corrected concentrations of the oxidation products formaldehyde, carbon monoxide, and carbon dioxide. Transient data were neglected by averaging concentrations during the final 2/3 of each interval. The average for the photothermal interval was reported as the photothermal measurement. The two thermal averages were consistently found to be similar within experimental error, and their average was reported as the thermal measurement. The three oxidation products each contained one carbon atom, so a reaction rate for ethylene oxidation was calculated for each

species as 1/2 of its formation rate. The total ethylene conversion was always below 5%, assuring that the observed reaction rates were kinetically limited.

In-situ DRIFTS experiments were performed to investigate the effects of UV irradiation on the intermediate surface species that form on TiO_2 and Au/TiO_2 during photocatalytic ethylene oxidation. The instrument used was a Bruker Optics Tensor 27 Infrared Spectrometer equipped with a Harrick Scientific Praying Mantis IR accessory and high temperature reaction vessel. Before loading each sample, the sample cell was cleaned with ethanol and heated to 200°C to remove ethanol residue. The sample was then loaded and pretreated at the test temperature for 2 hr under 100 sccm flowing N_2. Following the pretreatment, a background scan was collected and applied, and a stable, flat spectrum was confirmed. The reaction mixture was then introduced, 70 sccm of ethylene (6% C_2H_4, balance N_2) and 70 sccm oxygen (20% O_2, balance N_2). IR spectra were collected every 5 min for 30 min. Then the UV was switched on and spectra continued to be collected every 5 min for another 30 min.

Results and Discussion

Characterization of TiO_2 and Au/TiO_2

The BET specific surface area of TiO_2 prepared by flame-spray pyrolysis was calculated to be 70 m^2/g from N_2 physisorption analysis. The average particle size derived from BET was 22 nm assuming densities of 4.25 g/cm^3 for rutile and 3.90 g/cm^3 for anatase. From XRD data, the crystallite sizes calculated from the Scherrer equation were 35 nm for the anatase phase and 38 nm for the rutile phase. The phase composition calculated from Rietveld refinement was 85±1 wt% anatase and 15±1 wt% rutile. A particle size distribution was assembled for 114 Au particles from several STEM HAADF images (Figure 4.2), and showed a number-average particle size of 11.6 nm.

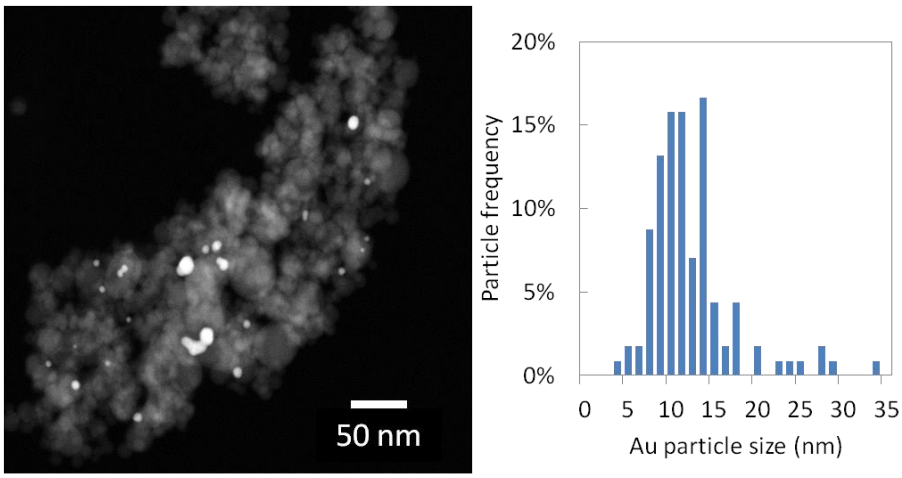

Figure 4.2 Representative STEM HAADF image of 1% Au/TiO_2 prepared via photodeposition and Au particle size distribution.

TiO_2 photocatalytic ethylene oxidation experiments

Since hydroxyl groups are known to have a major role in photocatalytic oxidation reactions [24], experiments with and without H_2O were expected to reveal important details about photocatalytic behavior at elevated temperatures and allow better comparison of TiO_2 and Au/TiO_2 photocatalysis.

Thermal activation of C_2H_4 oxidation, indicated by the appearance of CO_2, occurred at 450°C with H_2O, and 350°C without H_2O (Figure 4.3(a) and (c), respectively). Photocatalytic formation of CO_2 was observed at all temperatures in the range 50-500°C; with H_2O a maximum photocatalytic rate of CO_2 formation was observed at 120°C (Figure 4.3(b) and (g)), and without H_2O a maximum appeared with a lower rate at 270°C (Figure 4.3(d) and (h)). When H_2O but no O_2 was present, no thermal or photocatalytic oxidation products were observed up to 500°C (Figure 4.3(e) and (f)).

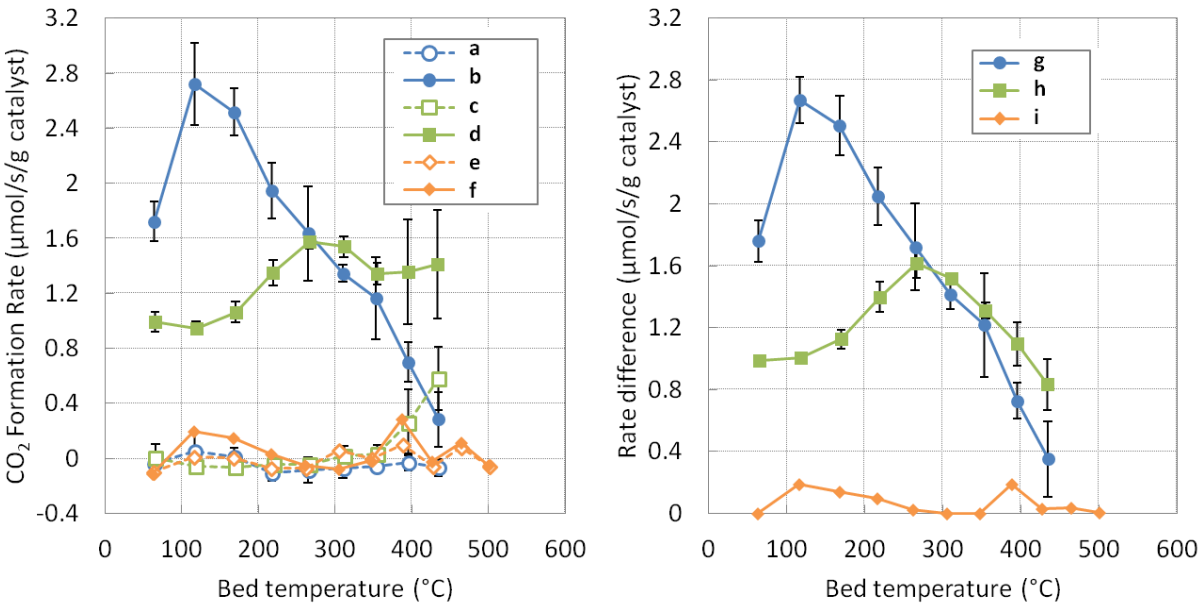

Figure 4.3 Photocatalytic CO_2 formation rates on TiO_2 between 50°C and 500°C under conditions of (a) thermal-only (no UV irradiation) with 2.6 kPa H_2O and 10 kPa O_2, (b) photothermal (with UV irradiation) with 2.6 kPa H_2O and 10 kPa O_2, (c) thermal-only with no H_2O and 10 kPa O_2, (d) photothermal with no H_2O and 10 kPa O_2, (e) thermal-only with 2.6 kPa H_2O and no O_2, and (f) photothermal with 2.6 kPa H_2O and no O_2. Differences between thermal-only and photothermal CO_2 formation rates on TiO_2 between 50°C and 500°C under conditions of (g) 2.6 kPa H_2O and 10 kPa O_2, (h) no H_2O and 10 kPa O_2, and (i) 2.6 kPa H_2O and no O_2.

H_2CO and CO partial oxidation products were also significant, and formed thermally above approximately 350°C both with and without H_2O (data not shown), though with H_2O, H_2CO formation was observed at temperatures as low as 150°C. Thermal formation rates of both H_2CO and CO were higher without H_2O. Photocatalytic formation of H_2CO and CO occurred above 50°C and increased with increasing temperature, each reaching formation rate maxima around 400°C (Figure 4.4(b) and (c)). Product selectivities were similar for CO but different for H_2CO with and without H_2O; more H_2CO was formed without H_2O, and in the presence of H_2O photocatalytic formation of H_2CO was not observed until 250°C.

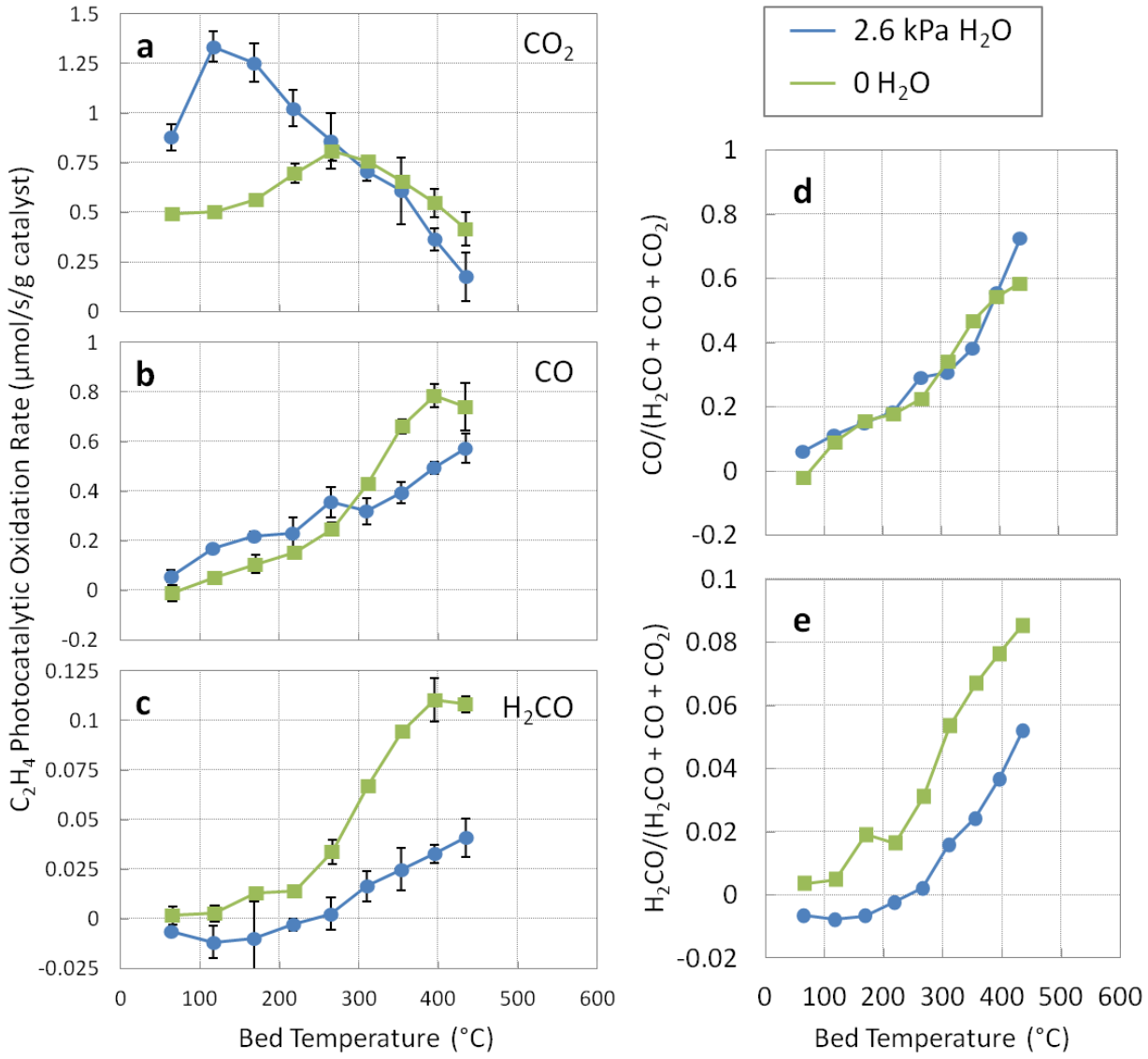

Figure 4.4 Rates of photocatalytic ethylene oxidation on TiO_2 between 50°C and 500°C with and without H_2O to (a) CO_2, (b) CO, and (c) H_2CO. Selectivities between 50°C and 500°C on TiO_2 to partial oxidation products (d) CO and (e) H_2CO.

One half of the photocatalytic formation rate of each product may be equated to the rate of C_2H_4 photocatalytic oxidation to that product, as shown in Figure 4.4(a)-(c). When the sum of C_2H_4 photocatalytic oxidation rates for each product is plotted versus temperature for the cases with and without H_2O (Figure 4.5), three remarkable effects of H_2O are immediately seen. First, H_2O enhances photoactivity at low temperature and inhibits photoactivity at high temperature, for total C_2H_4 oxidation as well as for each product. Second, the C_2H_4 oxidation rate temperature maxima are 120°C with H_2O, and 400°C without H_2O. Third, the absence of H_2O

results in a higher selectivity to H_2CO. The implications of these effects are an important expansion of the existing knowledge of high temperature photocatalysis, as will be explained below.

H_2O is clearly not a significant reactant, and molecular oxygen is required for photocatalytic C_2H_4 oxidation, as shown by the experiments without H_2O and without O_2. In the experiment without O_2, no products were observed. In the experiment without H_2O, full conversion could only produce 2/3 of the oxygen in H_2O required for the next turnover. But H_2O significantly enhances the photocatalytic reaction in the temperature range 100-200°C, likely by increasing the coverage of surface hydroxyl groups [25]. Hydroxyl radicals formed from holes reacting with adsorbed H_2O or surface hydroxyl groups are well-known to facilitate photocatalytic oxidation of ethanol at 30°C [26], as well as many other compounds at temperatures below 100°C [24].

A maximum photocatlytic rate near 150°C was proposed by Westrich *et al*. to be caused by the relative contributions with increasing temperature of an increasing kinetic reaction rate and a decreasing fraction of productive photo-generated charge carriers due to phonon recombination [15]. However his experiments were all performed with H_2O, and he did not measure oxidation products other than CO_2. Indeed, the experiments in this study with H_2O had similar results, with a maximum rate near 120°C and high selectivity towards CO_2.

However when H_2O was absent, the photocatalytic behavior at high temperature was significantly different. Surprisingly, a maximum in photocatalytic C_2H_4 oxidation rate occurred at a much higher temperature of 400°C. In addition, the opposite effect of H_2O occurred at higher temperatures; the formation rates of each product increased with H_2O below about 280°C, but decreased with H_2O above 280°C. These observations suggest that two different photocatalytic reaction pathways take place on TiO_2. Pathway A, previously observed and studied by Westrich *et al*., is enhanced by H_2O and has a maximum rate at 120°C; and Pathway B, previously unknown, is inhibited by H_2O, has a higher kinetic activation energy, and has a maximum rate at

400°C. The inhibition of Pathway B by H_2O may be due to H_2O adsorption on the unknown active sites of Pathway B.

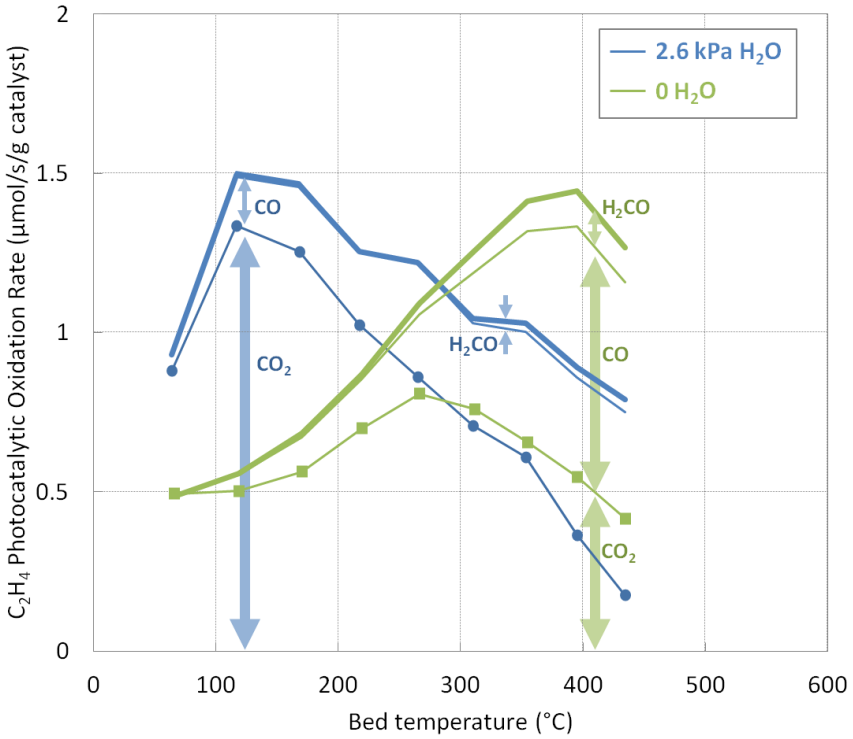

Figure 4.5 Total photocatalytic ethylene oxidation rate on TiO_2 between 50°C and 500°C with and without H_2O, showing the contributions of each product.

Pathway A and Pathway B can be further distinguished by analysis of oxidation product selectivities observed during experiments. First, the similar effects of temperature on both pathways must be determined. Based on the evidence of the effect of H_2O and the temperatures of rate maxima, Pathway A is expected to be more prevalent at low temperatures with H_2O, and Pathway B is expected to be more prevalent at high temperatures without H_2O. Therefore, for both pathways the selectivity to partial oxidation products increases with increasing temperature, both with and without H_2O (Figure 4.4(d) and (e)). This similar trend for both pathways may be explained by a lower stability of surface intermediates at higher temperatures, where they quickly desorb as partial oxidation products before further reaction with photo-generated charge carriers. Given the similar increasing selectivities to partial oxidation products with increasing temperature during photocatalytic oxidation of ethylene, it

appears that both Pathway A and Pathway B have similar selectivities to CO. However, Pathway B has a higher selectivity to H_2CO than Pathway A.

Whereas Pathway A is likely facilitated by surface hydroxyl groups or adsorbed H_2O activated by photo-generated holes, Pathway B may involve a different active site. It is possible that Pathway B involves direct interaction of ethylene with holes, but adsorption of ethylene would need to be confirmed, as photo-generated electrons and holes have shorter lifetimes than the time required for molecular adsorption [3,24]. With surface hydroxyl groups and adsorbed H_2O being the only widely recognized hole traps on TiO_2, it is reasonable to hypothesize that photo-generated electrons trapped at surface Ti(IV) centers [6] interact with adsorbed molecular oxygen to facilitate Pathway B. Sun *et al*. observed evidence in experiments with TiO_2 of two different photocatalytic formaldehyde oxidation pathways at room temperature, which they proposed were a hole-based pathway prevalent with H_2O and an electron-based pathway prevalent without H_2O [25]. The sites for the electron-based pathway may be oxygen vacancies, and there is strong evidence that these are the active sites for thermal oxidation on TiO_2 [27]. These sites may be blocked by H_2O, causing the rate to decrease in the presence of H_2O, as seen in experiments.

The observed difference in temperature of maximum rate between Pathway A (120°C) and Pathway B (400°C) is predicted by the Westrich model for two different kinetic activation energies. The phonon energy and the number of phonons participating in recombination, the other temperature-independent variables that affect the temperature of maximum rate, are properties of the semiconductor and are not expected to change with the presence of H_2O.

Au/TiO_2 photocatalytic ethylene oxidation experiments

The experiments with TiO_2 demonstrated that chemically productive photo-generated charge carriers are available at temperatures higher than 400°C, far higher than previously known. Thus the temperature range where photogenerated electrons participate in surface chemistry overlaps with the temperature range where heterogeneous catalysts become thermally active. For example, Au/TiO_2 becomes thermally active for C_2H_4 oxidation at 300°C. Rather than solely reacting with adsorbates, it is possible that the Fermi level equilibration phenomenon will occur and photo-generated electrons in TiO_2 will be transferred to Au nanoparticles, accomplishing an electronic promotion.

Thermal activation of C_2H_4 oxidation to CO_2 occurred on Au/TiO_2 at a lower temperature compared to TiO_2, about 300°C both with and without H_2O (Figure 4.6(a) and (c)), but thermal rates were higher without H_2O. Interestingly, photocatalytic formation of CO_2 exhibited a rate maximum at 350°C with H_2O (Figure 4.6(e)) and at 400°C without H_2O (Figure 4.6(f)); and photocatalytic rates of CO_2 formation were higher without H_2O above 350°C. Compared to TiO_2, which had one temperature maximum for CO_2 formation rate, on Au/TiO_2 there were two maxima: one at low temperature (i.e., about 120°C), and one at high temperature (i.e., about 400°C). With H_2O, the maximum photocatalytic rate of CO_2 formation at 120°C was lower on Au/TiO_2 than on TiO_2, but without H_2O the difference was small.

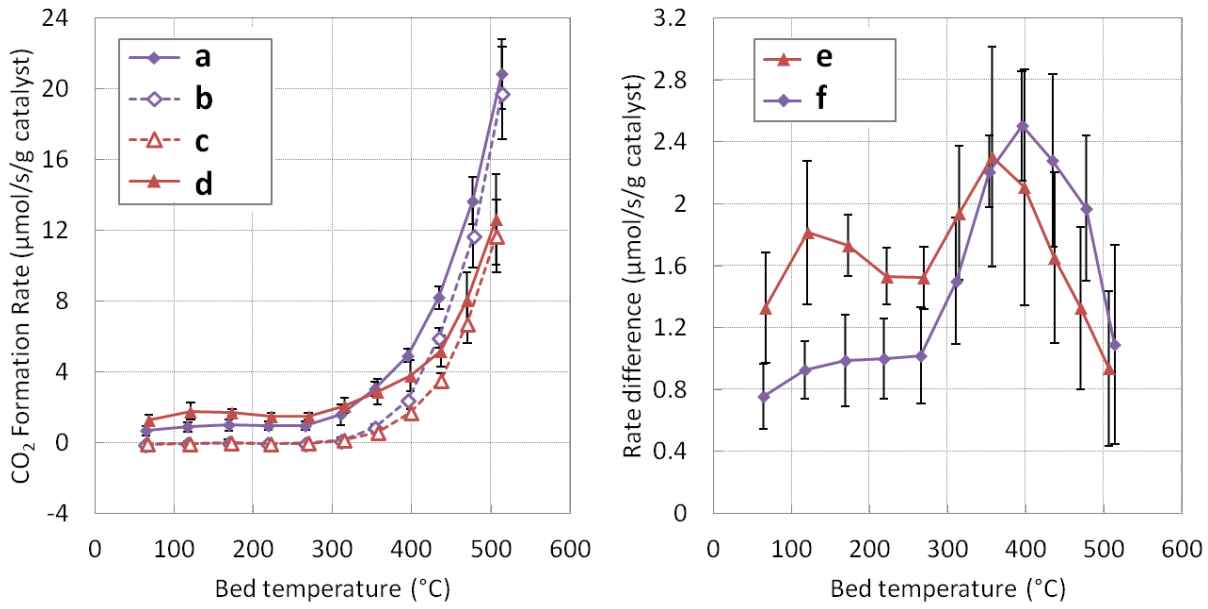

Figure 4.6 Photocatalytic CO_2 formation rates on Au/TiO_2 between 50°C and 500°C under conditions of (a) thermal-only (no UV irradiation) with 2.6 kPa H_2O and 10 kPa O_2, (b) photothermal (with UV irradiation) with 2.6 kPa H_2O and 10 kPa O_2, (c) thermal-only with no H_2O and 10 kPa O_2, and (d) photothermal with no H_2O and 10 kPa O_2. Differences between thermal-only and photothermal CO_2 formation rates on Au/TiO_2 between 50°C and 500°C under conditions of (e) 2.6 kPa H_2O and 10 kPa O_2 and (f) no H_2O and 10 kPa O_2.

Thermal formation of partial oxidation products on Au/TiO_2 occurred above 300°C for CO and above 400°C for H_2CO (data not shown). Contrasting with the results for TiO_2, thermal formation rates were higher with H_2O for Au/TiO_2. As on TiO_2, photocatalytic formations of H_2CO and CO were observed on Au/TiO_2 at temperatures above 50°C (Figure 4.7(b) and (c)). Their formation rates were similar with and without H_2O for the full range of temperatures, including the incidences of rate maxima at 270°C.

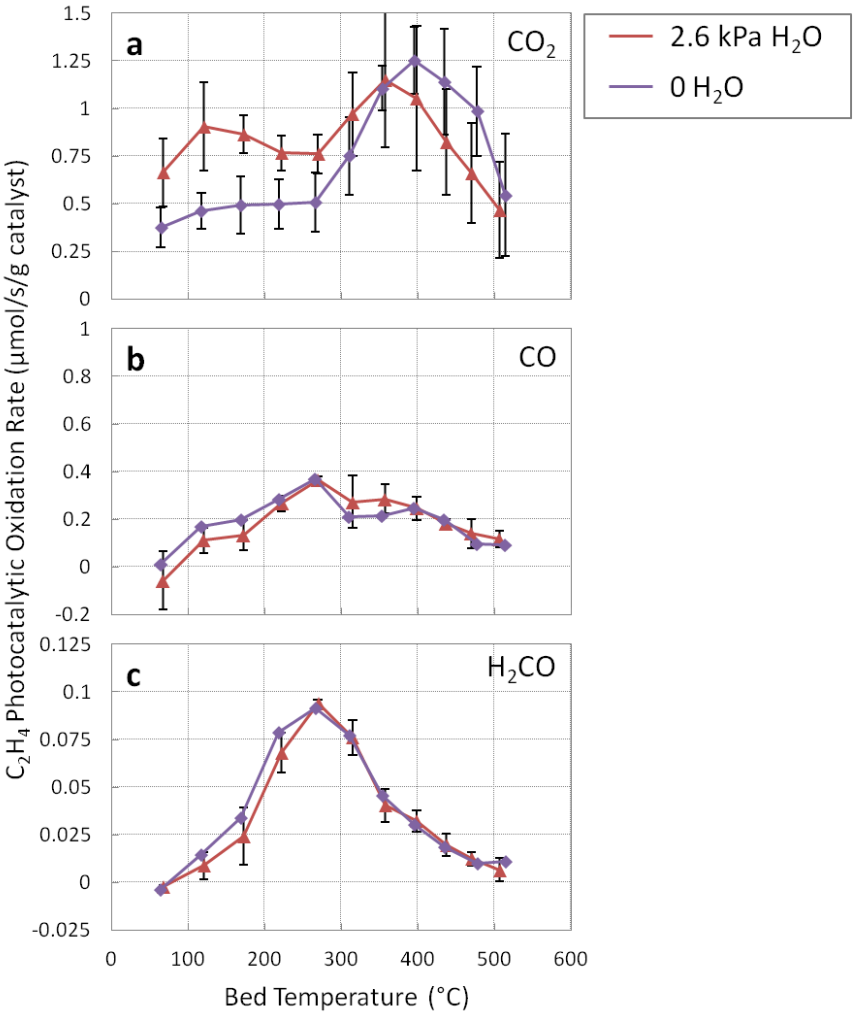

Figure 4.7 Rates of photocatalytic ethylene oxidation on Au/TiO_2 between 50°C and 500°C with and without H_2O to (a) CO_2, (b) CO, and (c) H_2CO.

From separate CO oxidation experiments on a similar Au/TiO_2 catalysts (results not shown), it is known that Au has a higher thermal activity for CO oxidation than for C_2H_4 oxidation, and the same may be true for H_2CO, and so it is expected that H_2CO and CO formed photocatalytically on TiO_2 will be thermally oxidized to CO_2 on Au/TiO_2. This explanation is strongly supported by the combined evidence that, first, the temperature of the CO and H_2CO photocatalytic formation rate maxima coincided with the temperature of thermal activation of C_2H_4 oxidation on Au/TiO_2 (i.e., approximately 300°C), and second, that the temperature of the CO_2 formation rate maximum with Au/TiO_2 coincided with the temperature of the total C_2H_4 oxidation rate maximum with TiO_2 (i.e., approximately 400°C).

Therefore, no component of the observed photocatalytic behavior on Au/TiO_2 may be attributed to Au nanoparticles; effects of the transfer of photo-generated electrons to Au nanoparticles were not observed; neither enhanced TiO_2 photocatalysis due to separation of charge carriers and decreased recombination, nor photocatalytic enhancement of Au catalytic oxidation. As observed by STEM, fresh Au/TiO_2 samples had an average Au particle size (11.6 nm) similar to other studies where electron transfer effects were observed [10,14]. The absence of these effects can be accounted for by a combination of loss of surface hydroxyl species which facilitate Pathway A due to coverage with Au nanoparticles, and Au particle growth at higher temperatures where Pathway B and Au thermal activity are prevalent. These explanations are described in more detail below.

Surface hydroxyl species are likely the active sites of Pathway A, as is well-known from low temperature photocatalytic oxidation studies [24], and as is consistent with the results in this study showing that H_2O strongly enhanced Pathway A while not participating as a reactant. Previous studies have shown how Au nanoparticles deposited by photodeposition on semiconductors can block surface hydroxyl species and thereby limit photocatalytic oxidation rates [2]. Therefore, even if a photocatalytic enhancement of Pathway A occurred, the competing effect of active site removal could have been more significant on observed photocatalytic rates. The effects of electron transfer at lower temperature may be better observed with a different reaction not reliant on surface hydroxyl species, or with Au/TiO_2 samples prepared by methods other than photodeposition such as deposition-precipitation or impregnation which are not known to selectively cover surface hydroxyl species.

Pathway B, prevalent at higher temperatures and having active sites that were blocked by H_2O, clearly different than Pathway A, would not be expected to be affected by coverage of surface hydroxyl species by Au nanoparticles in the same way. But Au particle growth could have easily occurred at higher temperatures (i.e., above approximately 300°C) where Pathway B and Au thermal oxidation activity were prevalent, causing a loss of surface contact area between Au nanoparticles and TiO_2. In separate experiments (not shown), calcination of Au/TiO_2 at 400°C

for 2 hr in air resulted in an average particle size near 35 nm, and similar particle growth likely occurred in photocatalytic ethylene oxidation experiments. The extent of Fermi level equilibration-based enhancement of photocatalysis has been found to be dependent on particle size at low temperatures [5,10,14,28]. The limitation on the transfer of electrons to Au nanoparticles due to particle growth could similarly limit the potential for accumulation of electrons to promote the thermal oxidation activity of Au. Both effects of electron transfer at high temperature may be better observed with Au/TiO_2 samples with smaller and more stable Au particle sizes. Au nanoparticles deposited on TiO_2 via the photodeposition synthesis route are typically large and in poor contact with the semiconductor compared to other routes like impregnation or deposition-precipitation [2,10], and so these latter methods should be employed. Additionally, Au particle sizes may be better stabilized at high temperature by utilizing a core@shell nanostructure, either $Au@TiO_2$ [6] or depositing a layer of porous SiO_2 on Au/TiO_2 [29].

Though experimental results with Au/TiO_2 showed no photocatalytic behavior attributable to Au nanoparticles, they provide further insight into the two photocatalytic pathways occurring on TiO_2: Pathway A facilitated by surface hydroxyl groups, enhanced by H_2O, with a lower kinetic activation energy, and with a lower selectivity to H_2CO; and Pathway B possibly facilitated by oxygen vacancies, inhibited by H_2O, with a higher kinetic activation energy, and with a higher selectivity to H_2CO. Because the deposition of Au nanoparticles on TiO_2 is known to reduce the concentration of surface hydroxyl groups [2], it is expected that Au deposition will decrease the activity of Pathway A while having less effect on Pathway B. Both of these hypotheses were confirmed by total rates of C_2H_4 photocatalytic oxidation on TiO_2 and Au/TiO_2, which showed little difference due to Au without H_2O (Figure 4.8(b)), but a significant decrease in the maximum photocatalytic oxidation rate with Au at 120°C with H_2O where Pathway A is more prevalent (Figure 4.8(a)).

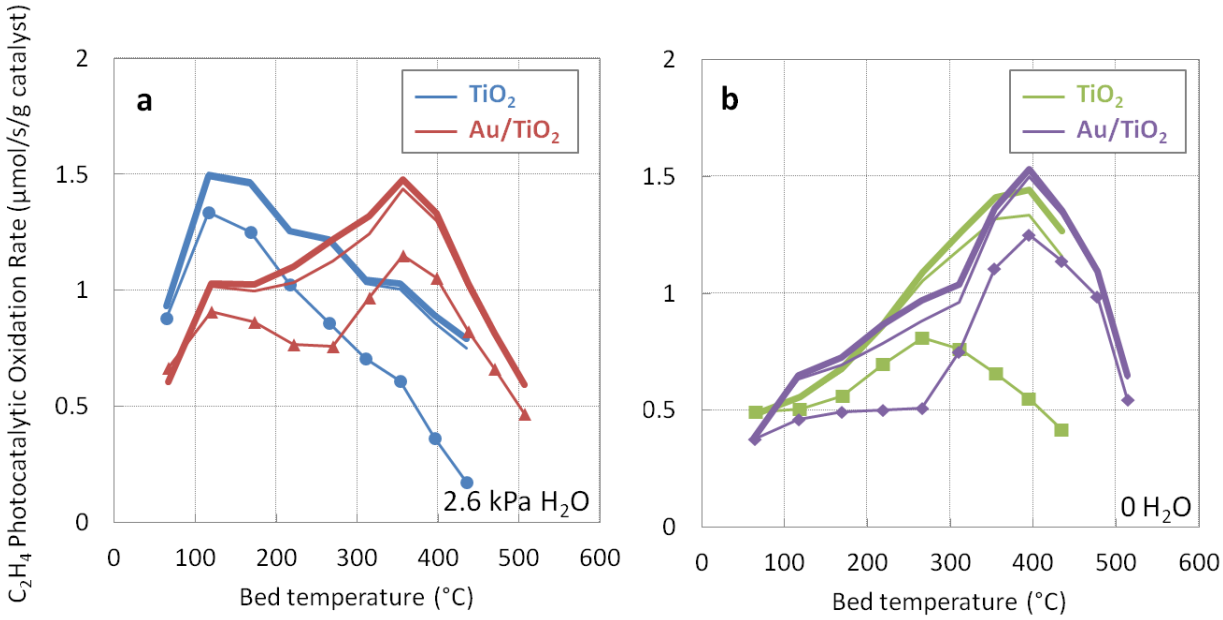

Figure 4.8 Total photocatlaytic ethylene oxidation rate of ethylene oxidation on TiO_2 and Au/TiO_2 between 50°C and 500°C with (a) 2.6 kPa H_2O and (b) no H_2O. For each experiment, the contributions of each product are depicted in the same manner as in Figure 4.5.

Two additional observations showed that deposited Au nanoparticles, while not significantly affecting Pathway B, actually caused Pathway B to be less inhibited by H_2O. First, a photocatalytic oxidation rate maximum appeared at 350°C with H_2O on Au/TiO_2, similar to the rate maximum that appeared at 400°C on TiO_2 with H_2O and on Au/TiO_2 without H_2O. Second, observed H_2CO formation rates were similar with and without H_2O on Au/TiO_2, and were similar to TiO_2 without H_2O, at temperatures below 300°C where Au is not thermally active. The mechanism of this Au-based abatement of H_2O inhibition of Pathway B is unknown and warrants further, perhaps theoretical, investigation.

In-situ DRIFTS experiments

To further investigate differences in the photocatalytic behavior of TiO_2 and Au/TiO_2, and based on the hypothesis of two different reaction pathways prevalent at low and high temperatures (i.e., Pathway A and Pathway B, respectively), in-situ DRIFTS spectra were collected of TiO_2 and

Au/TiO_2 samples under flow of C_2H_4 and O_2 at 120°C and 390°C. DRIFTS spectra in Figure 4.9 show thermal data collected after 30 min under reaction conditions, immediately before UV irradiation, and photothermal data collected after 10 min of irradiation. No significant changes occurred after 30 min without irradiation or after 10 min under irradiation.

No surface species formed without UV irradiation at 120°C, consistent with reaction experiments which showed no thermal activity at 120°C, and absorption peaks only occurred under UV irradiation. Under photothermal conditions, both TiO_2 and Au/TiO_2 had formation peaks at 1573 and 1365 cm^{-1} attributed to surface formate species [26,30] and consumption peaks at 2975, 2928, and 2853 cm^{-1} attributed to C-H bonds of various surface species. However, a broad peak observed at 3664 cm^{-1} attributed to surface hydroxyl and adsorbed H_2O species indicated that surface hydroxyl species formed on the TiO_2 surface but were removed from Au/TiO_2. A second difference was that TiO_2 had a peak at 1540 cm^{-1} in the C-O region belonging to an unknown carbonate species, possibly a second type of formate species [30].

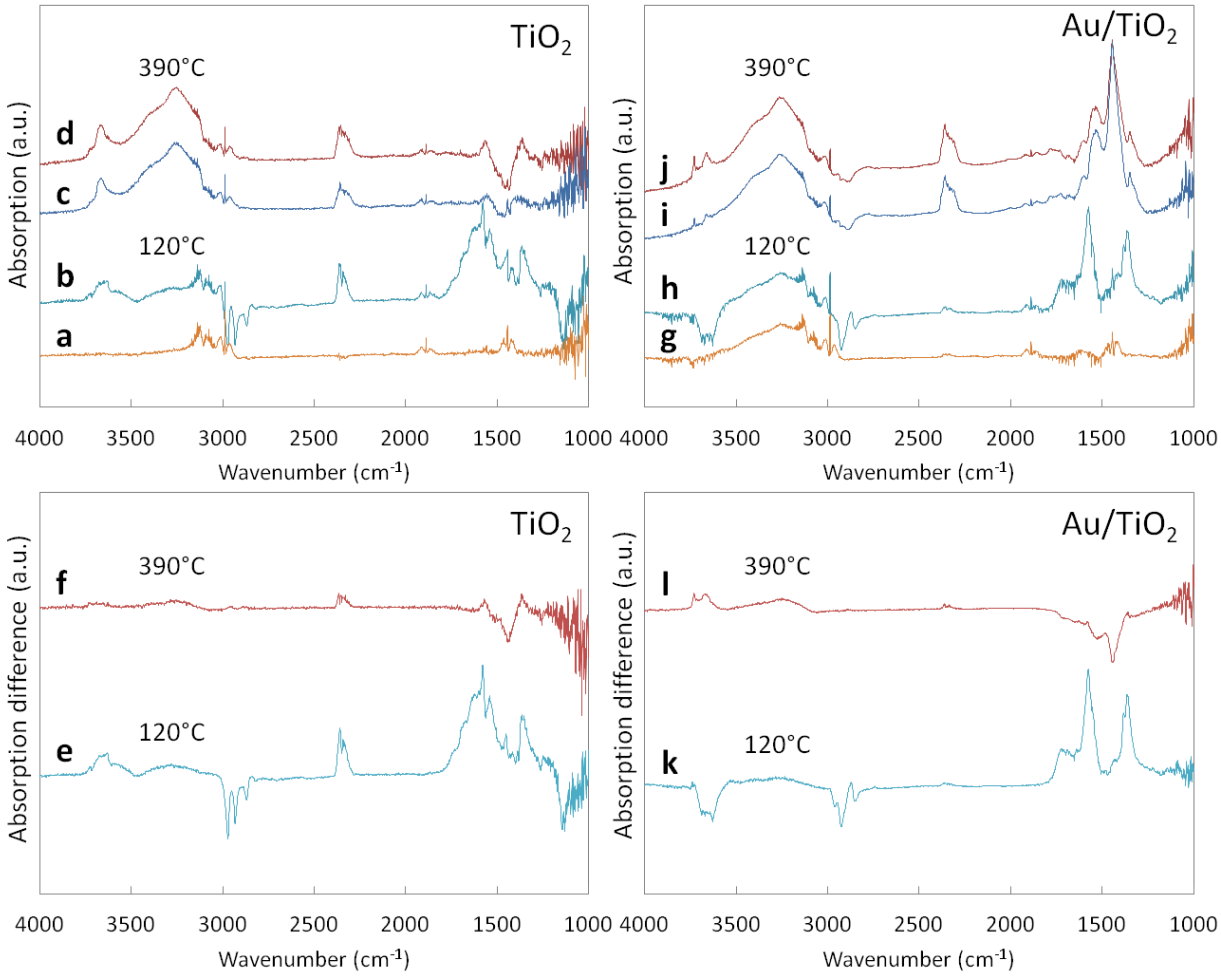

Figure 4.9 In-situ DRIFTS spectra for TiO_2 and Au/TiO_2 under thermal-only and photothermal ethylene oxidation conditions. Spectra for TiO_2 without H_2O under conditions of (a) thermal-only at 120°C, (b) photothermal at 120°C, (c) thermal-only at 390°C, and (d) photothermal at 390°C. Differences between thermal-only and photothermal spectra on TiO_2 at (e) 120°C and (f) 390°C. Spectra for Au/TiO_2 without H_2O under conditions of (g) thermal-only at 120°C, (h) photothermal at 120°C, (i) thermal-only at 390°C, and (j) photothermal at 390°C. Differences between thermal-only and photothermal spectra on Au/TiO_2 at (k) 120°C and (l) 390°C.

On TiO_2 at 390°C, surface formate species were absent, perhaps because these intermediates were not stable at this temperature and quickly desorbed as partial oxidation products before further oxidation, consistent with the increasing selectivities to CO and H_2CO with increasing temperature observed in reaction experiments. A broad hydroxyl peak similar to that observed with UV on TiO_2 at 120°C was observed on TiO_2 at 390°C without UV irradiation. This thermal hydroxyl peak was not affected by UV, which was also consistent with a lower extent of complete oxidation observed in reaction experiments under the same conditions. On Au/TiO_2, strong peaks appeared at 1548, 1536, 1444, and 1349 cm^{-1}, attributed to acetate adsorbed on

Au [26,30,31] and two distinct peaks corresponding to surface hydroxyl species appeared at 3730 and 3664 cm^{-1}, attributed to the Au and TiO_2 surfaces, respectively. These acetate and hydroxyl peaks are consistent with thermal oxidation taking place on Au. At 390°C, the difference between UV differences was small, and the only differences between Au/TiO_2 and TiO_2 were with hydroxyl species and unknown C-O species with wavelengths larger than 1573 cm^{-1}.

Of the differences between TiO_2 and Au/TiO_2 at 120°C and 390°C, the decrease in hydroxyl species initially present on Au/TiO_2 at 120°C at the time of obtaining the background spectrum and the decrease in the amount of hydroxyl species on Au/TiO_2 at 390°C compared to TiO_2 were particularly interesting. It is known that deposited Au nanoparticles can cover TiO_2 hydroxyl sites which facilitate oxidation [2]. But the loss of surface TiO_2 hydroxyl species observed during DRIFTS for Au/TiO_2 compared to TiO_2 at 120°C and the decreased amount of hydroxyl species on Au/TiO_2 compared to TiO_2 at 390°C showed that Au nanoparticles somehow caused increased desorption of hydroxyl species not covered by Au nanoparticles under irradiation. This is consistent, at both low and high temperatures, with the decreased activity of Pathway A, which could have suffered from removal of surface hydroxyl species both by blockage and by desorption, and with the observed decrease in H_2O inhibition of Pathway B.

Further comparison of TiO_2 and Au/TiO_2 by DRIFTS data shows that photocatalytic activity of Au/TiO_2 can be explained by a combination of TiO_2 photoactivity and Au thermal activity, consistent with reaction experiments which showed no evidence of Au photoactivity. First, similar negative peaks for UV difference data around 1440 cm^{-1} suggest that TiO_2 photocatalysis occurring at 390°C also occurred on Au/TiO_2 at this temperature. Second, the additional hydroxyl species formed on the Au/TiO_2 surface at 3730 and 3664 cm^{-1} can be attributed to the complete thermal oxidation of partial oxidation products from TiO_2 photocatalysis.

The negative peaks at 1440 cm^{-1} observed for both TiO_2 and Au/TiO_2 indicate an unknown species removed from TiO_2 during irradiation. As the removal of this unknown species occurs

under the conditions where Pathway B is prevalent, studying its occurrence under different conditions could be important for gaining a better understanding of Pathway B.

Au/SiC photocatalytic ethylene oxidation experiments

Photochemical promotion of catalysis would decouple the material properties of the semiconductor from the material properties of the catalytically active material. This would allow a range of semiconductors to be used for the same catalytic metal, as long as photo-generated electrons in the conduction band could transfer to the metal nanoparticles. As TiO_2 was seen to have a high photocatalytic activity for the full range of temperatures tested, the specific effects of photochemical promotion of Au may have been difficult to observe on Au/TiO_2. Therefore, because a different semiconductor can theoretically be used to achieve the same promotion effect, experiments with 1 wt% Au/SiC prepared by photodeposition were conducted to isolate only this photochemical promotion of Au catalysis.

Thermal activation of C_2H_4 oxidation to CO_2 occurred at 400°C with SiC and Au/SiC (Figure 4.10(a) and (c)), with no significant detection of other oxidation products. No photocatalytic activity was observed for either SiC alone or Au/SiC (Figure 4.10(e) and (f)). However two observations made it difficult to observe the particular behavior of Au. First, Au/SiC had a much lower thermal activity than Au/TiO_2 under the same conditions. Second, Au/SiC appeared to have a slightly higher thermal activity than SiC, but the difference was much less than for Au/TiO_2 compared to TiO_2.

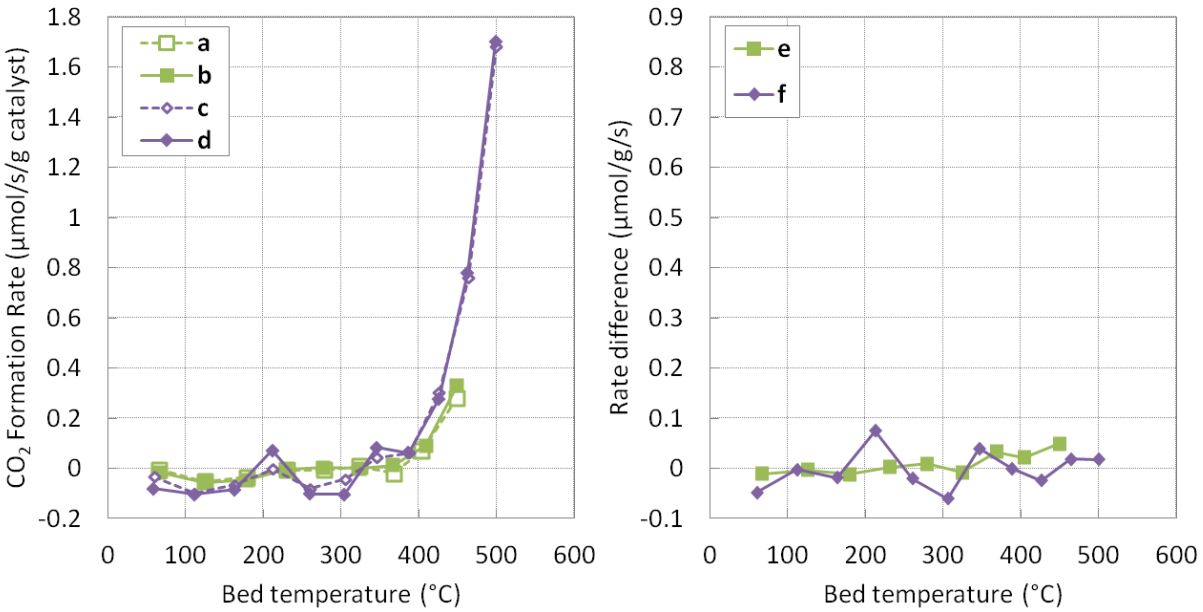

Figure 4.10 Photocatalytic CO_2 formation rates on SiC and Au/SiC without H_2O between 50°C and 500°C. (a) SiC under thermal-only conditions, (b) SiC under UV irradiation, (c) Au/SiC under thermal-only conditions, and (d) Au/SiC under UV irradiation. Differences between thermal-only and photothermal CO_2 formation rates without H_2O between 50°C and 500°C on (e) SiC and (f) Au/SiC.

The much lower activity of Au/SiC compared to Au/TiO_2, along with the difficulty of resolving the contribution of Au in Au/SiC compared to SiC, suggests a less efficient deposition of Au, much larger Au particle sizes, or Cl poisoning. Therefore this Au/SiC sample was not optimal for observing the particular effect of promotion of Au, and the absence of observed photocatalytic activity did not conclusively show that photochemical promotion does not occur. More experiments of this kind with better-characterized Au nanoparticles deposited on catalytically inactive semiconductors are needed.

Conclusion

The photocatalytic behavior of TiO_2 and Au/TiO_2 were investigated for ethylene oxidation at temperatures between 50°C and 500°C. Previously a maximum in photocatalytic oxidation rate was known to occur at approximately 150°C due to the decreasing fraction of productive charge carriers with increasing temperature. However in this study a second reaction pathway,

Pathway B, was distinguished by higher kinetic activation energy, inhibition by H_2O, and a higher selectivity to formaldehyde. The higher activation energy resulted in a higher temperature of maximum photocatalytic rate, approximately 400°C, unprecedented in photocatalysis. Future work should investigate the active site of Pathway B and determine if this site can facilitate other important industrial reactions, for example conversion of CO_2.

In-situ DRIFTS results showed that deposition of Au nanoparticles decreased the concentration of surface hydroxyl species during the reaction, indicating an increased desorption of H_2O. This is consistent with both the observed decrease in the activity of Pathway A, which may have been further limited by blockage of surface hydroxyl species by Au nanoparticles, and with the removal of H_2O inhibition of Pathway B. Further study is needed to understand the mechanism of this effect of Au on surface hydroxyl groups and on Pathway B in the presence of H_2O.

The photoproperties of semiconductors may be separated from the catalytic properties of metal nanoparticles for engineering purposes in catalytic systems where the catalytic activity of metal nanoparticles may be promoted by inducing a negative charge. Ethylene oxidation, proposed to be rate-limited by oxygen adsorption, is a good candidate. However no electrochemical promotion of Au activity was observed for photocatalytic ethylene oxidation experiments in this study, possibly due to particle growth and associated loss of Au nanoparticle contact with TiO_2 at elevated temperatures. Further study is recommended using a semiconductor that is catalytically inactive, deposited with Au nanoparticles that have a stable particle size. The core@shell nanostructure may be ideal for this purpose.

References

[1] Rajeshwar, K.; Chanmanee, W. Bioinspired photocatalyst assemblies for environmental remediation. *Electrochim. Acta* **2012**, *84*, 96-102.

[2] Primo, A.; Corma, A.; Garcia, H. Titania supported gold nanoparticles as photocatalyst. *Phys. Chem. Chem. Phys.* **2011**, *13*, 886-910.

[3] Mohamed, H.H.; Bahnemann, D.W. The Role of Electron Transfer in Photocatalysis: Facts and Fictions. *Appl. Catal., B* **2012**, *128*, 91-104.

[4] Choi, H.; Chen, W. T.; Kamat, P. V. Know thy nano neighbor. Plasmonic versus electron charging effects of metal nanoparticles in dye-sensitized solar cells. *Nano* **2012**, *6*, 4418-4427.

[5] Subramanian, V.; Wolf, E.E.; Kamat, P.V. Catalysis with TiO_2/gold nanocomposities. Effect of metal particle size on the Fermi level equilibration. *J. Am. Chem. Soc.* **2004**, *126*, 4943-4950.

[6] Hirakawa, T.; Kamat, P.V. Charge separation and catalytic activity of Ag@TiO_2 core-shell composite clusters under UV-irradiation. *J. Am. Chem. Soc.* **2005**, *127*, 3928-3934.

[7] Jakob, M.; Levanon, H.; Kamat, P.V. Charge distribution between UV-irradiated TiO_2 and gold nanoparticles: Determination of shift in the Fermi level. *Nano Lett.* **2003**, *3*, 353-358.

[8] Jovik, V.; Al-Azri, Z.H.N.; Chen, W.-T.; Sun-Waterhouse, D.; Idriss, H.; Waterhouse, G.I.N. Photocatalytic H_2 production from ethanol-water mixtures over Pt/TiO_2 and Au/TiO_2 photocatalysts: A comparative study. *Top. Catal.* **2013**, *56*, 1139-1151.

[9] Shen, P.; Zhao, S.; Su, D.; Li, Y.; Orlov, A. Outstanding performance of sub-nm Au clusters for photocatalytic hydrogen production. *Appl. Catal., B* **2012**, *126*, 153-160.

[10] Lin, H.-Y.; Chang, Y.-S. Photocatalytic water splitting for hydrogen production on Au/$KTiNbO_5$. *Int. J. Hydrogen Energy* **2010**, *35*, 8463-8471.

[11] Mohamed, H.H.; Dillert, R.; Bahnemann, D.W. Kinetic and Mechanistic Investigations of the Light Induced Formation of Gold Nanoparticles on the Surface of TiO_2. *Chem. Eur. J.* **2012**, *18*, 4314-4321.

[12] Nosaka, Y.; Norimatsu, K.; Miyama, H. The function of metals in metal-compounded semiconductor photocatalysis. *Chem. Phys. Lett.* **1984**, *106*, 128-131.

[13] Abdulla-Al-Mamun, M.; Kusumoto, Y.; Zannat, T.; Islam, M.S. Synergistic cell-killing by photocatalytic and plasmonic photothermal effects of Ag@TiO_2 core-shell composite nanoclusters against human epithelial carcinoma (HeLa) cells. *Appl. Catal., A* **2011**, *398*, 134-142.

[14] Chiarello, G.L.; Aguirre, M.H.; Selli, E. Hydrogen production by photocatalytic steam reforming of methanol on noble metal-modified TiO_2. *J. Catal.* **2010**, *273*, 182-190.

[15] Westrich, T.A.; Dahlberg, K.A.; Kaviany, M.; Schwank, J.W. High-temperature phtocatalytic ethylene oxidation over TiO_2. *J. Phys. Chem. C* **2011**, *115*, 16537-16543.

[16] Chistopher, P.; Xin, H.; Marimuthu, A.; Linic, S. Singular characteristics and unique chemical bond activation mechanisms of photocatalytic reactions on plasmonic nanostructures. *Nat. Mater.* **2012**, *11*, 1044-1050.

[17] Linic, S.; Christopher, P.; Ingram, D.B. Plasmonic-metal nanostructures for efficient conversion of solar to chemical energy. *Nat. Mater.* **2011**, *10*, 911-921.

[18] Broqvist, P.; Molina, L.M.; Grönbeck, H.; Hammer, B. Promoting and poisoning effects of Na and Cl coadsorption on CO oxidation over MgO-supported Au nanoparticles. *J. Catal.* **2004**, *227*, 217-226.

[19] Chandler, B.D.; Long, C.G.; Gilbertson, J.D.; Pursell, C.J.; Vijayaraghavan, G.; Stevenson, K.J. Enhanced oxygen activation over supported bimetallic Au-Ni catalysts. *J. Phys. Chem.* **2010**, *114*, 11498-11508.

[20] Min, B.K.; Friend, C.M. Heterogeneous gold-based catalysis for green chemistry: Low-temperature CO oxidation and propene oxidation. *Chem. Rev.* **2007**, *107*, 2709-2724.

[21] Ibrahim, N.; Poulidi, D.; Metcalfe, I.S. The role of sodium surface species on electrochemical promotion of catalysis in a Pt/YSZ system: The case of ethylene oxidation. *J. Catal.* **2013**, *303*, 100-109.

[22] Xie, W.; Li, Y.; Sun, W.; Huang, J.; Xie, H.; Zhao, X. Surface modification of ZnO with Ag improves its photocatalytic efficiency and photostability. *J. Photochem. Photobiol., A* **2010**, *216*, 149-155.

[23] Subramanian, V.; Wolf, E.E.; Kamat, P.V. Green emission to probe photoinduced charging events in ZnO-Au nanoparticles. Charge distribution and Fermi-level equilibration. *J. Phys. Chem. B* **2003**, *107*, 7479-7485.

[24] Fox, M.A.; Dulay, M.T. Heterogeneous photocatalysis. *Chem. Rev.* **1993**, *93*, 341-357.

[25] Sun, S.; Ding, J.; Bao, J.; Gao, C.; Qi, Z.; Li, C. Photocatalytic oxidation of gaseous formaldehyde on TiO_2: An in situ DRIFTS study. *Catal. Lett.* **2010**, *137*, 239-246.

[26] Yu, Z.; Chuang, S.S.C. In Situ IR study of adsorbed species and photogenerated electrons during photocatalytc oxidation of ethanol on TiO_2. *J. Catal.* **2007**, *246*, 118-126.

[27] Setvin, M.; Aschauer, U.; Scheiber, P.; Li, Y.-F.; Hou, W.; Schmid, M.; Selloni, A.; Diebold, U. Reaction of O_2 with subsurface oxygen vacancies on TiO_2 anatase (101). *Science* **2013**, *341*, 988-991.

[28] Cozzoli, P.D.; Fanizza, E.; Comparelli, R.; Curri, M.L.; Agostiano, A.; Laub, D. Role of metal nanoparticles in TiO_2/Ag nanocomposite-based microheterogeneous photocatalysis. *J. Phys. Chem. B* **2004**, *108*, 9623-9630.

[29] Takenaka, S.; Matsumori, H.; Matsune, H.; Tanabe, E.; Kishida, M. High Durability of Carbon Nanotube-Supported Pt Electrocatalysts Covered with Silica Layers for the Cathode in a PEMFC. *J. Electrochem. Soc.* **2008**, *155*, B929–B936.

[30] Nguyen, L.Q.; Salim, C.; Hinode, H. Roles of nano-sized Au in the reduction of NO_x by propene over Au/TiO_2: An in situ DRIFTS study. *Appl. Catal., B* **2010**, *96*, 299-306.

[31] Xu, W.Q.; Liu, Z.Y.; Johnston-Peck, A.C.; Senanayake, S.D.; Gong, Z.; Stacchiola, D.; Rodriguez, J.A. Steam reforming of ethanol on Ni/CeO2: reaction pathway and interaction between Ni and CeO_2 support. *ACS Catal.* **2013**, *3*, 975-984.

Chapter 5

Conclusions and future work

The capability of catalysts to meet future energy and environmental challenges, including in transportation fuel reforming for auxiliary power units and photocatalysis applications, hinges on achieving particular improvements in their activity, selectivity, and stability. Conventionally the catalyst support is only a refractory material with a high physical surface area over which metal nanoparticles are dispersed, but ongoing research is showing how supports can be engineered to have crucial impacts on the above properties.

Core@shell nanostructured catalysts have attracted interest for many applications because they avoid metal particle growth, maximize metal-support interactions, and impose a diffusion barrier between the metal nanoparticles and the bulk reaction phase that engenders size selectivity characteristics. The advantages of core@shell nanostructures may be particularly amenable to fuel reforming, wherein Ni-based catalysts suffer particle growth and carbon deposition, and high selectivity to products is limited by equilibrium. Yet despite several studies of Ni@SiO_2 catalysts for methane partial oxidation and steam reforming reactions, much was unknown about the long term stability of these materials, the extent of Ni particle growth and carbon deposition, stability of the SiO_2 shell morphology and porosity, and potential size selectivity characteristics. The yolk-shell morphology may have additional advantages, such as a lower coverage of the metal surface by the shell material and the potential accumulation of

intermediates in the gas phase in contact with the catalytic surface to enhance selectivity. However, no direct comparison of yolk-shell and core@shell nanostructures for a catalytic application had been reported. In addition, many synthetic strategies for yolk-shell have been reported, but most did not completely encapsulate the metal and were limited to only certain materials.

The work presented in this thesis has addressed the above questions. In Chapter 2, a novel synthesis technique for Ni@SiO_2 nanotubes using a nonionic microemulsion template was demonstrated [1], which could be used to produce both nanospheres and nanotubes under certain conditions. Extensive TEM analysis showed that the nanotube cavities were cylindrical and highly uniform with diameters of 12-13 nm independent of length, that the nanotube lengths could be controlled up to 2 microns, and that the nanotube shell thicknesses could be controlled in the range of 5.1 to 12.4 nm. H_2 chemisorption experiments showed high Ni dispersions over 14-15% in Ni@SiO_2 nanotubes, and N_2 physisorption analyses revealed SiO_2 micropores on the order of 1 nm.

A new phenomenon was discovered underlying Ni@SiO_2 nanotube formation. The hypothesis advanced in Chapter 2 is that N_2H_4 decomposed into gases which were entrained in reverse micelles, causing their elongation and excluding the shell precursor from inner micellar regions, leading to the formation of cavities. However, it remains an open question why micelles with a growing entrained gas phase elongate one-dimensionally into remarkably stable cylinders rather than spheres. Although no instances of gas entrainment have been reported, observations of micelle elongation in nonionic water-in-oil microemulsions have usually been explained as a thermodynamic balance between two effects: first, either a less energetically favorable interaction between hydrophobic surfactant groups and the continuous oil phase or increased aggregation number due to increased total inner micellar volume (tending to favor enlarged spherical micelles); and second, the minimization of the conformational energy of hydrophobic surfactant groups (tending to favor elongated cylindrical micelles).

According to the above considerations, it was hypothesized that an increased aggregation number associated with a growing volume of entrained gas caused micelle elongation. Future work should employ cross polarized light microscopy to directly observe potential liquid crystalline phases in microemulsions under conditions where micelles are suspected to be elongated. Further, it may be of interest to explore how the Laplace pressure inside the micelle might change with the presence of an entrained gas phase or with elongation. Finally, if the above hypotheses regarding micelle elongation due to gas evolution and the underlying thermodynamics are correct, then varying the length of the hydrophobic alkyl group of the surfactant would be expected to change the diameter of the elongated micelles and therefore the cavity diameter of SiO_2 nanotubes. Specifically, decreasing the alkyl group length should increase these diameters and perhaps even lead to enlarged spherical micelles.

While Ni@SiO_2 nanotubes exploited the cavity formation and elongation phenomenon well, other core and shell materials may be possible using this technique. For example, preliminary syntheses of Co@SiO_2 and Fe@SiO_2 nanotubes by simple 1:1 molar substation of the Ni precursor with Co and Fe precursors were promising. The resulting materials clearly contained metal nanoparticles in open cavity spaces encapsulated by elongated SiO_2 shells. Optimization of the material structure should be possible by controlling the variables that affect the rate and amount of gas evolution from N_2H_4 oxidation. Even nanotubes without encapsulated metal nanoparticles should be possible using this technique, if a compound that solubilizes in the micelle such as N_2H_4 or H_2O_2 can evolve gas under stable microemulsion conditions with nonmetal oxidizing agents.

In propane autothermal reforming experiments presented in Chapter 3, Ni@SiO_2 nanotubes and nanospheres each outperformed impregnated Ni/SiO_2 in both H_2 yield and stability during 20 hr on stream. Specifically, Ni@SiO_2 samples had superior ethylene steam reforming and water-gas shift activity as well as less extensive particle growth and carbon deposition. More carbon deposition was observed for Ni@SiO_2 nanotubes, likely due to the greater extent of particle growth possible in its open cavities. SiO_2 shell sintering was observed with both

Ni@SiO_2 samples, and both morphologies approached a similar morphology under reaction conditions, but there were no observed consequences on performance. Even so, to alleviate concerns of shell degradation, other more stable shell materials such as Al_2O_3 or ZrO_2 should be tried; or core@shell materials may be better recommended for reactions that require lower operating temperatures.

In the first known direct comparison of the catalyst performances of core@shell and yolk-shell nanostructures, the Ni@SiO_2 nanotubes and nanospheres were not significantly different. This was likely due in part to both materials approaching a similar morphology over time, and future work should investigate possible performance differences in situations where these nanostructures are stable over time. In the first known study of the potential influence of the size selectivity characteristics of core@shell on the selectivity of equilibrium-limited reactions, both Ni@SiO_2 morphologies had strikingly different product selectivities compared to impregnated Ni/SiO_2. The higher H_2, higher CO_2, and lower CO selectivites of the Ni@SiO_2 catalysts suggested that they were more active for the water-gas shift reaction, which may have been caused by the selective removal of H_2 from the gas phase in contact with the catalyst surface. Future work should investigate if this desirable size selectivity effect can be enhanced by maintaining the cavity spaces in Ni@SiO_2 nanotubes under reaction conditions (with the potential for accumulating reaction intermediates), perhaps by replacing SiO_2 with Al_2O_3 or ZrO_2; and by increasing the shell thickness according to the methods demonstrated in Chapter 2. If the water-gas shift reaction selectivity indeed can be altered in this way by the core@shell nanostructure, this size selectivity effect should be investigated for designated water-gas shift catalysts. Core@shell nanostructure should also be applied to other reactions where size selectivity is desirable.

While these Ni@SiO_2 materials have been convincingly shown to be resistant to deactivation by carbon deposition, they may also be resistant to deactivation by sulfur poisoning. This process is highly problematic for Ni-based catalytic reforming of liquid fuels, typically containing on the order of 30-3000 ppm thiophenes, benzothiophenes, and dibenzothiophenes [1]. In previous

studies in our group, we confirmed the severe deactivation of Ni-based reforming catalysts due to exposure to sulfur-containing species [2,3]. However, the porous shell of Ni@SiO_2 catalysts is hypothesized to greatly increase the lifetime of Ni-based authothermal reforming catalysts by mitigating exposure to bulky sulfur-containing species. For example, dibenzothiophene, with a diameter of gyration of ca. 0.94 nm, is expected to be highly mass-transport limited in its diffusion to the metal surface of the Ni@SiO_2 materials reported here, having pore sizes on the order of 1 nm. Moreover, we have shown that smaller Ni particles have greater sulfur tolerance [3], and so the potential of Ni@SiO_2 to stabilize a high Ni dispersion and avoid particle growth may further curtail sulfur poisoning. These hypotheses should also be tested in future work.

In addition to providing stability against metal particle growth and size selectivity characteristics, catalyst supports may also interact electronically with metal nanoparticles to enhance performance. The manner in which a catalyst support can interact electronically with metal nanoparticles was explored in an entirely new way for photocatalysis in Chapter 4. In photocatalysis research, well-known strategies to increase photo efficiency like controlling particle size, controlling phase composition, coupling two or more semiconductors, and doping have not achieved sufficient efficiency for full-scale implementation, and different strategies are highly desirable. Recently we have shown in photocatalytic ethylene oxidation experiments on TiO_2 that photo generation of charge carriers is not only possible but increases with increasing temperature, reaching a maximum at a temperature near where heterogeneous catalysts become active [4]. But the effect of H_2O and the formation of partial oxidation products were not considered, limiting our understanding of photocatalytic behavior at elevated temperature.

Deposition of metal nanoparticles on photocatalysts is known to decrease recombination rates at ambient temperatures through the transfer of photo-generated electrons to these metal nanoparticles. This phenomenon could further enhance photocatalytic activity at elevated temperatures. Additionally, this transfer of photo-generated electrons to metal nanoparticles may produce an electrochemical promotion for electrophilic reactions. The advent of

photochemical promotion of catalysis would decouple the materials engineering constraints of the catalytically active metal and photochemically active semiconductor and offer a completely new strategy for catalyst design for many applications.

Neither of the above-hypothesized effects of the transfer of photo-generated electrons to Au nanoparticles was observed in photocatalytic ethylene oxidation experiments on Au/TiO_2, likely due to a combination of two effects. First, Au nanoparticles caused a loss of surface hydroxyl species, which facilitate Pathway A, due to blockage and increased desorption. Second, Au particle growth likely occurred at higher temperatures where Pathway B and Au thermal activity are prevalent, resulting in loss of contact between Au particles and TiO_2. However both photo-generated electron transfer hypotheses remain compelling and should be pursued in future work. The effects of electron transfer at lower temperatures may be better observed with a different reaction not reliant on surface hydroxyl species, or with Au/TiO_2 samples prepared by methods other than photodeposition such as deposition-precipitation or impregnation which are not known to selectively cover surface hydroxyl species. The effects of electron transfer at high temperatures may be better observed with Au/TiO_2 samples with smaller and more stable Au particle sizes. Au nanoparticles deposited on TiO_2 via the photodeposition synthesis route are typically large and in poor contact with the semiconductor compared to other routes like impregnation or deposition-precipitation, and so these latter methods should be employed. Additionally, Au particle sizes may be better stabilized at high temperature by utilizing a core@shell nanostructure, either $Au@TiO_2$ or by depositing a layer of porous SiO_2 on Au/TiO_2. Other metals, whose nanoparticles may be more stable and which may catalyze different reactions, should be investigated over a range of Fermi levels and charging tendencies. Finally, utilizing semiconductors that do not participate in the reaction pathway except by transferring electrons to metal nanoparticles may help resolve metal promotion effects.

While the core@shell nanostructure affords catalysts significant advantages in stability and size selectivity, they have also been noted to intrinsically maximize the contact of the metal and

support. As noted above, one can envision the photocatalysis of Au/TiO_2 being optimized by a core@shell nanostructure (i.e., $Au@TiO_2$) due to the stabilization of metal particle size and contact with the semiconductor at elevated temperatures. Moreover, because the TiO_2 material in $Au@TiO_2$ would be entirely both near the surface and in close proximity to Au nanoparticles, photo-generated charge carriers would travel a minimum distances to trap states, therefore minimizing recombination.

Although effects of photo-generated electron transfer to Au nanoparticles were not observed, a new photocatalytic pathway, designated Pathway B, was discovered on TiO_2, which achieved a maximum photocatalytic ethylene oxidation rate near 400°C, unprecedented in photocatalysis on semiconductors. Significantly, temperatures near 400°C can be achieved under solar irradiation. Pathway B was also found to be inhibited by H_2O and a higher selectivity to formaldehyde formation, whereas previously known Pathway A was enhanced by H_2O and had a lower selectivity to formaldehyde. Au nanoparticles had no effect on Pathway B but hindered Pathway A and even increased H_2O desorption, which favored Pathway B in the presence of H_2O. The discovery of Pathway B raises interesting questions about what other reactions may be facilitated by its active sites, and future work should pursue an understanding of the nature of these sites. Transient DRIFTS experiments at 400°C with various reaction environments with and without UV irradiation should more fully reveal the order of formation and reaction of surface intermediates. Oxygen vacancies are one candidate for the active site of Pathway B, and this hypothesis should be tested using TPR and TPO analyses following in-situ N_2, O_2/N_2, and $C_2H_4/O_2/N_2$ treatments, with and without UV irradiation. TPD experiments should be performed to test if CO_2 or other species of interest adsorb at all or more after similar in-situ pre-treatments. Finally, Pathway B may be illuminated through experiments with varying C_2H_4 and O_2 concentrations under conditions where this pathway is prevalent. Reaction orders measured from these data may then be linked to a microkinetic model to elucidate the reaction mechanism of Pathway B.

In summary, with the growing knowledge of the specific ways that supports may be engineered to enhance catalyst performance, and how these benefits can be maximized in the core@shell nanostructure, interest in support effects and core@shell materials is expected to continue to grow. This thesis has investigated new catalyst support effects to address specific challenges in fuel reforming and photocatalysis, and has sought to present the knowledge gained in a broader context, highlighting the underlying strategies and phenomena which may be transferable to other areas of catalysis research. Certainly the new ideas advanced in this thesis, including nanotube synthesis in a microemulsion template, core@shell size selectivity to enhance the selectivity of equilibrium-limited reactions, photocatalysis at elevated temperatures, and photochemical promotion of catalysis, promise to have broad implications for the field of catalysis.

References

[1] Dahlberg, K.; Schwank, J.W. Synthesis of Ni@SiO_2 nanotube particles in a water-in-oil microemulsion template. *Chem. Mater.* **2012**, *24*, 2635-2644.

[2] Mayne, J.M.; Tadd, A.R.; Dahlberg, K. A.; Schwank, J.W. Influence of thiophene on the isooctane reforming activity of Ni-based catalysts. *J. Catal*. **2010**, *271*, 140-152.

[3] Mayne, J.M.; Dahlberg, K.A.; Westrich, T.A.; Tadd, A.R.; Schwank, J.W. Effect of metal particle size on sulfur tolerance of Ni catalysts during autothermal reforming of isooctane. *Appl. Catal., A* **2011**, *400*, 203-214.

[4] Westrich, T.A.; Dahlberg, K.A.; Kaviany, M.; Schwank, J.W. High-temperature phtocatalytic ethylene oxidation over TiO_2. *J. Phys. Chem. C* **2011**, *115*, 16537-16543.